Università degli Studi Roma Tre

Scuola Dottorale in Scienze Matematiche e Fisiche
Sezione di Fisica

XXVII Ciclo

Ph.D. Thesis

Auger-PhotoElectron Coincidence Spectroscopy on magnetic thin films: a study of multiplet spin structure and electron correlation

Ph.D. Student: ***Marco Sbroscia***

Supervisor: ***Prof. Giovanni Stefani***

Coordinator: ***Prof. Roberto Raimondi***

Per questo traguardo:
a papà Franco e a mamma Leonarda,
alla mia compagna Silvia,
a me, il piccolo di casa.

Per la vita che ci attende:
a nonno Franco e nonna Leonarda
a nonno Mario e nonna Tiziana
a zia Sara e zia Adele
a zio Armando
a mamma Silvia
a papà Marco
a Irene, la piccola di casa,
la nostra nuova grande avventura.

È difficile essere giusti
perciò cerco di essere onesto.

Contents

Introduction **1**
Magnetic systems above transition temperature: is long- or short-range order lost? . . . 2
Probing electron correlation: the advent of electron-pair detection experiments . . . 5
How APECS can access magnetic properties from a local viewpoint 7

1 Magnetic properties of solids **11**
1.1 Magnetism in three-dimensional systems . . . 11
1.1.1 Ferromagnetism . . . 14
1.1.2 Antiferromagnetism . . . 21
1.1.3 Indirect exchange . . . 27
1.2 Magnetism in thin films . . . 28
1.2.1 Surface vs. bulk magnetisation . . . 29
1.2.2 Thickness dependence of transition temperature and magnetic moment direction . . . 30
1.3 Magnetic bilayers . . . 33
1.3.1 Exchange bias . . . 34

2 Electron spectroscopies **39**
2.1 Photoemission spectroscopy . . . 39
2.1.1 Specimen thickness estimation using photoemission spectroscopy . . . 44
2.2 Auger electron spectroscopy . . . 46
2.3 Auger-PhotoElectron Coincidence Spectroscopy . . . 58
2.3.1 Basic theory of APECS: one- and two-step description 58
2.3.2 AR-APECS . . . 62
2.3.3 DEAR-APECS . . . 70

3 Experimental set-up **73**
3.1 Light source . . . 75
3.1.1 Synchrotron Radiation . . . 75
3.1.2 The insertion device . . . 76
3.2 The ALOISA beamline . . . 79
3.2.1 Light transport . . . 79
3.2.2 The end station . . . 82
3.3 Electrons detection . . . 85
3.3.1 Electrostatic lenses . . . 86

3.3.2 Hemispherical analysers 90
3.3.3 Channeltron, Micro-channel Plate and Delay anode . . 91
3.4 Coincidence acquisition chain 98
3.4.1 Raw data: time spectrum 100
3.5 Experimental geometry in AR-APECS experiments 106

4 Investigation of electronic spin coupling in magnetic systems by APECS 111
4.1 Unravelling final state spin multiplet terms in Antiferromagnetic system, the case of NiO 112
4.1.1 The NiO/Ag(100) sample 112
4.1.2 Thickness estimation 113
4.1.3 Magnetic phase transition 118
4.1.4 AR-APECS from NiO below and above the transition temperature 124
4.2 Investigation of electron correlation in Ferromagnetic thin films, the cases of Ni and Fe 133
4.2.1 Experimental 134
4.2.2 AR-APECS spectra from ferromagnetic Ni/Cu(001) and Fe/Ag(001) 138
4.3 Insight of a FM/AFM bilayer interface spin multiplet terms via coincidence spectroscopy, the case of Fe/CoO 143
4.3.1 Experimental 145
4.3.2 AR-APECS spectra 145

Conclusions 151

A Data analysis 155
A.1 Filters 157
A.2 Time spectra construction 157
A.3 Peak alignment 159
A.4 Time correction 159
A.5 Building different kinematics 160
A.6 From time spectra to APECS spectra 161

Ringraziamenti 165

Bibliography 167

Introduction

Understanding and controlling electron correlation is one of the hardest task of modern physics. Electron-electron interaction is of particular interest because several highly intriguing phenomena like Ferro- and Antiferromagnetism (FM and AFM), Giant and Colossal Magnetoresistance or Superconductivity are due to such a correlation. Since the advent of quantum mechanics, physicists have had to contend with difficulties of finding analytical solutions to Schrödinger equation already for an atom as simple as Helium. In this simple case, for infinite nucleus mass approximation, the Hamiltonian of the system reads

$$H = -\frac{\hbar^2}{2m}\nabla^2_{\vec{r_1}} - \frac{Ze^2}{4\pi\varepsilon_0 r_1} - \frac{\hbar^2}{2m}\nabla^2_{\vec{r_2}} - \frac{Ze^2}{4\pi\varepsilon_0 r_2} + \frac{e^2}{4\pi\varepsilon_0 r_{12}}$$

where the last term describes the interaction among the two electrons. Unfortunately Coulomb interaction goes to zero as $\frac{1}{r}$, where r represents the distance between two charges and it does not allow to consider two electrons inside the same potential well completely independent. An example of physical interest is the case of two electrons belonging to the same atomic site. Such an interaction term, and in the same manner every electron correlation term, produces an Hamiltonian not separable in single-particle contributions, making not possible to determine the exact eigenvalues as well as eigenstates of the system. In interpreting material properties local density approximation (LDA) is a widely used frame for the independent quasi-particle picture. LDA is structured after a semiclassical mean-field theory approach and because it is based on the use of a one-electron potential, it fails in describing strongly correlated systems. For example in a LDA picture a $3d$-metal oxide Mott insulator is not properly described: FeO or CoO appears to have metallic behaviour instead of the insulator one pointed out experimentally. To include in the description the role played by interacting electrons, the so called density-functional theory (DFT) was developed. DFT is a theory devoted to determine the electronic ground state structure for non-relativistic interacting electrons in an external potential $v(\vec{r})$. It is based on the sim-

ple Hohengberg and Kohn lemma [1] which states that since the external potential influences the ground state energy of a many interacting electrons system and this potential is an unique functional of the one-particle electronic charge density $n(\vec{r})$, the knowledge of such a physical quantity leads, via a variational method, to the determination of the ground state itself [2]. Despite this step forward with respect to the original LDA approach, some aspects for interacting-electron systems are still missing: for NiO the pure DFT is not suitable to determine the right value of its band-gap [3, 4]. This is mainly because DFT neglects correlation among *d*-electrons, incorrectly accounting for occupancy of localized states. The main problem in applying DFT in the LDA to system with localised electrons resides in the dependence of the density functional from the *exact* potential. This latter seems to show discontinuities not reproduced in this method leading to the failure of the LDA in describing properties of strongly correlated materials, e.g. the band gap of Mott insulators [5, and ref. therein] as mentioned before. Thus, what was said just above makes clear the necessity to go beyond any single-particle approach to properly describe such systems, overcoming methods in which the interaction among electrons is approximated via a mean field or introduced in a pure perturbative manner.

These few examples have been proposed just to underline the importance of taking into account the electron correlation. This is more relevant in the case of magnetic systems where the electron-electron interaction is the origin of such properties. In this thesis a correlation-sensitive spectroscopic technique like Auger PhotoElectron Coincidence Spectroscopy is applied to magnetic thin films with the aim to validate theoretical models which describes the electron spin coupling contributing to the Auger transition and to access an unambiguous assignment of the several final state spin terms allowing for a deeper understanding of the electron correlation and magnetic properties at atomic scale.

Magnetic systems above transition temperature: is long- or short-range order lost?

Highly correlated systems are occupying a relevant place in modern physics not only because a proper and complete description of their properties has not been reached yet, but also for their possible use in new devices. In this latter field a central role is played by magnetic thin films and heterostructures for their application in spintronics, hence monitoring the magnetic phase transition becomes a fundamental aspect. A highly debated issue is the origin

of magnetic properties of solids at the atomic level or, in other words, what happens to magnetic and electronic structures, from a microscopic viewpoint, when a sample exceeds its own magnetic transition temperature (Curie temperature (T_C) for FM, Néel temperature (T_N) for AFM). It is well known that when a FM or an AFM material is well below this critical temperature it shows a long range magnetic order throughout the solid. When the solid overcomes the transition temperature the long-range order is lost, but what happens at atomic scale is still far from the comprehension and, at the state of the art, conflicting experimental evidences are present. Mook *et al.* [6] performing neutron scattering on a FM Ni specimen showed that spin-wave excitations could be observed at temperature higher than Curie point relating this to the persistence of spin correlation well above the transition temperature. Of the same tendency are the photoemission results from bulk [7, 8] as well as surface [9] states of Ni. In these cases photoemission spectra show the presence of two distinct peaks associated to the spin-up and spin-down splitted bands. Increasing the temperature, exceeding the Curie point, the non-collapse of these two structures characterising the spectra reveals the persistence of exchange splitting and consequently the existence of a short-range magnetic order above T_C. Hopster *et al.* [10] found an experimental temperature-dependence of exchange splitting (decreasing of the exchange splitting upon increasing the temperature) in Ni that cannot be concordant with the temperature-independent theoretical models supported by the aforementioned results. So the situation is far from being clear because the exchange-splitting temperature-dependence is strongly dependent from the theoretical approach used in interpreting photoemission spectra [9]. Contradictions are not finished yet. In a magnetic material, below the phase transition temperature, exchange interaction splits the valence band in two pure spin bands. Spin band splitting derives from the proper balance of exchange-energy gain (the interaction among electron's spins) and the kinetic energy variation due to Pauli exclusion principle (electrons with the same spin have to be in different $\left(\vec{k}, E\left(\vec{k}\right)\right)$ band points). In such a scenario the characteristic FM or AFM behaviour is described, in an Heisenberg model approach, through an Hamiltonian term like

$$E_{ex} = -\sum_{i \neq j} J_{ex}^{ij}\, \vec{S}_i \cdot \vec{S}_j$$

where the sum runs over all the atomic sites, $\vec{S}_i$ and $\vec{S}_j$ are spins of two different interacting electrons, while J_{ex}^{ij} is the exchange integral and the external field contribution is neglected. The exchange integral takes into account the FM or AFM nature of the system. The minimisation of the exchange energy implies that if $J_{ex} > 0$ the spins of interacting electrons are

coupled in a parallel alignment favouring a FM order, while if $J_{ex} < 0$ an antiparallel coupling is favoured leading to an AFM order. Such a model derives from a local description of the (anti-) ferromagnetism and puts in evidence the role of the electron correlation in such phenomena. Anyway this model can be integrated by a band theory approach in which the magnetic properties of a system are derived from their band structure, the so called Stoner model. For a spin polarised sample the density of states (DOS) shows two different subbands accounting for spin-up and spin-down populations. These two bands are energy shifted because of the exchange interaction and this splitting is reduced upon increasing the temperature. Once the sample's temperature exceeds the transition point these two bands coalesce, as predict by long-range-order models. Magnetic excitations, like single-particle spin flip (Stoner excitation) or collective excitations (spin-waves or magnons) [11], are expected to be sensitive to such changes. It is expected that differences in the spin bands splitting leads to a temperature dependence in the energy-vs-momentum plot of these quasi-particles, but on the contrary such a dependence has not been observed in neutron scattering experiments by Mook *et al.* [6]. Of the same advice is the work by Kirschner and Langenbach [12] in which exchange splitting in Ni has been shown to be temperature independent using high-resolution spin-polarised electron-energy-loss spectroscopy. Spin-resolved photoemission and inverse-photoemission experiments performed on Fe [13, 14] pointed out a complex scenario: the collapse of magnetic order depends upon the sampled point in k-space, for example studying the exchange splitting of empty bands it has been shown that for an high symmetry phase-space point, namely the H point, of a bcc Fe sample majority and minority bands merge together upon approaching the Curie point from below, while for the same crystal, sampling two other different phase-space points, a non-collapsing behaviour is found. These complications make difficult to understand the itinerant-electron ferromagnetism[1]. During the '90s other experiments were performed in order to clarify the situation which, however, remained the same: temperature and wave-vector dependence of exchange splitting [15, 16] and collapse of band-splitting approaching the Curie temperature observed in inverse photoemission [17] are in contrast with the presence of local moments of $3d$-character and spin polarisation above T_C [18] still making not possible to properly interpret magnetism. Recently the temperature evolution of itinerant ferromagnetism [19, 20] seemed to be in agreement with the persistence of local magnetic moment well above the Curie point, but, again, the issue about whether FM originates from local

[1] An itinerant ferromagnet is a system whose magnetic properties are characterised by those electrons able to be delocalised on different atomic sites.

moment or itinerant electrons is of pivotal importance. In the last years efforts have been made in trying to answer it unequivocally, but unfortunately a complete description of magnetism remains controversial.

Probing electron correlation: the advent of electron-pair detection experiments

As discussed in the previous sections, a complete understanding of magnetism around the transition temperature has not been reached yet. As a consequence theoretical models are able to predict only a few aspects at a time of the physical phenomena observed experimentally. The Stoner-Wohlfarth approach [21, and ref. therein], based on the assumption that the exchange energy is proportional to the square of the magnetisation, takes into account a reduction of the exchange interaction upon increasing the temperature reaching a paramagnetic state at the Curie point. On the contrary, in local fluctuating band theories, the magnetic phase transition is driven by the *transverse fluctuations* like the spin-waves. In this case, for an itinerant ferromagnet, because of the delocalised nature of the electronic wave functions, the $\mathbf{S}_i{}^2$, where $\mathbf{S}_i$ represents the total spin density operator for the i-th lattice site, does not correspond to a sharp quantum number. This means that fluctuations among different atomic sites are able to destroy the long-range magnetic order, preserving local magnetic moments above T_C.

In order to overcome this controversial picture, in the last decades efforts have been dedicated to the description of strongly correlated material properties. As mentioned before the LDA scheme, even considering the DFT approach, is not completely satisfactory because it fails in describing correlation among the d- and f-electrons while they play a critical role in magnetism. In this direction the first refinement has been the introduction of the Hubbard parameter U, which describes Coulomb energy interaction among two electrons at the same lattice site [22], in the so called LDA+U scheme [23, 5, 24] as well as the introduction of the dynamical mean field theory (DMFT) approach [25, 26], but for the comprehension of magnetism in solids, the capability to completely describe the itinerant electrons behaviour plays a crucial role. The nature of these electrons can be classified comparing the same U parameter coming from the Hubbard Hamiltonian [22] with respect to the band width W to which they belong. In systems like magnetic thin films of $3d$ metal and their oxides, where U, W and the exchange interaction Δ, responsible for majority and minority spin bands splitting, are of the same magnitude, it is not possible to neglect the mutual

electron repulsion.

The difficulties in understanding magnetism and, more in general, Coulomb interaction in many-body effects, originates not only from the theoretical side, indeed the most common and used spectroscopic techniques are based on single-particle interpretation. For example photoemission spectroscopy involve a single-particle dipole matrix element. Despite very appealing, because the quasi-particle band structure can be probed, these single electron spectroscopies give us information about correlation only indirectly, e.g. via the satellite peaks in photoemission spectra, but this seems not to be enough to fully understand electron correlation and related phenomena. In the last forty years efforts have been made in developing new experimental techniques able to directly probe electron correlation. In this scenario the electron-pair emission based experiments like direct and core-resonant Double Photoemission seem to be successful. In this kind of experiments two or more electrons coming from the same interaction process between the sample and the probe (electrons or photons) are collected. This means that after excitation the target falls in a final state characterised by two or more interacting holes in the valence band, giving access to correlation effects. These techniques are suitable for probing matter in its various states of aggregation: in atomic, molecular or solid form.

In a direct double photoemission process the photon absorption leads to the emission of two electrons according to

$$\hbar\omega + A \rightarrow A^{++}\left(v^{-1}v^{-1}\right) + e^{-} + e^{-}$$

where an impinging photon represented by its energy $\hbar\omega$ and a neutral charged atom target in its ground state, A, form the initial state. In the final state are present a doubly ionised atom $A^{++}\left(v^{-1}v^{-1}\right)$ with two holes in valence levels and two electrons emitted in the continuum. These two electrons can share the excess energy available in the final state.

It is possible to get the same final state via the decay of a core-hole, that leads to the emission of an Auger electron coupled to the photoemitted one. In this case the double photoionisation process is termed as core-resonant and the reaction reads

$$\hbar\omega + A \rightarrow A^{+}\left(c^{-1}\right) + e^{-} \rightarrow A^{++}\left(v^{-1}v^{-1}\right) + e^{-} + e^{-}$$

where $A^{+}\left(c^{-1}\right) + e^{-}$ represent the intermediate state where a core-hole is produced in the target and an electron is in the continuum. For this core-ionised state the decay, for our purpose, is driven by an Auger emission. This is the case in the Auger PhotoElectron Coincidence Spectroscopy (APECS) [27].

Written in this form, the reaction can be interpreted in a two-step model where the Auger emission takes place from a stationary state and can be treated separately with respect to the preceeding photoionisation process, hence this is possible only if the core-hole lifetime is long enough to allow the relaxation of the other excitations, otherwise a one-step process, with the emission of two electrons sharing the excess energy, follows the photon absorption [28, 29, 30].

In an APECS experiment two electrons out-coming from the sample and generated in a unique radiation-matter interaction event are collected in a time-correlated and energy-resolved fashion. After the photon absorption a photoelectron is emitted in the continuum and the sample goes in a core-ionised state. In the target, via an autoionisation process driven by Coulomb interaction, the core-hole decays leading to the emission of a second, Auger, electron coupled to the first one. The photoemission process, when the photoelectron is discriminated in angle with respect to linear polarisation, prepares a proper subset of core-ionised states in the target. The collection of Auger electrons in time coincidence with photoelectrons of a specific energy allows to measure the partial Auger yield associated to the decay channel of only that particular subset of ionised states.

It is clear that such an experimental approach highlights 2-electrons and 2-holes material properties, in other words properties of both the electron-pair in the continuum and the interacting final state holes in valence band (or levels) must be described via a 2-quasi-particle wavefunction. For this reason the interpretation of correlation spectroscopies results are related to a 2-particle density of states (2-DOS). Theoretical works devoted to the determination of 2-DOS have made their appearance since late '70s with the pioneering works of Cini and Sawatzky [31, 32] undergoing later developments to be suitable not only for closed shells [33].

How APECS can access magnetic properties from a local viewpoint

As mentioned before, *d*-electrons and *d*-holes dictate the magnetic properties for transition metals and their oxides. For this reason it is fundamental to probe the behaviour of their valence electrons. Magnetic quantum numbers of the two, or more, final state holes are related to those of the ejected electrons, which are responsible, through their spin coupling, for the magnetic properties of the system. Hence, probing the *d*-holes spin coupling, magnetic information can be unravelled.

The angular electron emission is such that electrons characterised by partial waves with different projections m of the angular momentum, i.e. electrons belonging to different magnetic sublevels, are mainly emitted at different angles with respect to the electric vector of linearly polarised light, which acts as quantisation axis [29, figure 4]. Both the selection rules for the photoemission process[2] and for the Auger [34] put in correlation the magnetic quantum numbers of the partial waves of the emitted electrons with those of the valence holes in the final state [29]. In this way, combining the angular emission pattern with the selection rules, it is straightforward to differently weighting individual total spin contributions to the final state without any spin detection, but just collecting electrons under different kinematic conditions. Hence performing APECS experiments in an Angle-Resolved fashion (AR-APECS), that means upon changing the experimental geometry, leads to collect electron-pairs arising from different multiplet spin terms[3].

It has been shown recently by Stefani and co-workers [35] how the application of this coincidence spectroscopy to magnetic systems makes possible to get information about their magnetic state. The spectral difference in AR-APECS spectra collected in different kinematics gives a Dichroic Effect called DEAR-APECS, by means of which it is possible to access the final state holes spin configuration [36] unravelling individual multiplet contributions to the Auger spectrum. It has been shown that the DEAR-APECS effect is sensitive to the magnetic order of the systems under investigation, i.e. while it is present when a magnetic sample is below its phase transition temperature, it disappears exceeding such a value [37].

APECS is a core-excitation based technique and, in the same manner of other core-emission based spectroscopies, has a correlation length dictated by the spatial extension of the core-hole wavefunction. This means that APECS brings informations on the systems at atomic scale. This makes APECS a powerful tool to probe and monitor the magnetic phase transition from a local viewpoint overcoming limitations induced by the necessity of long-range order required by most electron spectroscopies and without having to rely on crystal periodicity or thermodynamical issues.

This work is devoted to the study of electron correlation in strongly cor-

[2]Optical dipole selection rules: $\Delta l = \pm 1$ with l angular momentum and $\Delta m = 0$ in the case of linearly polarised light.

[3]When two or more spins of interacting quasi-particles are coupled the angular momenta combination rules give back more than one total-spin state. For example combining two $|\frac{1}{2}\rangle$ spins the total spins accessible are $|0\rangle$ and $|1\rangle$ the well known Singlet and Triplet states. In the same way combining for example four $|\frac{1}{2}\rangle$ spins besides the Singlet and Triplet contributions rises the Quintet one. When considered in their totality these spin states are known as *spins' multiplets*.

related systems like magnetic thin films in the few monolayers regime. We performed AR-APECS experiments on both FM and AFM systems in order to unravel spin multiplets and the effects of electron correlation on the final state spin contributions. Exploiting both the local sensitivity and the spin selectivity of the AR-APECS will be possible to contribute to the issue about the loss of short-range magnetic order exceeding the transition temperature for both FM and AFM systems.

Chapter 1

Magnetic properties of solids

Man's encounter with magnetism is rooted in ancient time. A first hint of such a still vivid relation is given in the "Thales of Miletus" (about 634-546 BC) in which the fascinating property of the "lodestone", today commonly called magnetite, Fe_3O_4, of attracting iron was first described. History of magnetism found location also in China where the first instrument known to be a compass found its birth: it has been realised modeling a piece of lodestone into a spoon shape and placing it onto a bronze plate, as reported in figure 1.1. The handle of this spoon pointed, misteriously, to the South. Pliny the Elder (23-79 AD) in his *Historia Naturalis* traces the term magnet to a shepherd called Magnes, who discovered the "attractive" power of some stones putting his iron-nailed cane on the ground. Maybe the most important medieval study on magnetism still remain the epistle "De Magnete" by Peter Peregrinus (title page in figure 1.2a) which introduces the concept of magnetic poles, but starting from 1600 AD the reference text was the "De Magnete" by William Gilbert (title page in figure 1.2b). Nowadays magnetism is one of the most important field of research because it affects our everyday-life. This fact gives to magnetism a special place and a new vitality, also due to the fact that is a field that is still undergoing developments.

1.1 Magnetism in three-dimensional systems

Magnetic material are with no doubts among the most important and intriguing materials in nature and a microscopic investigation of such phenomenon is of pivotal interest. A magnetic medium can be described exploiting the so called constitutive equations, particularly by means of the magnetic permeability μ and the susceptibility χ. Such quantities are related to the magnetic field H, the magnetic induction B and the magnetisation M according to the

Figure 1.1: Working model of the first instrument known as a compass composed by a magnetic lodestone spoon and a bronze plate. Image from the web.

(a) Title page of the epistle *De Magnete* by Peter Peregrinus in 1296 in the reprint of 1558, Gasser ed. Germany. Figure from the web.

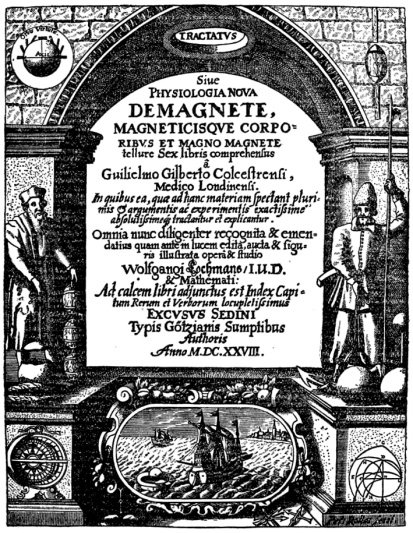

(b) Title page of the "De Magnete" by William Gilbert in 1600. Figure from the web.

Figure 1.2: Title pages of the *De Magnete*.

following equations [38, p. 15]:

$$\begin{aligned} \vec{B} &= \mu\vec{H} \\ \vec{M} &= \chi\vec{H} \\ \vec{B} &= \vec{H} + 4\pi\vec{M} = (1 + 4\pi\chi)\vec{H}. \end{aligned}$$

From a macroscopic viewpoint the magnetisation M represents the linear response to the application of an external field and it finds its origin in the magnetisation current induced by the action of the Lorentz's force upon the charges constituting the system. From this viewpoint a preliminary, but not satisfactory, connection with the microscopic nature of magnetism can be seen. For this reason the susceptibility represents a quantity able to discriminate upon different magnetic behaviors, allowing to classification of different magnetic materials.

$\chi < 0$	Diamagnetic	i.e. He, Ne, NaCl, Cu
$0 < \chi << 1$	Paramagnetic (PM)	i.e. Na, Al
	Antiferromagnetic (AFM)	i.e. NiO, FeO
$\chi >> 1$	Ferromagnetic (FM)	i.e. Fe, Co, Ni
	Ferrimagnetic (Fim)	i.e. Fe_3O_4

A diamagnetic substance, once immersed in an external magnetic field, reacts producing a magnetic moment opposite to the field, thus showing a negative susceptibility. The classical theory was formalised by Langevin in 1905 [39] on the base of the work of Ampére and Weber. In the same paper Langevin put down the theory for paramagnetic systems. In this case he assumed the same net magnetic moment μ for each atom of the specimen. These magnetic moments result randomised in the absence of an applied field, so the net magnetization of the sample is zero. If an external field is applied, these atomic moments tend to align to the field direction, but thermal agitation of the atoms opposes this tendency and randomises the moments. The result is only propensity to the alignment in the field direction, and therefore only a small positive susceptibility is obtained. Upon increasing the temperature this randomising effect is increased. Ferromagnetic and antiferromagnetic are indeed substances which in the high-temperature regime

show a paramagnetic behavior, but at low temperature (lower than a critical value characteristic for each system) they show a magnetic order even in absence of an external applied field. In the case of a ferromagnetic material this order is accompanied by a large net spontaneous magnetisation, on the contrary for an antiferromagnetic system the net magnetisation is null at any temperature, so it is possible to distinguish it from a paramagnetic specimen only with a very close investigation in a wide temperature range. Ferrimagnetism is the case of double oxide of iron and other metals. Like ferromagnetic materials they show a net spontaneous magnetisation which rises from a particular spin alignment: spins are coupled antiferromagnetically but the two FM sublattices show different magnitude. Because of these reasons they are a class apart.

In the following we will examine the intensive properties such as susceptibility and saturation magnetisation of Ferromagnetic and Antiferromagnetic substances, which are relevant for technological applications and are the kind of magnetic substances investigated in this thesis. These properties are not dependent on details of structural elements like lattice imperfections, grain size, crystal orientation or presence of impurities. Following the temperature dependence of such quantities a great clue on the magnetic nature of these systems can be achieved.

1.1.1 Ferromagnetism

Some substances, very common indeed like Iron or Cobalt, have shown a particular behavior with respect to others magnetic systems. A typical paramagnet is characterised by a net magnetisation if dived into an external magnetic field, but it shows no magnetism once removed from the field, while for a ferromagnet a magnetic ordering is preserved even if no external magnetic field is applied. Such substances are termed as Ferromagnet or Antiferromagnet. For these systems the existence of a spontaneous magnetic order suggests that their ground state must be characterised by a well defined orientation of the magnetic dipoles. Such dipoles can be very large and they are responsible for the macroscopic permanent net magnetisation. This magnetic order can be removed only heating the sample exceeding a certain temperature, typical for each system, termed as critical temperature, T_c. This temperature acts as watershed between the (Anti-) Ferromagnetic state and the paramagnetic one. In order to get more details on the nature of the interaction responsible for this behavior, let us refer to table 1.1 in which the magnetisation at $T = 0$ K, the magnetic moment and the critical temperature are given. In a magnetic system the dipole-dipole interaction has the tendency to line up the dipoles: a dipole influenced by the dipolar field of another magnetic

	M @ $T = 0$ K (gauss)	$\frac{\mu}{\mu_B}$	T_c (K)
Fe	1752	2.219	1043
Co	1446	1.715	1394
Ni	510	0.604	630
Gd	1980	7.12	293

Table 1.1: Magnetisation, magnetic moment and Curie temperature for the most common ferromagnets. Values from [40, chapter XVII].

dipole is affected by a torque which tends to align this two dipoles. Such an interaction is of the form $\sim \frac{\mu_1 \mu_2}{r^3}$ and it is possible to estimate typical energy contribution of this classical interaction of the order of ~ 0.1 meV. The critical temperature (or Curie temperature for a ferromagnet) reported in table 1.1 are of the order of ~ 100 meV, hence they cannot be interpreted in terms of the dipole-dipole interaction. No real progress in understanding magnetism was made until P. Weiss proposed the idea of an internal field usually called molecular field [41] responsible for the dipole alignment. In such a mean field theory the magnetisation is not only due to the external field, but a molecular field play a role:

$$H_{\text{eff}} = H + \lambda M$$

where the last terms takes into account for this field generated by the aligned dipoles. Under this assumption the magnetisation can be expressed as [40, chapter XVII]

$$M = \frac{N}{V} \mu_0 tgh \left[\frac{\mu_0 (H + \lambda M)}{K_B T} \right] \tag{1.1}$$

where M is the magnetisation, $\mu_0 = g \mu_B J$ is the magnetic moment given as the product of the gyromagnetic factor g, the Bohr magneton and the total angular momentum of the ion, $\frac{N}{V}$ the number density of ions in the system and $K_B T$ the thermal energy. It has been considered the interesting case[1] for $J = \frac{1}{2}$ and $g = 2$ instead of using the complete Brillouin function for the sake of simplicity. This equation allows to determine the magnetisation of a ferromagnet in absence of the external field, $H = 0$. Under this restriction equation (1.1) is reduced to:

$$M = \frac{N}{V} \mu_0 tgh \left(\frac{\mu_0 \lambda M}{K_B T} \right). \tag{1.2}$$

[1] See figure 1.5

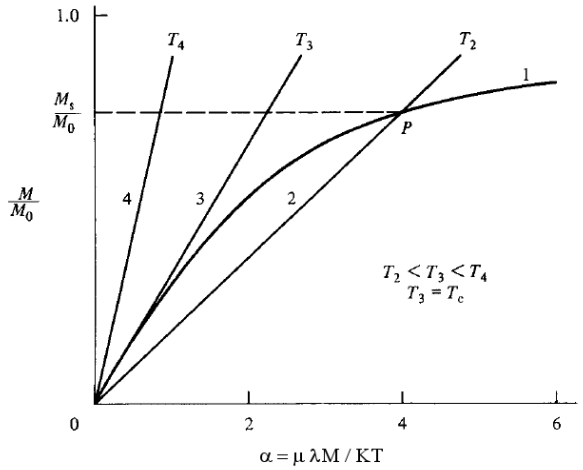

Figure 1.3: The solution of equation (1.3) is given in figure in terms of relative magnetisation as a function of the dimensionless α parameter. Curve 1 is the Langevin function. Solutions for three temperature values are given. Image redrawn from [38].

Such an equation has a standard way to be solved: defining $\alpha = \frac{\mu_0 \lambda M}{K_B T}$ and $T_c = \frac{\mu_0^2 \lambda N}{V K_B}$ equation (1.2) can be rewritten as

$$tgh(\alpha) = \alpha \frac{T}{T_c} \tag{1.3}$$

which can be graphically solved as given in figure 1.3: the Langevin curve labeled as 1, that represents the relative magnetisation (here M_0 is the saturation magnetisation), is reported with a plot of equation (1.3) for three different temperatures T_2, T_3 and T_4 in the $T_2 < T_3 < T_4$ relation. In the case $T = T_3 = T_c$ the straight line is tangent to the Langevin function in $\alpha = 0$ so the slope of line 3 determines the Curie temperature of the system. Increasing the temperature, as in the case of line 4, the only intersection point between this two curves is in the origin, i.e. the case $M = 0$ that is not of interest. The most intriguing case is given by line 2 for which a non trivial solution for equation (1.3) is present. The point P represents the spontaneous magnetisation, expressed as a fraction of the saturation value, achieved at that temperature.

Let us now focus only on the solution at $T = T_2$. The trivial solution $M = 0$ represents an unstable state because the slightest applied field, e.g. the Earth's field, will magnetize the system to a certain point, A in figure 1.4. At this point a magnetsation $M = A$ must be due to a molecular field

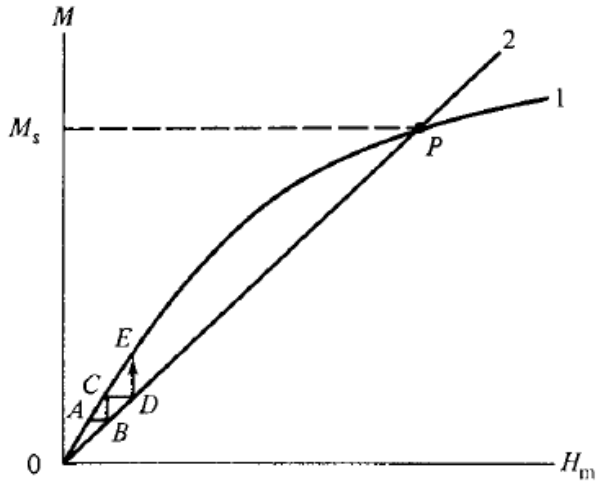

Figure 1.4: Schematic representation of the spontaneous magnetisation process due to the molecular field. Image from [38].

$H_m = \lambda M = B$ in reference to figure 1.4. Anyway such a field must produce a magnetsation $M = C$ and so on up to the point P that represent a stable point at which the sample results spontaneously magnetised. The magnetisation of these ferromagnetic systems as a function of the temperature shows a trend similar to those reported in figure 1.5. In such a figure $\frac{\sigma_s}{\sigma_0}$ expresses the magnetisation in terms of the specific magnetisation according to the relations [38]

$$\begin{aligned} \frac{\sigma_s}{\sigma_0} &= \frac{M_s \rho_0}{M_0 \rho_s} \\ \frac{\sigma}{\sigma_0} &= \left(\frac{J+1}{3J}\right)\left(\frac{T}{T_c}\right)\alpha' \\ \alpha' &= \frac{\mu_H H}{K_B T} \end{aligned}$$

where $\rho_{s(0)}$ is the density of the system at temperature T ($T = 0$ K), J is the total angular momentum of the ion and μ_H the projection along the field of the magnetic moment. Figure 1.5 clarify the role of the critical temperature T_c, while the system taken below such a value shows a spontaneous magnetisation, on the contrary it shows no magnetic order exceeding that critical point. Of course this two different magnetic states follow two different laws: approaching the Curie temperature from below the magnetisation scales with a power law temperature dependence, while approaching it from above the typical Curie-Weiss law describes the paramagnetic behavior shown by the

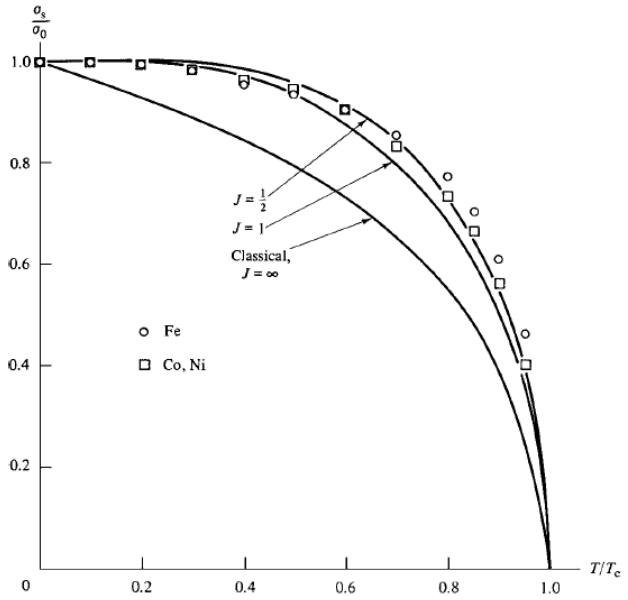

Figure 1.5: Relative saturation magnetisation as a function of the temperature for Iron, Nickel and Cobalt. The solid lines are calculations for different values of the total angular momentum J. Image from [38].

system [40, chapter XVII]

$$\begin{cases} M = \frac{N}{V}\mu_0 \frac{T}{T_c}\sqrt{3\left(1-\frac{T}{T_c}\right)} & \text{if} \quad T \to T_c^- \\ M = \frac{N}{V}\frac{\mu_0^2 H}{K_B(T-T_c)} & \text{if} \quad T \to T_c^+. \end{cases}$$

Figure 1.5 gives also information about the angular momentum, J, dependence of the magnetisation: the best agreement between the experimental values an the theoretical calculations is obtained for the total angular momentum $J = \frac{1}{2}$ that means the magnetic moment is entirely due to the spins, with no orbital contribution. Hence it is possible to state that ferromagnetism in transition metals is due essentially to electron spin [38].

The Weiss theory of the molecular field gives no explanation about the origin of this field, simply it relates via a proportionality law this field and the existing magnetisation, underlining the cooperative nature of the phenomenon, as shown also in figure 1.5 in which the spontaneous magnetisation decreases upon the increasing of the temperature. Only in 1928 this origin started to be understood, with the brilliant hypothesis by Heisenberg, who proposed that the spin alignment throughout the solid was due to the exchange interaction, so a purely quantum effect with macroscopic manifestation. Exchange forces depend on the relative spin orientation of two

interacting electrons. It is a consequence of the Pauli exclusion principle[2] applied to these two interacting electrons as a whole system. According to this principle these two electrons cannot occupy the same energy level unless they are provided of two opposite spins. This interaction arises from the Coulomb force, so it has basically an electrostatic origin.

Let us suppose two different atomic sites labeled as A and B. The total Hamiltonian can be expressed as

$$H_A + H_B + H_{1,2}$$

considering $H_{A\,(B)}$ the single-particle Hamiltonian for an electron in the atomic site A (B) and where

$$H_{1,2} = -\frac{e^2}{|\vec{r_1} - \vec{r_B}|} - \frac{e^2}{|\vec{r_2} - \vec{r_A}|} + \frac{e^2}{|\vec{r_1} - \vec{r_2}|}.$$

The two-electrons Hamiltonian allows two different total spin states, the Singlet with $S = 0$ and the Triplet with $S = 1$, energy shifted by twice the exchange integral [40, chapter XVII]

$$E(S = 0) - E(S = 1) = 2J_{ex}.$$

Heisenberg intuition was to attribute ferromagnetism to the direct spin-spin interaction that can be described with an Hamiltonian term like

$$H = -\sum_{m \neq n} J_{mn}^{ex} \vec{S_m} \cdot \vec{S_n}.$$

Exchange interaction drops rapidly to zero upon increasing the separation between the two interacting electrons, thus it is possible to simplify this term reducing the sum over all the possible atomic site to the nearest-neighbor. In the simplest case let us consider only the z-component (along the quantisation axis) of the spin. Assuming also that the exchange integral is the same for all these neighbours, that means assuming an isotropic substance, the Heisenberg model is reduced to the Ising one:

$$H_{\mathrm{I}} = -J_{ex} \sum_{m,i} S_m^z S_{m+i}^z \tag{1.4}$$

where the index m runs over all the atomic sites and i over the nearest-neighbours. It is clear that a positive exchange integral, which is a rare

[2]The name *exchange* comes from the fact that two electrons are completely indistinguishable so the energy contribution in which they exchange their role must be accounted for.

condition, is necessary for a ferromagnetic alignment of the spins, because if $J_{ex} > 0$ a parallel alignment of the spins leads to a minimum in the exchange energy, on the contrary in the case of $J_{ex} < 0$ an antiparallel, antiferromagnetic, alignment is favored. Of course the exchange integral, if positive, is proportional to the Curie temperature. This is very simple to understand because it requires a large thermal energy to destroy the spin alignment held by a strong exchange interaction. Anyway it is possible to put this statement on a more quantitative ground [38]:

$$J_{ex} = \frac{3K_B T_c}{2zS(S+1)}$$

where z is the coordination number, i.e. the nearest-neighbor, and S the spin. Exchange forces depend mainly on interatomic distances and not on any geometrical arrangement of the atomic sites, thus crystallinity is not a required condition for forromagnetism. The first discovery of ferromagnetism in an amorphous sample goes back to 1965 [42].

In discussing about the spin alignment in a ferromagnet a marginal role has been given to the dipole-dipole interaction. Such a classical interaction term contribute with an energy given by [38, p. 365]:

$$\Delta E = \frac{\vec{\mu_1}\vec{\mu_2}}{r^3} - \frac{3}{r^3}(\vec{\mu_1} \cdot \hat{r})(\vec{\mu_2} \cdot \hat{r})$$

where $\vec{r}$ is the distance between the two dipoles $\vec{\mu_1}$ and $\vec{\mu_2}$. This dipolar interaction drops to zero as $\frac{1}{r^3}$ slower with respect to the exchange integral and at a macroscopic level it is responsible for the formation of the so called "Weiss domains". A Weiss domain is a portion of the sample in which a certain number of spins are aligned to each other, but two adjacent domains can have two different orientation of the net magnetic moment. This is due to the fact that the exchange interaction forces the spins to lie parallel to each other, but a configuration with all the spins aligned is not favored by the dipole-dipole term. Thus a proper balance of this two contribution leads to the formation of different domains in order to gain energy from the dipole-dipole interaction among different domains and the gain from the spin coupling inside a single domain. The only expenses are in the formation of the separation surfaces between domains, the so called "domain walls".

This domain structure is able to account for the absence of spontaneous magnetisation in a ferromagnet above the Curie temperature: starting with a system showing a net magnetisation, i.e. there is a propensity in the domain alignment, upon increasing the temperature the orientation of the different domains starts to randomise, reaching a condition of a null average net magnetisation once approached the Curie point.

The Stoner model: a brief description

In the previous paragraph a brief description of the local Weiss theory for ferromagnetism has been given. Such a theory for the $3d$-transition metal is adequately integrated by a so called band theory. The simplest band-model is often referred as Stoner-Wohlfarth-Slater-model (SWS-model) which is based on the one-electron density of state considering separately for the two possible spin orientation (up ($\uparrow$) or down ($\downarrow$)). Due to the exchange interaction which prevents that an electron can be approached from another with the same spin, the effective charge density of electrons with the same spin orientation in the neighborhood is reduced. In the Stoner model this is taken into account introducing an energy renormalisation as follow [43, chapter 9 section 4]:

$$E_{\uparrow}(\vec{k}) = E(\vec{k}) - \frac{In_{\uparrow}}{N}$$
$$E_{\downarrow}(\vec{k}) = E(\vec{k}) - \frac{In_{\downarrow}}{N}$$

where $E(\vec{k})$ are the normal one-electron energy-bands, $n_{\uparrow\,(\downarrow)}$ the number of electrons with the corresponding spin and N the total number of atoms. The exchange correlation effect is taken into account with the Stoner parameter I. A k-independent subband splitting results from this model as depicted in figure 1.6. In the presence of a molecular field the centers of the two subbands with opposite spins are separated by the exchange splitting Δ. At $T = 0$ K all the electron states are filled up to the Fermi level, so it results convenient to refers to electrons as *majority* or *minority*, according to the excess of one kind of spins with respect to the other. The microscopic ferromagnetic moment originates from the excess of majority spin over the number of minority spins:

$$|\vec{m}| = \mu_B(n_{\mathrm{maj}} - n_{\mathrm{min}}).$$

The occurrence of spontaneous magnetism below T_c can be explained as follow [43, pp. 477-478]: local fluctuations in the spin orientation below the Curie point lead to a momentary polarisation responsible for the spin alignment into a magnetic order, which in turn is responsible, because of energetics, of the majority and minority band splitting.

1.1.2 Antiferromagnetism

Besides the ferromagnetism there is another intriguing type of magnetic order termed as antiferromagnetism. An antiferromagnet (AFM) is a substance

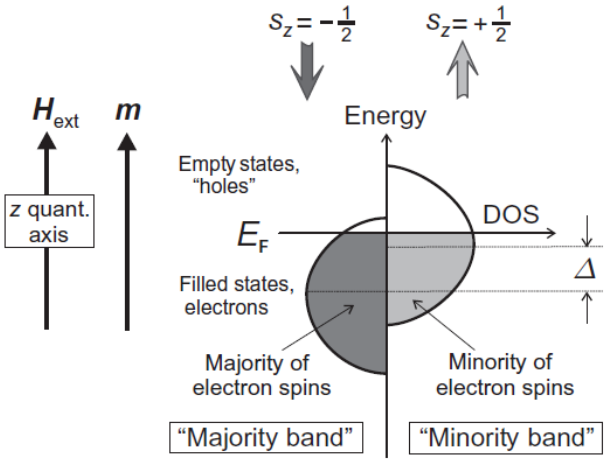

Figure 1.6: The Stoner model for the 3d-metal is reported. Occupied electron states below the Fermi energy E_F are shown shaded. The spin band with the largest number of electrons is termed as *majority spin band*, the other as *minority*. The centers of the two subbands are separated by the exchange splitting Δ. The labels "spin-up" and "spin-down" only have a meaning in conjunction with a quantization direction, which is taken to be the direction of the external field. Minority spins always point in the direction of the magnetisation M. The magnetic moment $|\vec{m}|$ is determined by the difference in the number of majority and minority spins. Image from [44, chapter 7].

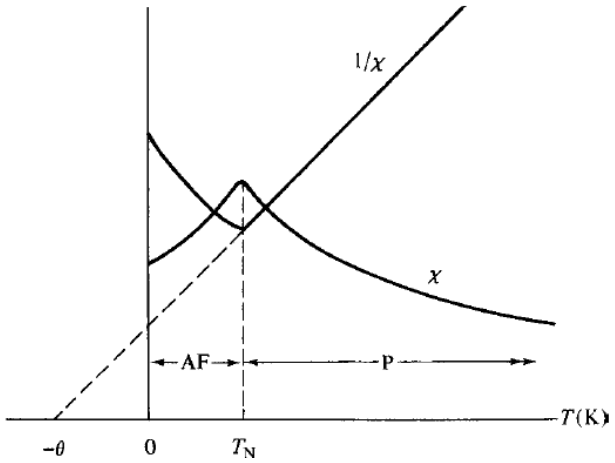

Figure 1.7: Temperature dependence of susceptibility and its inverse for an AFM system: schematic representation. AF and P refer to antiferromagnetic and paramagnetic respectively. θ is the temperature value, proportional to the molecular field, at which the susceptibility diverges in the Curie-Weiss law. The Néel temperature T_N is also reported. Image from [38, chapter 5].

characterised by a susceptibility[3] which varies in a peculiar way with the temperature, appearing, at first glance, like an anomalous paramagnet. In figure 1.7 the susceptibility χ as a function of the temperature in an AFM is reported. Starting from the high-temperature limit, the susceptibility increases as the temperature decreases, reaching a maximum at a critical temperature called *Néel temperature*, T_N. Going further in decreasing the temperature under T_N the susceptibility starts to decrease. Closer studies have put in evidence that such systems requires a proper classification. Such substances show themselves as a paramagnet above T_N and as an AFM below it. Transition metal oxides are one of such a kind of systems and some values for their T_N are given in table 1.2.

The theory about antiferromagnetism found its origin in 1932 with the work of L. Néel [45]. In his work he applied the Weiss molecular field theory, discussed above, to the problem of antiferromagnetism. In figure 1.7 the straight dashed line extrapolates to a negative temperature at $\frac{1}{\chi} = 0$

$$\chi = \frac{C}{T + \theta} = \frac{C}{T - (-\theta)}$$

in other words obeying the Curie-Weiss law but with a negative temperature.

[3] In general, upon application of an external magnetic field H, a specimen acquires a magnetisation M. The magnetic susceptibility is defined as $\chi = \frac{\partial M}{\partial H}$.

	Metal ion arrangement	T_N (K)	$-\theta$ (K)
FeO	fcc	198	570
CoO	fcc	293	280
NiO	fcc	523	3000
MnO	fcc	122	610

Table 1.2: Crystal symmetry, Néel temperature and $-\theta$ temperature extrapolation for the most common transition metal oxides antiferromagnets. Values from [38, chapter 5].

$\theta = \rho C \gamma$ hence is proportional to the molecular field coefficient (see ref. [38, p. 97, eqn (3.22)]) and this means that in the paramagnetic region the molecular field is opposite to the applied field H; whereas H tends to align the ionic moments the molecular field acts to disalign them. At atomic scale any tendency of ionic moment to point in one direction is immediately counteracted by the tendency of the adjacent moment to point in the opposite direction [38, chapter 5]. According to equation (1.4) such systems have a negative exchange integral. Below the critical temperature this tendency to align in antiparallel fashion the magnetic moments throughout the solid is strong enough to survive the thermal energy even with no applied field. Such a strength increases upon decreasing the temperature below T_N down to $T = 0$ K where the antiparallel alignment results perfect. It is now clear that an AFM system has no spontaneous net magnetisation and can acquire a moment only under the effect of a high external magnetic field. It is also clear that the Néel temperature T_N play a role equivalent to the Curie temperature for a ferromagnet dividing the magnetic ordered phase and the paramagnetic one.

Almost all AFM systems are electrically insulators or semiconductors. This means that they contain no free charges, hence their magnetism is dictated by localised electrons belonging particular ions. Therefore the molecular field theory, that is a localised-moment theory, is expected to better fit the case of antiferromagnetism with respect to the ferromagnetism [38, p. 154]. Let us divide the entire AFM lattice in two identical sublattices, namely A and B, such that all nearest-neignbours of sublattice A are B sites and vice versa. In doing so only the magnetic ions arrangement is taken into account. In both of these sublattices a ferromagnetic arrangement is present. In the case of a simple cubic whole lattice two interpenetrating fcc (face-centered cubic) sublattices in the well-known NaCl structure are obtained for A and B, while in the case of a compete bcc (body-centered cubic) lattice the re-

sulting sublattices A and B show a simple cubic structure. In the case of the entire AFM lattice is fcc there is no simple partition for the two sublattices A and B in order to get all nearest-neighbors of an A site belonging to B and vice versa [40, p. 635]. The Weiss theory can be applied to each sublattice assuming that the effective field acting on a site A contains a cooperative contribution proportional and opposite to the magnetisation on the B sublattice and vice versa. Let us also assume that the nearest-neighbor interaction is of the type AB (BA) and the second-nearest-neighbor, AA (BB), is again antiferromagnetic. In this case we have *two* molecular fields to deal with [38, chapter 5]:

$$\begin{aligned} H_{\mathrm{mA}} &= \lambda M_{\mathrm{B}} \\ H_{\mathrm{mB}} &= \lambda M_{\mathrm{A}}. \end{aligned}$$

So the effective field on the two sublattices are [40, chapter XVII]:

$$\begin{aligned} \vec{H}_{\mathrm{A}}^{(\mathrm{eff})} &= \vec{H} - \lambda_1 \vec{M}_{\mathrm{B}} - \lambda_2 \vec{M}_{\mathrm{A}} \\ \vec{H}_{\mathrm{B}}^{(\mathrm{eff})} &= \vec{H} - \lambda_1 \vec{M}_{\mathrm{A}} - \lambda_2 \vec{M}_{\mathrm{B}} \end{aligned} \tag{1.5}$$

where H is the external field, $M_{\mathrm{A(B)}}$ the magnetisation of sublattice A (B) and λ_1, λ_2 two positive phenomenological constants (λ_2 can be also null or negative, but $|\lambda_2| < \lambda_1$) which account for the first- and second-nearest-neighbor interaction respectively.

It must be taken into account that once applied a field above T_N each sublattice becomes magnetised in the same direction of the applied field, but the molecular fields act in the opposite direction of the applied field reducing the two sublattice, i.e. the net, magnetisation with respect to the case of an ideal paramagnet. In this condition the susceptibility of the systems follows the Curie-Weiss law but results reduced with respect to the non-interacting case ($\lambda_1 = \lambda_2 = 0 = \theta$) as expressed in the following equation [40, chapter XVII] and graphically in figure 1.8:

$$\begin{aligned} \chi &= \frac{M}{H} = \frac{C}{T+\theta} \\ \theta &= C\frac{\lambda_1 + \lambda_2}{2}. \end{aligned} \tag{1.6}$$

In the temperature region below T_N a spontaneous magnetisation for each sublattice, even in the absence of an external applied field, is expected. Because of the net magnetisation of an AFM system is null at any temperature the following condition must be satisfied:

$$M_{\mathrm{A}} = -M_{\mathrm{B}}$$

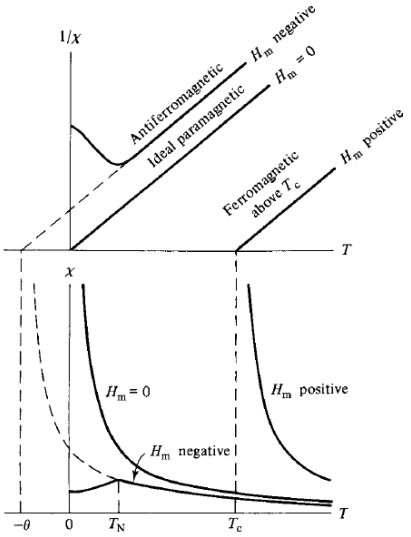

Figure 1.8: Molecular field dependence of susceptibility (lower panel) and its inverse (upper panel) for an AFM system: schematic representation for H_m greater, lesser and equal to 0. Image from [38, chapter 5].

and the magnetisation can be derived from equation (1.5). In this case the Néel temperature reads [40, chapter XVII]:

$$T_N = C\frac{\lambda_1 - \lambda_2}{2} \tag{1.7}$$

hence from equations (1.6) and (1.7) it straigthfarward to derive:

$$\frac{T_N}{\theta} = \frac{\lambda_1 - \lambda_2}{\lambda_1 + \lambda_2}. \tag{1.8}$$

In the case the second-nearest-neighbor antiferromagnetic interactions (AA and BB) are negligible, i.e. putting $\lambda_2 = 0$ in equation (1.8), $\theta = T_N$, so T_N play the same role of the Curie temperature in a ferromagnet.

Although a net spontaneous magnetisation is zero below T_N, a small magnetisation can be driven by the application of an external field. In such condition the susceptibility has been found to depend upon the angle between the applied field and the axis of antiparallelism of the magnetic moment, i.e. the axis at which the two spins lie. This last statement is supported by the fact that in most of the AFM systems the orbital contribution results entirely quenched, so the magnetic moment founds its origin essentially in the spin contribution [38, p. 157].

1.1.3 Indirect exchange

The magnetic interaction discussed above is known as *direct exchange* because it arises from the direct wavefunction overlap among electrons from two ions. This is not the unique force in magnetism, because often happens that two magnetic ions are separated by a non magnetic one (with all the electronic shells closed). In this case for the two magnetic ions exist the possibility to have a magnetic interaction mediated by the electron cloud of the non magnetic intermediate. Such an interaction is extended more than the short-range direct exchange and for this reason is usually termed as *superexchange*. In this type of interaction, first pointed out by Kramers in 1934 [46] and then formalised by Anderson in 1950 [47], the wavefunction of the magnetic atom overlaps with the wavefunction of a non magnetic intermediate ion which in turns has its own wavefunction overlapped to the one of the other nearest-neighbor magnetic atom. Such an interaction is typical for the $3d$-metal oxides, like NiO. For these systems the bonding are formed by the $3d$-electrons of the metal and the $2p$-valence electrons of the ligand oxygen. Exploiting a Hubbard approach for the superexchange it is possible to show that the ground state for these systems provides an antiferromagnetic spin alignment [44]. Let us assume that the electronegativity of the Oxygen in a transition metal oxide is strong enough to maintain unchanged its electron arrangement to the O^{-2} configuration. In an oversimplified way, for an electron belonging to a metal ion the hopping to another metal ion is allowed only in an antiferromagnetic alignment of the spins because of the Pauli exclusion principle. This antiferromagnetic state offers new degrees of freedom with respect to the one in which a parallel spin alignment is provided, so electrons can lower the total energy by delocalising.

Another source of magnetic interaction, that involves electrons in the conduction band, is the so called *itinerant exchange*. In this case the electrons involved in ferromagnetism are considered to belong to the crystal as a whole and to be able to move from an atom to another. Such a theory is capable to account for the relative magnitude of the dipole magnetic moment in Iron, Cobalt and Nickel and it results a good support to the band theory of ferromagnetism, not detailed here. The localised spin picture fails in describing transition metals with partially filled d-bands because of the itinerant character of these electrons. A physical picture that describes electrons in term of Bloch functions plus correlation terms is desirable. A prototype model for itinerant ferromagnetism is the Stoner-Hubbard Hamiltonian [40, p. 659]:

$$H = \sum_{\vec{k}} E\left(\vec{k}\right)\left[c^{+}_{\vec{k}\uparrow}c_{\vec{k}\uparrow} + c^{+}_{\vec{k}\downarrow}c_{\vec{k}\downarrow}\right] + U\sum_{\vec{t_m}} c^{+}_{m\uparrow}c_{m\uparrow}c^{+}_{m\downarrow}c_{m\downarrow} \tag{1.9}$$

where $E\left(\vec{k}\right)$ are the conduction band energies, $c^{+}_{\vec{k}\sigma}$ and $c_{\vec{k}\sigma}$ the creation and annihilation operators for conduction electrons in the $\vec{k}$ state with spin σ, $c^{+}_{m\sigma}$ and $c_{m\sigma}$ have the same meaning but it is specified the lattice site $\vec{t_m}$ and finally U is a phenomenological parameter that quantify Coulomb repulsion among two electrons of opposite spins belonging to the same lattice site. Hamiltonian (1.9) can lead to macroscopic magnetic effect, particularly if U is negligible it allows for a non-magnetic ground state with the lowest lying $\frac{N}{2}$ orbital Bloch states doubly occupied (here N is the number of atom composing the crystal), on the contrary if the band dispersion is negligible, i.e. $E\left(\vec{k}\right) = E$, the ground state is magnetic with the states of one spin sub-band completely filled and the others completely empty [40, p. 659]. For an intermediate case, working at $T = 0$ K and in the so called "unrestricted Hartree-Fock approximation" where the operators $c^{+}_{m\sigma}$ and $c_{m\sigma}$ are replaced by their expectation value on the ground state, the susceptibility of the system can be expressed in terms of the density of states at the Fermi level $D(E_F)$ as [40, p. 660]:

$$\chi = \frac{1}{V}\frac{{\mu_B}^2 D(E_F)}{1 - \frac{1}{2}\frac{D(E_F)}{N}U}.$$

In the case $U = 0$ the Pauli magnetic susceptibility is regained, while it is increased when $U > 0$. In the case

$$\frac{1}{2}\frac{D(E_F)}{N}U = 1 \tag{1.10}$$

the magnetic susceptibility diverges and a ferromagnetic transition is expected.

1.2 Magnetism in thin films

Magnetism and magnetic materials are of great interest as they are a "complication" in the solid state physics. They are usually characterised by a complex electronic structure and they are dominated by electron correlation, usually neglected in conventional band theory.

The capability to deal with low dimensional systems has represented a relevant historical moment inasmuch it opened the way to the study of magnetic properties of surfaces and thin films. Of particular interest are ferromagnetic and antiferromagnetic films since they found application in technological devices. Surface magnetism is a wide field but in the following only some aspects will be discussed.

1.2.1 Surface vs. bulk magnetisation

Magnetic properties in reduced dimensions can be very different with respect to the ones of the corresponding bulk systems and this is because of the reduced coordination of surface atoms, the broken symmetry, and so on. The presence of a surface plays a crucial role in the case of low dimension systems, where one of the three dimensions is reduced for example to few times the extension of the exchange interaction. In (anti-) ferromagnetic systems the surface critical temperature can be largely lower if compared to the bulk value.

To highlight differences from bulk magnetism let us consider for example the temperature dependence of the surface magnetisation. It is convenient to approach the problem within a simple model of exchange coupling in the framework of mean field theory. Let us focus on the case $T \to T_c^-$, that means approaching the Curie point from below, in absence of any external field, that implies a magnetisation approaching zero. Under these assumption equation (1.3) can be inverted as follow:

$$M + \frac{M^3}{3} - \frac{T}{T_c}M = 0 \tag{1.11}$$

exploiting the Taylor's series of the $atgh(x)$ (arctangent) function. The solution of this equation leads to a bulk magnetisation

$$M \sim |T_c - T|^{\frac{1}{2}}.$$

Such a temperature dependence cannot explain the surface magnetisation as clearly shown in figure 1.9 where the magnetisation of the Fe (100) surface is reported as a function of the reduced temperature. As a comparison the bulk M vs. T curve is also reported. In the case of a surface the situation is certainly more complicated than in the bulk. In this case a surface exchange interaction must be considered. Such a term can be expressed in the form

$$J_s = J_b(1 - \Delta)$$

where the surface exchange integral J_s is given in terms of the bulk value J_b, here Δ represents the reduction term due to the reduced coordination. It is possible to demonstrate that under this assumption the temperature dependence of the magnetisation is expected to be linear [48]

$$M \simeq T_c - T$$

very close to the experimental behavior.

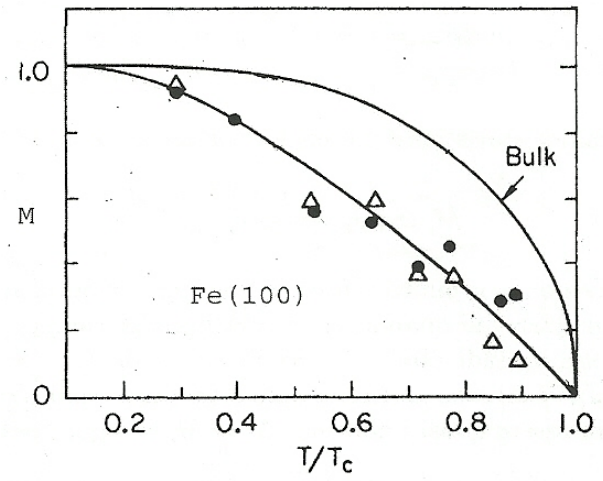

Figure 1.9: Magnetisation vs temperature for Fe (100) measured by spin polarised photoemission spectroscopy. The solid line superimposed to the experimental data is a layer dependent magnetisation curve calculated for the first atomic layer, the solid line marked as "bulk" represent the bulk magnetisation behavior. Image adapted from [49].

1.2.2 Thickness dependence of transition temperature and magnetic moment direction

The Stoner criterion for ferromagnetism expressed in equation (1.10) contains an important ingredient to understand magnetism in low-dimensional systems, the density of states at the Fermi level, $D(E_F)$. The DOS is dependendent on the interatomic wavefunctions overlap thus it depends on the coordination number. For this reason a modified DOS with respect to the bulk has to be expected in surfaces and thin films. Not only the electronic band structure but also the thermodynamical properties are influenced by the reduced dimensionality. The stabilisation of the ferromagnetic phase as a collective phenomenon is affected by the number of nearest-neighbor atoms, because a certain number of neighboring atoms is required to create an average magnetic moment high enough to induce, during fluctuations, the spin alignment. Also the critical temperature T_c at which the ferromagnetic order starts to disappear results modified with respect to the bulk value. According to the following expression [43, paragraph 9.4]

$$T_c = \frac{1}{4}\nu\frac{J}{K_B}$$

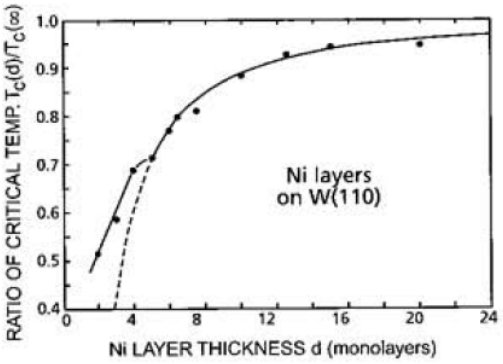

Figure 1.10: Thickness dependence of the critical point, referred to the bulk value $T_c(\infty)$, in Ni(111) grown on top of W(110). Dashed line is a theoretical fit (see reference for more details). Image from [50].

where J is the exchange integral, K_B the Boltzmann's constant and, most important, ν the number of coordinated atoms. Hence it is now evident that the critical point depends upon the dimensionality of the system and particularly for surfaces and thin films, where a lower coordination occurs, it is expected to be lower than the bulk value. Such a behavior has been experimentally verified. In figure 1.10 the Curie temperature for a Ni layer grown on top of a W(110) substrate measured via magnetic resonance is reported as a function of the layer thickness [50]. More recently, magnetic dichroism in X-ray absorption spectroscopy has been largely employed in the determination of the critical temperature in ferromagnetic as well as antiferromagnetic thin films. Particularly for antiferromagnets, like NiO, because of its macroscopic magnetisation is null at any temperature, very few techniques are useful. In such a case X-ray Magnetic Linear Dichroism (XMLD), sensitive to the square of the magnetisation, $\langle M^2 \rangle$, has proved a useful tool to determine the Néel temperature for films of different thickness as reported in figure 1.11. The magnetic information is carried out by the so called L_2 ratio which represents the asymmetry in the lineshape of the L_2 absorption edge due to the exchange interaction (as will be discussed in section 4.1.3): upon increasing the temperature this asymmetry is reduced down to a constant value once the Néel temperature is exceeded. Figure 1.11b puts in evidence also the role of the substrate in affecting the magnetic properties of thin films: in its bottom panel the same 3 ML-thick film of NiO shows a $T_N = 390$ K when grown on a silver substrate, while $T_N < 40$ K in the case of a MgO substrate [51, 52].

In the same works by Alders et al. [51] and Altieri et al. [52] another

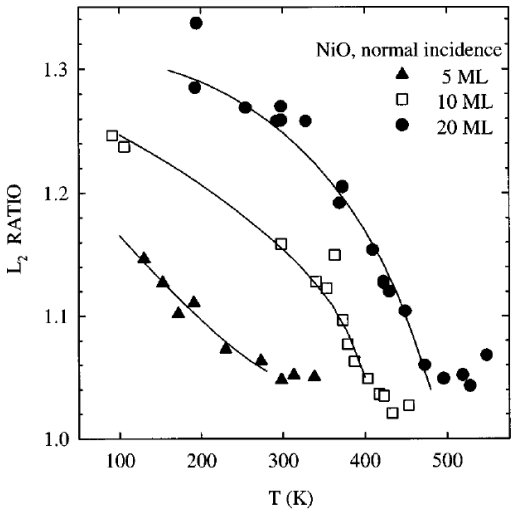

(a) Temperature and thickness dependence of the intensity ratio in Ni L_2-XAS doublet in NiO(100). A Néel temperature of $T_N = 295$, 430 and 470 K for 5, 10 and 20ML-thick films respectively have been found. From [51]

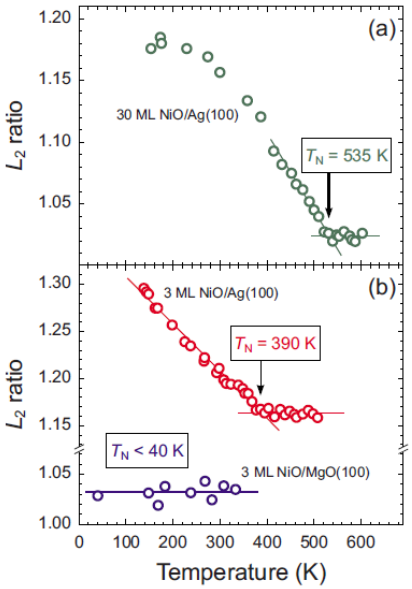

(b) Temperature dependence of the intensity ratio in Ni L_2-XAS doublet for 30 ML NiO(100)/Ag(100) (top) and 3 ML NiO(100)/Ag(100) (bottom, red) versus 3 ML NiO(100)/MgO(100) (bottom, blue). From [52].

Figure 1.11: Transition temperature determination in NiO using XMLD.

important characteristic of thin films is also shown: while for NiO/Ag the spins, hence the magnetisation, lie on the film plane, on the contrary for NiO/MgO such magnetisation results normal to the surface. This means that not only the critical temperature is affected by the reduction in the dimensionality of the system, but also the spin structure.

In the treatment for ferromagnetism and antiferromagnetism reported above an isotropic spin-coupling has been assumed. Anyway a rigorous theoretical treatment by Mermin and Wagner [53] shows that spontaneous magnetism does not occur in systems with two or lower dimension if only such an isotropic-coupling is taken into account. This result clearly is in contrast with the one in figure 1.10 where a magnetism with a lowered critical temperature for 2 ML-thick Ni film was observed. In order to solve this contradiction a *magnetic anisotropy* must be considered. This anisotropy is responsible for the stabilisation of the ferromagnetism in quasi-2D-systems [43, p. 484]. The dipole and spin-orbit interactions are responsible for the existence of directions of easy magnetisation and while in the isotropic-coupling the direction of the molecular field is arbitrary, on the contrary, if a magnetic anisotropy is invoked this field falls, below the critical temperature, along such directions. Particularly dipole interaction favors the spin alignment within the film plane, whereas spin-orbit coupling allows also for a perpendicular magnetisation. Spin orientation depends upon the anisotropy energy and the symmetry-breaking effect of a surface plays a crucial role: the lower the film thickness the greater the surface effect, so the orientation of the macroscopic moment is affected by the film thickness [43, p. 484]. What just said has been experimentally proved and in figure 1.12 a recent example for NiO is given as reported in [54]. In this work a multilayer of Iron and NiO is grown on the vicinal (1,1,10) Ag surface and the spin alignment both for Fe and NiO has been measured applying Magneto Optical Kerr Effect (MOKE) of the Fe layer. The results show a transition of the spin alignment from parallel to perpendicular orientation with respect to the Ag surface steps crossing a critical thickness of $d \sim 2.8$ nm.

Such a work, which reports the NiO case, summarises what just said above regarding both the thickness dependence of the critical temperature and the spin reorientation transition.

1.3 Magnetic bilayers

In the last decades efforts have been made in developing new material devices based on the electron spin degree of freedom instead of the charge transport, the so called spintronic devices. In this framework magnetic ma-

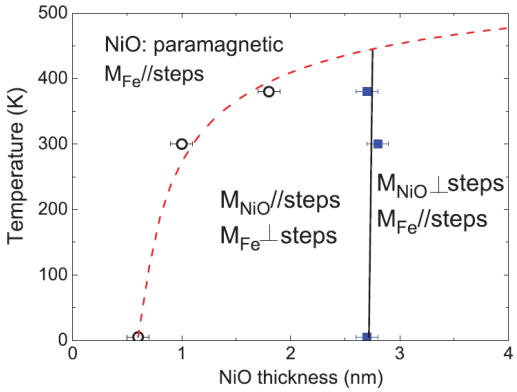

Figure 1.12: Phase diagram of spin orientation for Fe and NiO in Fe/NiO/Ag(1,1,10). Lines are guides to eyes. Image from [54].

terials have found a fruitful ground, particularly shaped as thin films that allow for the miniaturisation of such devices. Many spintronic devices are based on the so called exchange bias effect, that is the breaking of the time reversal symmetry and the rise of an unidirectional anisotropy in a field-cooled[4] ferromagnetic/antiferromagnetic bilayer. Magnetic coupling at the interface allows managing the magnetic properties in heterostructures and the exchange bias effect has attracted a large interest because of its possible applications in magnetoelectronic devices. The mechanism responsible for this phenomenon has not been yet understood in detail from a microscopic viewpoint due to the difficulties in properly detecting the spin configuration of the antiferromagetic phase. Hence a general theory for the exchange bias is still missing, even if some model do exist.

1.3.1 Exchange bias

Once a Ferromagnet (FM) is coupled to an Antiferromagnet (AFM) and such an interface is cooled down below the Néel temperature of the AFM system (assuming the Curie temperature T_c larger than the Néel temperature T_N) an anisotropy termed as "exchange bias" is induced in the FM. This anisotropy was first discovered on Co particles embedded in their native oxide by Meiklejohn and Bean [55] in 1956 and nowadays it represents an intriguing phenomenon characterising FM/AFM bilayers. Magnetic thin films have been the most widely studied type of system because of the high

[4] "Field cooling" is the decrease of the temperature of a material while it is under the effect of a magnetic field pinning the magnetisation of the sample.

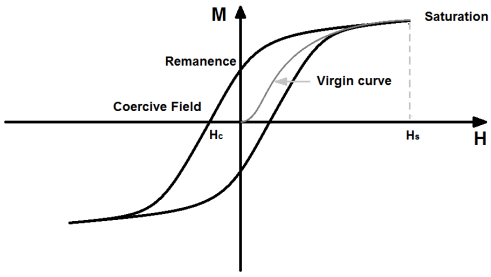

(a) Schematic representation of the magnetisation vs applied field curve for a typical ferromagnet. The main features are labeled.

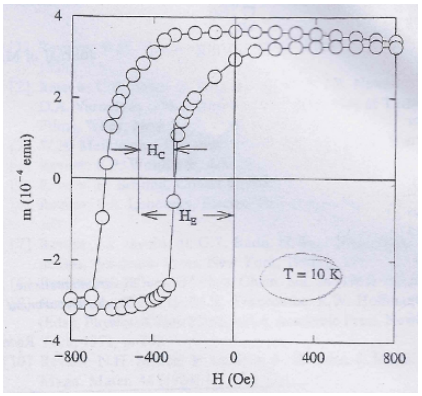

(b) Hysteresis loop of FeF_2 at $T = 10$ K after field cooling. In figure H_E and H_C are the exchange and coercive fields respectively. From [57].

Figure 1.13: Hysteresis loop for a typical FM (schematic in panel (a)) and for a FM/AFM bilayer (panel (b)).

level achieved in controlling and characterising their interfaces and because they found a special role in developing devices based on the exchange bias.

Following the review paper proposed by J. Nogués and I. K. Schuller [56] let us see what this exchange anisotropy is from a phenomenological viewpoint. The coupling at the interface can be highlighted cooling the FM/AFM bilayer from a temperature in between the T_c of the FM layer and T_N of the AFM to a temperature lower than T_N in presence of an external field. In doing so the FM is in its ferromagnetic state and its magnetic ordering is frozen, while the AFM phase make a transition from a paramagnetic phase to the AFM-ordered condition. The effect can be seen in the shift of the hysteresis loop. The hysteresis loop is the characteristic loop in the magnetisation-vs-field graph of a FM. In figure 1.13 the hysteresis loop for a typical FM (schematic in panel (a)) and for a FM/AFM bilayer (panel (b)) is reported. Let us consider a magnetic sample which has never been exposed to a megnetic field. Upon increasing the applied field the magnetisation is increased. In this case the magnetisation grows up to a saturation value along the path termed as "virgin curve". In doing so the randomly organised domain structure is broken and the magnetisation points entirely to the applied field direction. Once the saturation value has been reached, decreasing the applied field the magnetisation decreases but along a different path, so the process is not reversible. The residual magnetisation after removing the applied field is called "magnetic remanence". Such a remanence is due to the

spin interaction discussed in previous paragraphs. In order to demagnetize the sample the "coercive field" must be applied in the opposite direction to the saturation field. The magnetic behavior described here is the same if the field is applied in this second direction, so a loop centered in the origin, called hysteresis loop, is obtained. As clearly shown in figure 1.13 such a loop is no more centered at the origin of the magnetisation vs. applied field axes due to the exchange bias. The shift is usually in the opposite direction with respect to the cooling field, hence the coercive field for decreasing or increasing field is different. This feature disappear approaching the AFM critical temperature, confirming that this anisotropy is related to the presence of the AFM phase. This behavior can be understood in a very intuitive manner [56]. Let us assume an exchange interaction at the interface of a FM/AFM bilayer. As mentioned before if a field is applied in a temperature range $T_N < T < T_c$ the spins of the FM are aligned with the field, while for the AFM they results randomly disposed. This condition is represented in panel (i) of figure 1.14. Cooling down below T_N the spins of the AFM layer assume an AFM order starting with the topmost plane ferromagnetically coupled with the superimposed FM layer as depicted in panel (ii) of figure 1.14. This condition corresponds to the saturation point of the hysteresis loop. Once the applied field is reversed the spins of the FM start to rotate. In the case of sufficiently large AFM anisotropy the spins of the AFM remain pinned instead, as in the case of panel (iii) in figure 1.14. The spins of the AFM locally exert a torque on the spins of the FM trying to keep a ferromagnetic coupling at the interface working against the reversed field. Therefore the field necessary to completely reverse the spins for the FM material will be larger with respect to the one in the case of the single FM layer, because an extra contribution to overcome this microscopic torque is needed (see panel (iv) of figure 1.14). Of course once the applied field is reversed again to its original direction, the torque will favor the spin rotation, because it will act in the same direction of the field, so coming back a smaller field will be necessary to entirely reverse the spins, as shown in panel (v) of figure 1.14. The material behaves as if an extra (internal) bias is present, the *exchange bias*.

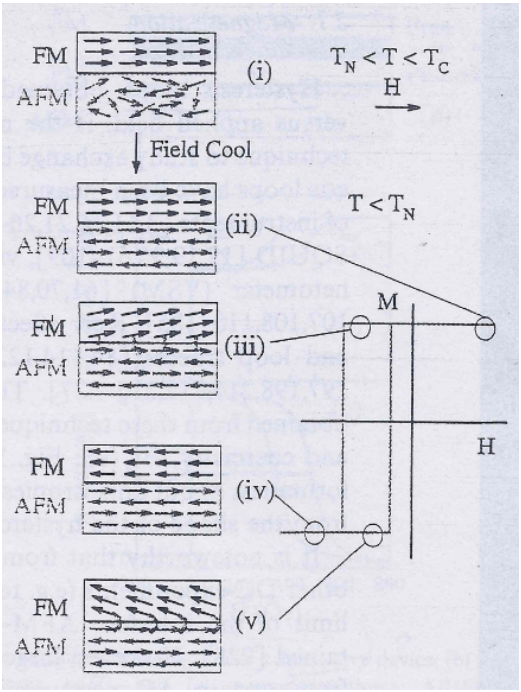

Figure 1.14: Schematic representation of the spin configuration in a FM/AFM bilayer in different stages of the hysteresis loop. Image from [56].

Chapter 2

Electron spectroscopies

In the last decades advances in research have led to the realisation of new materials and devices moving the interest in their characterisation. Capability to control the growth of thin material layers has paved the way for the creation of nanoscale heterostructures whose utilisation in the technological field is nowadays basilar. In this context, the possibility to control magnetic phase transition in heterostructures by coupling layers of different magnetic phase is a requested skill in order to create new devices. Because of the intimate relation existing between the magnetic properties of solids and their electronic structure, electronic spectroscopies found a renewed interest. Particularly those techniques based on core-excitation are now largely diffuse thanks to the advent of Synchrotron light sources. As a matter of fact photoemission spectroscopy has been established as one of the most important methods to investigate electronic structure of matter in all its different states of aggregation as well as Auger electron spectroscopy which is able to highlight phenomena involving interacting valence electrons. The combination of these two fundamental techniques led to the emergence of a new spectroscopy called Auger-PhotoElectron Coincidence Spectroscopy (APECS) that is showing surprisingly useful in surface analysis.

In this chapter the basic concepts of the electron spectroscopies used in this thesis will be discussed.

2.1 Photoemission spectroscopy

Photons and electrons are the easiest *particles* to use for the study of condensed matter and this is the reason why they are used in most of the spectroscopic techniques, both as projectiles or products of scattering processes.

Photoemission spectroscopy is a technique based upon the photoelectric

effect, surely a milestone of the quantum mechanics. In its basics the photoelectric effect consists of the emission of electrons by metal surfaces once lightened with a monochromatic radiation, $\hbar\omega$. Such an emission has been found to depend upon the photon energy while light intensity affect only the number of ejected electrons. These electrons show a well-defined energy spectrum with a maximum value, ${E_k}^{\max}$, related to the photon energy via the Einstein equation [58]

$$ {E_k}^{\max} = \hbar\omega - \Phi \tag{2.1} $$

where Φ is the characteristic work function of the system. Such a simple relation is very powerful indeed because it establishes a close relationship between the energy spectrum and the sample's properties, suggesting to use photoemission spectroscopy in order to get information about electronic structure.

It is possible to extend Einstein equation to those electrons emerging with an energy different from the maximum value. Let E_i be the initial energy of the electron inside the solid, equation (2.1) can be rewritten as

$$ E_k = \hbar\omega - \Phi - E_i. $$

This equation represents the energy conservation of the process in which an electron of the solid is treated as an independent particle. Assuming that the system has a certain energy band, the photoelectron current will depend upon the joint-DOS between initial and final states, reflecting the electronic properties of the solid. It is also clear that changing the photon energy a different portion of the electronic structure can be probed.

So far we have considered, in its very basics, the energetics of the process, but if we are interested in knowing additional notions about information given by such a technique a deeper insight in the states involved is necessary. In order to get the basics of photoemission spectroscopy, the radiation-matter interaction must be discussed.

Following the approach proposed in [59, chapter III, section D] and [60] let us consider the case of a many-electrons atom interacting with the radiation in an independent-particles picture. For this case the Hamiltonian of the system can be expressed as

$$ H = H_0 + H_\gamma $$

where the two terms represent the unperturbed system and the interaction between the electron cloud and the photon. In terms of single-particle contributions, in the non-relativistic limit and under the Born-Oppenheimer approximation, the unperturbed term can be written as

$$ H_0 = \sum_{i=1}^{N} \frac{{p_i}^2}{2m} + \sum_{i=1}^{N} \frac{-Ze^2}{r_i} + \frac{1}{2}\sum_{i\neq j} \frac{e^2}{|\vec{r_i} - \vec{r_j}|} \tag{2.2} $$

where the first sum represents the kinetic energies of the electrons, the other two terms the Coulomb interaction with nucleus and among electrons respectively. Here nuclear terms are neglected. The Hamiltonian for a charged particle in an electromagnetic field can be deduced from the *minimal substitution* [61, appendix 6]:

$$H_{\text{e.m.}} = \frac{1}{2m}\left(\vec{p} - q\vec{A}\right)^2 + q\phi$$

where q, m and $\vec{p}$ are the charge, the mass and the momentum of the particle respectively, while $\vec{A}$ and ϕ are the vector and scalar potentials. In the Coulomb's gauge, where $\vec{\nabla} \cdot \vec{A} = 0$ and the scalar potential $\phi = 0$, the interaction term can be expressed as follow:

$$H_\gamma = \frac{e}{2mc}\sum_{i=1}^{N}\left(\vec{p_i} \cdot \vec{A} + \vec{A} \cdot \vec{p_i}\right) \tag{2.3}$$

where, assuming a weak-field coupling, the $\vec{A}^2$ term is neglected with respect to the linear ones. The electromagnetic wave is assumed to be a plane monochromatic wave[1]

$$\vec{A}(\mathbf{r}, t) = \vec{\varepsilon} A_0 exp\left[i\left(\vec{k} \cdot \vec{r} - 2\pi\nu t\right)\right]$$

where A_0 is an amplitude, $\vec{\varepsilon}$ the polarisation vector while $\vec{k}$ and ν the light wave-vector and oscillation frequency.

Time-dependent perturbation theory states that transition probability from an initial state $|i\rangle$ to a final state $|f\rangle$ is given, at first order, by the Fermi's golden rule

$$P_{i\to f} \propto \frac{2\pi}{\hbar}\left|\langle i|\sum_{j=1}^{N}\vec{A}(\mathbf{r}_j) \cdot \vec{p}_j|f\rangle\right|^2 \delta\left(E_f - E_i - \hbar\omega\right)$$

where the sum runs over all the electrons of the system and the integration of time-dependent parts of states and operator give rise to the energy-conservation delta function.

Assuming that the photon wavelength is much larger with respect to the system dimensions, the dipole approximation can be used, in which $exp\left(i\vec{k} \cdot \vec{r}_j\right) \simeq 1$, expressing the dipole transition matrix-element in terms of an overlap integral between initial and final states. This approximation is

[1]The electromagnetism is linear so every field can be written as a linear combination of plane waves

reasonably good, but for x-rays with $\lambda \approx 10$ Å, as in the case of the radiation emitted from the de-excitation of an aluminum anode (i.e. Al K_α), it starts to be borderline.

The main issue to solve now is how to represent the initial and final states: for example in an atom they have the form of the product of a radial term and spherical harmonics, $\phi_{n,l,m}(r,\theta,\phi) = R_{n,l}(r)\, Y_{l,m}(\theta,\phi)$ while in a molecule often are approximated via a linear combination of atomic orbitals (LCAO) [61]; in solids they are expressed as Bloch-functions [62].

Assuming a strong "one-electron" character for the photoemission process a convenient choice for the initial state results to be the antisymmetrised product of the spin-orbital $\phi_k(\vec{r})\,\chi_k$ of the k-th electron considered as the "active" one, i.e. the orbital from which the photoionisation is assumed to occur and a $(N-1)$-electron residual due to the other "passive" electrons represented by $\Psi_R(N-1)$:

$$\Psi_i(N) = \hat{A}\left[\phi_k(\vec{r})\,\chi_k, \Psi_R(N-1)\right].$$

In this context $\Psi_R(N-1)$ cannot be considered as a proper wavefunction, but as the best representation of the ionic residual. In the weak-field coupling the final state is enough accurately represented by the antisymmetrised product of the spin-orbital of the electron in the continuum and the ionic wavefunction:

$$\Psi_f(N) = \hat{A}\left[\phi_f(\vec{r})\,\chi_f, \Psi_f(N-1)\right].$$

The next step is to consider the emission process rapid with respect to the relaxation time of the residual-electrons. Under this assumption, often termed as "sudden approximation", the matrix element as well as the cross-section are given in terms of product between one-electron dipole matrix element and an overlap integral between ionic wavefunctions in the initial and final states:

$$\frac{d\sigma}{d\omega} \propto |\langle\phi_f(\vec{r})\,|\mathbf{r}|\,\phi_k(\vec{r})\rangle|^2 |\langle\Psi_f(N-1)|\,\Psi_R(N-1)\rangle|^2.$$

The ionic overlap integral is the origin of the so-called monopole selection rule and give rise to transitions characterised by

$$\Delta J = \Delta L = \Delta S = \Delta M_J = \Delta M_L = \Delta M_S = \Delta\pi = 0$$

where, $J = L + S$ is the total angular momentum and π the overall parity.

At this stage it is possible to assume that the residual $N-1$ electrons are not going to relax. This case is termed as "frozen orbital", the natural framework of the Koopmans' theorem, based on the assumption that the one-electron orbitals in the initial state are the same of the final one, in other

words that the hamiltonian describing the system both in the initial and final states is the same. This imply the presence of a single core-hole in the k-th sublevel. Under these conditions the matrix element is reduced only to the dipole electron term, because of the orthonormality of the $\Psi_{R(f)}\,(N-1)$ wavefunctions. The photoemission spectrum expected in this case is composed by a single peak called the Koopmans' or adiabatic peak. Taking into account for a relaxation of the ionic residual the Hamiltonian describing the system in its final state is different with respect to the one describing the system at the beginning. Such a behaviour is due to the fact that after the electron ejection the $(N-1)$ remaining electrons are going to reorganise themselves, changing the electron potential generated. In such a situation the initial ionic residual wavefunction can be projected on more than one final $(N-1)$-electron state, giving access to satellites peak (also termed as shake-up, shake-off or correlation peaks) beside the adiabatic one.

It is not straightforward to apply the same treatment to solids so a different formalism has been developed. For a solid the photocurrent can be expressed as [63]:

$$I \propto \sum_{f,i,\vec{k}} \left| \langle \phi_{f,E_{\mathrm{kin}}} \right| \mathbf{r} \left| \phi_{i,\vec{k}} \rangle \right|^2 A\left(\vec{k}, E\right)$$

where $A\left(\vec{k}, E\right)$ is called *spectral function* and results related to the single-particle Green's function $G\left(\vec{k}, E\right)$ according to

$$A\left(\vec{k}, E\right) = \pi^{-1}\mathrm{Im}\{G\left(\vec{k}, E\right)\}.$$

The meaning of the spectral function is the probability to remove an electron from $(E < E_F)$ or to add one to $(E > E_F)$ an interacting N-electron system. Following the more detailed calculations reported in [63, chapter 1, section 3] it is possible to divide the Green's function into two contribution termed as coherent and incoherent responsible for the main and the satellites peaks.

The element selectivity of photoemission spectroscopy can be used in order to get informations about correlation, highlighting the many-body nature of the photoemission process, but it can also be applied for analytical purpose in order to determine the chemical composition of a sample or keep under control contaminants.

In the following another practical aspects in using photoemission spectroscopy will be discussed.

2.1.1 Specimen thickness estimation using photoemission spectroscopy

All the samples investigated in this thesis have been grown *in situ*, that means, in this case, grown directly inside the experimental chamber of the ALOISA beamline, that is the experimental station used for these measurements and described in more detail in section 3.2.2. For this reason a proper samples' characterisation has been necessary in order to keep under control their structural and magnetic properties. As discussed in section 1.2 in the case of low dimensional systems, like thin films, magnetic properties are strongly influenced by the film thickness. For such a reason it is of great importance to known a technique able to give this structural information and photoemission spectroscopy is a useful tool to get the thickness estimation.

Photoemission in solids, not discussed in details here, could be described with the help of the so called three-step model. Within this framework the photoemission process is decomposed in the following steps:

$1^{\mathbf{st}}$ **step** : an optical excitation occurs within the solid in which an electron of the target atom is promoted from the k-subshell to a Bloch final state still inside the solid, with an energy value that corresponds to the kinetic energy that it will have at the end of the process. This step is usually described via a matrix element, M_{fi}, between these initial and final states, affecting the photoemission cross-section, where labelling as N^{int} the "photocurrent" inside the solid:

$$N^{\text{int}}\left(E, \hbar\omega, \vec{k}_f\right) \propto |M_{fi}|^2 f(E_i)\delta(E_f - E_i - \hbar\omega)$$

in which $f(E_i)$ is the occupancy of the initial state and the delta function ensures the energy conservation;

$2^{\mathbf{nd}}$ **step** : the electron travels inside the solid towards the surface suffering scattering processes which degrade its energy. It is possible to account for this step introducing an optical absorption coefficient, α, besides the inelastic mean free path, λ. The latter describes the average distance that an electron is able to travel without suffering inelastic scattering processes. Ultimately this step can be reduced to a coefficient which depends from both these parameters:

$$d\left[\alpha, \lambda\left(E, \vec{k}\right)\right];$$

$3^{\mathbf{rd}}$ **step** : once reached the surface the electron has to overcome the potential barrier at the surface in order to access the continuum. This last

step is described schematically making use of a transmission coefficient $T\left(E,\vec{k}\right)$.

In the light of this model the photocurrent can be expressed as

$$I \propto |M_{fi}|^2 f(E_i) d\left[\alpha, \lambda\left(E,\vec{k}\right)\right] T\left(E,\vec{k}\right) \delta\left(\vec{k}_{\parallel} + \vec{G}_{\parallel} - \vec{k}_{e\,\parallel}\right) \delta(E_f - E_i - \hbar\omega).$$

Within this model, the photoelectron peak intensity, N_k, produced by the k-subshell can be determined integrating the differential spectral intensity dN_k which in turn can be expressed as the product of all the three steps described. Let us write this intensity highlighting the different contributions. If x, y, z denotes the position within the sample, the differential intensity can be expressed by the following product [59]:

$$\begin{aligned} dN_k \;=\; & \left[\begin{array}{c}\text{X-ray flux}\\ \text{at x,y,z}\end{array}\right] \cdot \left[\begin{array}{c}\text{Number of atoms}\\ \text{in dx,dy,dz}\end{array}\right] \cdot \left[\begin{array}{c}\text{Differential cross-section}\\ \text{for } k\text{-subshell}\end{array}\right] \cdot \\ & \left[\begin{array}{c}\text{Acceptance solid angle of}\\ \text{electron analyser}\end{array}\right] \cdot \left[\begin{array}{c}\text{Probability for no-loss escape}\\ \text{from specimen with negligible}\\ \text{direction change}\end{array}\right] \cdot \\ & \left[\begin{array}{c}\text{Instrumental detection}\\ \text{efficiency}\end{array}\right]. \end{aligned}$$

This differential intensity becomes

$$N_k = I_0 \rho(x,y,z) dx\; dy\; dz \frac{d\sigma_k}{d\Omega} \Omega(E_{\text{kin}}, x, y, z) T(E_{\text{kin}}, k^f, x, y, z) D_0(E_{\text{kin}}) \tag{2.4}$$

where I_0 is the incident photon flux as uniform over all the sample, $\rho(x,y,z)$ the target density, $\frac{d\sigma_k}{d\Omega}$ the atomic differential cross-section of the photoemission process from the k-subshell, $\Omega(E_{\text{kin}}, x, y, z)$ the accepted solid angle of the analyser, which defines also the effective specimen area A_0 involved, D_0 is the detection efficiency while $T(E_{\text{kin}}, k^f, x, y, z)$ represents the probability for no-loss escape with k^f that specifies the direction of the electron motion. This escape probability can be expressed, in its simplest form, via the Lambert-Beer-Bouguer law

$$N = N_0 e^{-\frac{x}{\lambda}} \tag{2.5}$$

which can be used itself as a model in determining the film thickness, simply inverting equation (2.5) to get x and putting inside the ratio of the spectral intensity of a substrate feature once with the clean sample and once with the film grown on top of it. Unfortunately despite its maneuverability, it results too simple for properly modeling the process. Under the aforementioned assumption, neglecting single-crystal anisotropies in emission and

elastic electron scattering and assuming an emission angle θ with respect to the surface, it is possible to integrate equation (2.4) in order to get the photoemission intensity ratio for uniform overlayer grown on top of a "semi-infinite" substrate:

$$\frac{N_l(\theta)}{N_k(\theta)} = \frac{\Omega_0(E_l)A_0(E_l)D_0(E_l)\rho'(d\sigma_l/d\Omega)\Lambda'_e(E_l)}{\Omega_0(E_k)A_0(E_k)D_0(E_k)\rho(d\sigma_k/d\Omega)\Lambda_e(E_k)}[1 - e^{-\frac{t}{\Lambda'_e(E_l)sin\theta}}]e^{\frac{t}{\Lambda'_e(E_k)sin\theta}} \tag{2.6}$$

where the subscripts l and k represent the overlayer and the substrate respectively, $E_{k,(l)}$ the kinetic energy of electrons coming from the substrate (overlayer) subshell, $\Lambda^{(\prime)}(E)$ and $\rho^{(\prime)}$ the inelastic mean free path for electrons with kinetic energy E and the atomic density in the substrate (overlayer) respectively, while all the other parameters have already been presented.

From equation (2.6) it is possible to obtain the thickness t of a film deposited onto a certain substrate via the peak intensity ratio of one core level from the substrate and one from the overlayer, that can be collected in the same spectrum.

2.2 Auger electron spectroscopy

Several decades ago phenomena involving Coulomb interaction among valence electrons in Auger processes have been discovered. Once its electronic cloud is strongly perturbed an atom could eject electrons termed Auger. Such electrons have the peculiarity to show an energy not dependent upon the excitation mode, e.g. X-rays absorption, electron bombardment or nuclear decay, but characteristics of the target atom, a fingerprint. The nature of the Auger electrons has been understood by P. Auger [64] in 1925 establishing a relation between different electron transitions and binding energies that is formalised in the following empirical relationship:

$$E(\alpha\beta\gamma) = E(\alpha) - E(\beta) - E(\gamma) \tag{2.7}$$

where $E(\alpha)$, $E(\beta)$ and $E(\gamma)$ represent the energy of three shells[2] of the atom while $E(\alpha\beta\gamma)$ stands for the energy of a Auger transition in which they are involved. Equation (2.7), which represents a first approximation of the energy balance, suggests to interpret the Auger transition as a two-step

[2]Usually these shells are labelled in spectroscopic notation as K,L,M,... where the capitol letter represent the main quantum number $n = 1, 2, 3, ...$ If the spin-orbit coupling is taken into account a subscript is used to discriminate upon different total angular momentum, for example the L shell will give rise to three contributions labelled as L_1, L_2, L_3 corresponding to the $2s_{1/2}, 2p_{1/2}, 2p_{3/2}$ sublevels respectively.

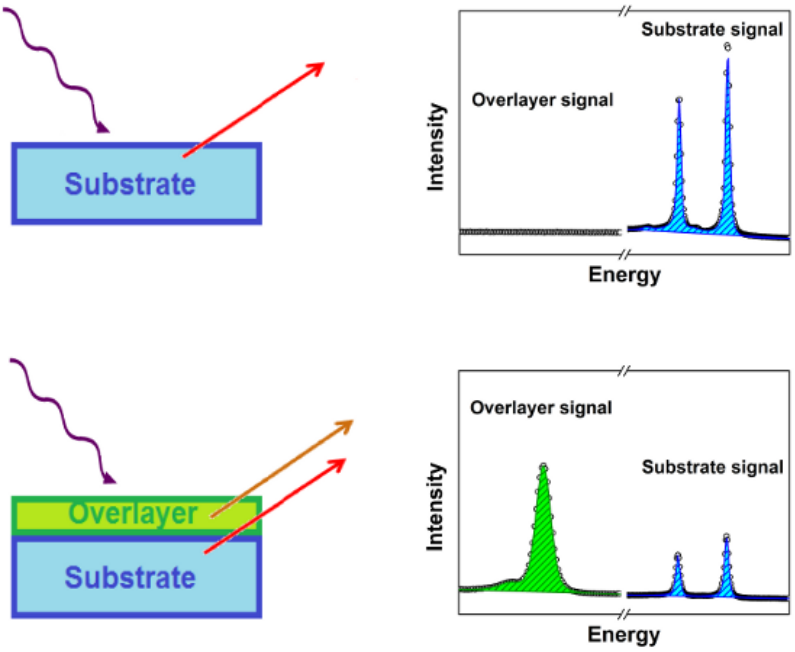

Figure 2.1: Schematic representation of the photoemission process, with related spectrum, from a clean substrate (upper panel) and the case of a uniform and homogeneous film of finite thickness grown on top of it (lower panel): while the model (2.6) needs only to collect the spectrum with the overlayer to get the film thickness, on the contrary using the model (2.5) both the measurements sketched must be performed in order to evaluate the intensity attenuation of the substrate's signal.

process where in the first step an excitation occurs creating an hole in the α subshell, while in the second step a less bound electron from one of the outer β and γ shells comes to fill this hole. In doing so, the excess energy is transferred to a second electron of the other outer shell that, for energy conservation, is emitted to the continuum. In the final state the doubly ionised atom has two holes in β and γ subshells, which can decay again if they are not at the Fermi level yet. This reaction reads

$$\hbar\omega + A \rightarrow A^{+}(\alpha^{-1}) + e^{-} \rightarrow A^{++}(\beta^{-1}\gamma^{-1}) + e^{-} + e^{-} \tag{2.8}$$

assuming a photon absorption as a primary excitation. This reaction is schematically depicted in figure 2.2

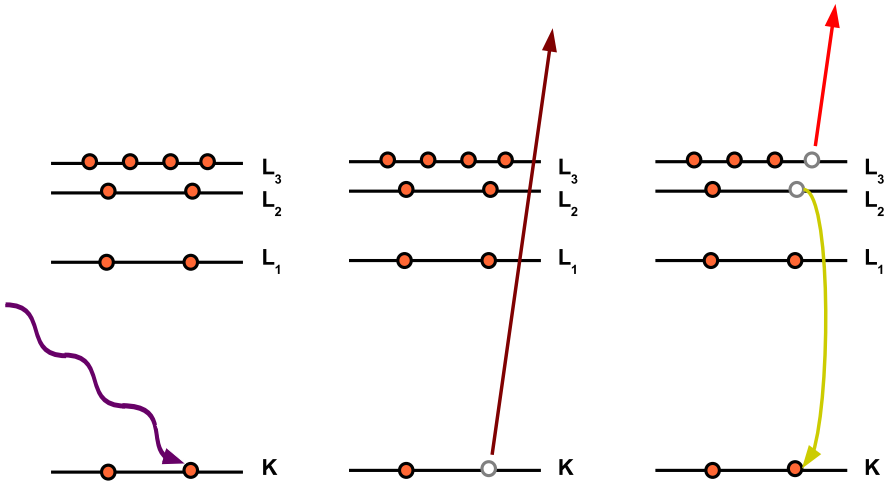

Figure 2.2: Schematic representation of a KL_2L_3 Auger transition following a primary photoexcitation of the $1s$ level. Panels from left to right corresponds to the three states reported in the reaction (2.8).

Because of this interpretation, the notation used in labelling different Auger transition is given in terms of three atomic subshells, expressed in spectroscopic notation, where the first is the subshell of the primary hole production and the other two are the subshells hosting the final state holes, hence for example an Auger transition in which a core-hole in the $1s$ level is filled by a $2p$ electron involving a second electron of the same shell is usually termed as KLL.

The nature of the Auger process could be better defined in terms of quantum-mechanics. The initial state $|i\rangle$ with a hole in the α-subshell, is not a steady state, but a metastable one with an intrinsic width given by both the radiative and Auger decay processes. This discrete state with a core hole is energy-degenerate with respect to the continuum of final states $|f\rangle$ of the doubly ionised atom with two holes in β and γ, so the Auger transition occurs spontaneously. Because of the existence of several final states accessible, the Auger spectrum is rich and difficult to interpret.

Equation (2.7) represents only a first approximation in describing the energetics of the process. This is mainly due to the fact that at the end of the Auger process the target is left in a doubly ionised state with two holes acting as two positive charged particles. It is clear that equation (2.7) neglects the mutual interaction as well as the spin-orbit coupling, whose contribution is relevant and responsible for an energy shift of the predicted transitions.

In order to foresee the energies and probabilities of Auger transitions, let us treat Coulomb interaction in a perturbative manner. The initial state $|i'\rangle$ of the Auger process is the one in which the atom is ionised and hosts a core-hole, α, while the final state, $|f'\rangle$, is made by a doubly ionised atom hosting two valence-holes, β, γ

$$\begin{aligned} |i'\rangle &\rightarrow |i_\alpha\rangle \\ |f'\rangle &\rightarrow |f_{\beta\gamma}\rangle = \phi_p |A^{++}_{\beta\gamma}\rangle \end{aligned}$$

where the final state is composed as the product of a single-particle wavefunction representing the electron in the continuum, and the doubly ionised atom. Spectral intensity, $S(E)$, will be proportional to the transition probability, hence, using the Fermi's golden rule

$$S(E) \propto |M_{i'f'}|^2 \delta(E_{i'} - E_{f'}) \tag{2.9}$$

where the Coulomb matrix element is

$$M_{i'f'} \propto \sum_{m<n} \langle i_\alpha \left| \frac{e^2}{r_{mn}} \right| f_{\beta,\gamma} \rangle.$$

At this point the problem is how to calculate the matrix element. In the same approach proposed for the photoemission process, it is possible to express the initial and final states in terms of single-particle spin-orbitals by using the Slater determinant formalism. Let us consider only the two emitted electrons as "active". Assuming the so called frozen-core approximation, where the spin-orbitals of the "passive" electrons are unrelaxed, the problem is reduced

from many to two electrons.

$$\langle i_\alpha \left| \frac{e^2}{r_{mn}} \right| f_{\beta,\gamma} \rangle \rightarrow \langle i \left| \frac{e^2}{r_{mn}} \right| f \rangle \langle R_i^{++} | A_{\beta,\gamma}^{++} \rangle$$

and in the Wentzel approximation [65] the matrix element is reduced to the difference between the direct, D, and exchange, E, Coulomb interaction term:

$$\begin{aligned} M &= D - E \\ D &= \langle \phi_\alpha(1)\phi_p(2) \left| \frac{e^2}{r_{12}} \right| \phi_\beta(1)\phi_\gamma(2) \rangle \\ E &= \langle \phi_\alpha(1)\phi_p(2) \left| \frac{e^2}{r_{12}} \right| \phi_\beta(2)\phi_\gamma(1) \rangle \end{aligned} \tag{2.10}$$

where the subscript p refers to the free electron in the initial state.

In the form shown above the matrix element highlights that the larger the superposition of the α, β and γ states, the higher the transition probability, hence the fact that the so called Coster-Kronig or Super Coster-Kronig[3] transitions are the highest in intensity.

As briefly discussed in the Introduction of this thesis, the two-step model used in this context is not always proper and its use depends upon the lifetime of the core-hole. In the case of short hole lifetime, that means tens of attoseconds, a single-step approach is necessary with excitation and decay considered as a unique process[4]. Of course the frozen-core approximation could be too stringent because relaxation of residual electrons must be expected.

The mutual interaction of the angular momenta of the two final state holes gives rise to a multiplet splitting. As proposed by Slater in his seminal work [67] an angular momentum l of an electron, or a hole, on which torques do not act can be arbitrary oriented in the space[5]. Choosing any quantisation axis it is possible to project such a momentum along this vector getting a set of values integrally spaced between the parallel and antiparallel orientation with respect to that direction. This means that the projection m_l can equal $l,\ l-1,\ l-2, \cdots,\ -l$. These $(2l+1)$ values correspond to the same number of energy-degenerate stationary states. We need to consider also the electronic spin, an intrinsic angular momentum labelled by s, which is also

[3] A Coster-Kronig Auger transition is the one hosting in the same sublevel the two final state holes, while in a Super Coster-Kronig the initial hole share the same sublevel of the two final holes.

[4] A first experimental proof in [66]

[5] Each electron moves in a field spherically symmetric

arbitrary oriented in the space without reference to the orientation of l. As for the case of the orbital momentum, also for the spin the same projection procedure along the quantisation axis produces $(2s+1)$ states. For an electron $s = 1/2$ so only the two up ($\uparrow$) and down ($\downarrow$) projections are allowed. It is usual to express the values of the total (principal) quantum number n and the orbital l angular momentum (s is always equal to $1/2$) in terms of a literal notation as $1s$, $2s$, ..., $2p$, $3p$, ..., $3d$, $4d$, ..., $4f$ and so on, where the first number is n and $s,\ p,\ d,\ f\ \cdots$ corresponds to $l = 0,\ 1,\ 2,\ 3,\ \cdots$. In this way the electronic configuration of an entire atom can be given in this literal notation. As an example the ground state electron configuration of an oxigen atom results $(1s)^2(2s)^2(2p)^4$ meaning that there are two $1s$ electrons (one with spin up and the other with spin down), two $2s$ electrons and four $2p$ electrons. This is the case of non interacting angular momenta. Let us now move on the case of two electrons (holes) with coupled momenta. In this case the coupling forces introduce a torque which is responsible for a time dependence in the spatial orientation of the orbital and spin momenta. But the torques are internal to the system, so they will not affect the total orbital L and spin S angular momenta. Hence considering the mutual interaction the angular momenta of the electrons are no longer good quantum numbers and the LS-coupling classification is necessary. Thus the l's of all the interacting electrons group together into a integer vector sum L which can be expressed as S, P, D, F, ... terms. The same is for the spins, where the sum vector S can be integer or half-integer. For these sum vectors a spatial quantisation in M_L and M_S projections along a quantisation axis is possible. Identifying M_L and M_S with $\sum m_l$ and $\sum m_s$ for uncoupled electrons multiplets appear from any combination of electrons. Figure 2.3 shows the combination of momenta in the case of p electrons. Let us consider two electrons characterised by $(n, l = 1, s = 1/2)$ and $(n', l = 1, s = 1/2)$. Each of them has $(2s+1)(2l+1) = 6$ different stationary states, which are represented in panel (a) of figure 2.3 (every circle corresponds to a state). Coupling these two electrons, as in panel (b) of the figure, 36 states will rise up, where each point represents $M_L \equiv \sum m_l$ and $M_S \equiv \sum m_s$ of one multiplet and every allowed arrangement gives terms with different energy and multiplicities (reported as the number inside the circle in figure). The number of allowed states is reduced in the case of two "equivalent" electrons, i.e. electrons sharing the same quantum numbers ($n = n'$ in our example). In this case the exclusion principle of Pauli must be considered (panel (c)). In combining momenta, states with $L = 0,\ 1,\ 2,\ 3,\ 4,\ \cdots$ are labelled as $S,\ P,\ D,\ F,\ \cdots$ and the spin multiplicity give rise to Singlets ($S = 0$), Doublets ($S = 1/2$), Triplets ($S = 1$), Quartets ($S = 3/2$), Quintets ($S = 2$) and so on. In panels (d - i) examples for Singlet ($^1S,\ ^1P,\ ^1D$) and Triplet ($^3S,\ ^3P,\ ^3D$) states for

the two coupled p electrons are given. In the case of heavy atoms also the spin-orbit interaction plays a role and the multiplets are classified also by the total $J = L + S$ angular momentum. As an example the triplet P is split in three total angular momentum contributions $^3P_0$, $^3P_1$ and $^3P_2$. The notion of multiplets will be largely used in the following of this dissertation.

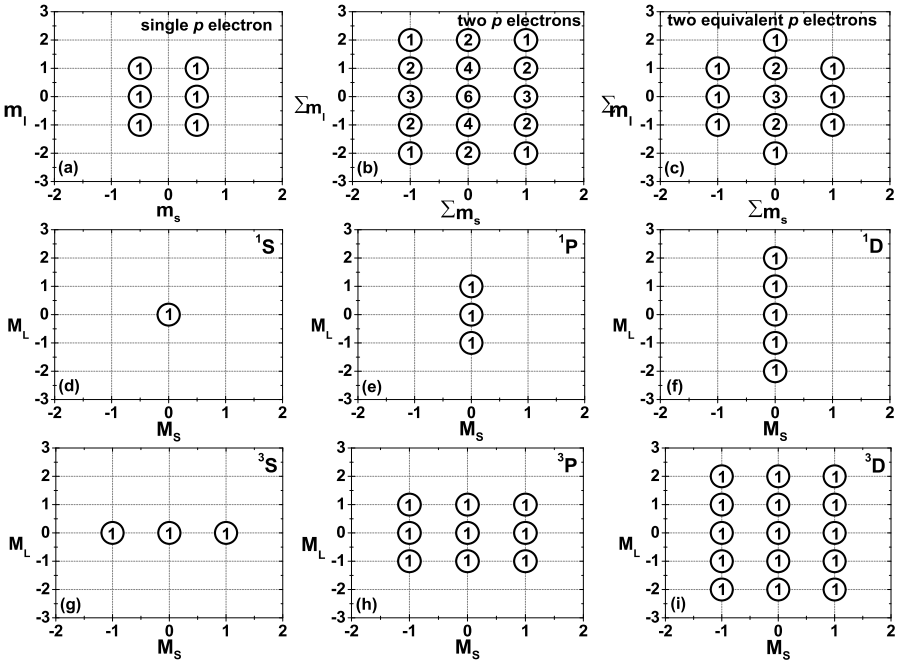

Figure 2.3: Schematic representation of the stationary states for two coupled p electrons. Every circle correspond to a state charactersed by certain values of m_l and m_s or M_L and M_S. The multiplicity of each term is reported inside every circle. In panel (a) the case of a single p electron, in panel (b) two p electrons, in panel (c) two equivalent p electrons. In panels (d-e-f) the case of ^1S, ^1P, ^1D respectively, in panels (g-h-i) the case of ^3S, ^3P, ^3D respectively. Figure redrawn on the basis of [67, figure 1]

Let us now move on to the Auger lineshape from solids. Deep electronic states of a solid still remain atomic-like, while valence levels are strongly perturbed. In the case of an Auger transition in a solid involving valence electrons interesting information about chemical bonds or valence electrons interaction can be achieved. Of high interest are the core-valence-valence (CVV) transitions which produce two valence holes in the solid. An interesting paper is the one published by Powell [68] where the CVV Auger transition from Ag and Al are shown. The main point highlighted in this paper is the different lineshape of the spectra from this two metals as reported

in figure 2.4: in the Ag case a multiplet structure characterised by narrow peaks is evident, while in the Al case the spectral distribution consists of one broad peak, representing its DOS. In order to classify this difference in the lineshape it is usual to term a spectral distribution similar to the Ag one as "atomic-like", on the contrary a spectral distribution made by a single very-broad peak, like in the case of Al, is defined as "band-like". A first interpretation of the aforementioned spectral difference has been given by Lander [71] who proposed that the origin of the Auger lineshape was the self-convolution of the single-particle valence DOS modulated by the energy-dependence of the Coulomb matrix element. Such an approach permits to get an interpretation of the band-like Auger spectra and the case of Al is quite stringent: the Al valence levels consist in a more or less 10 eV width smooth band. Let us label the bottom and the top of the valence band as E_1 and E_2 respectively. In the final state each one of the two holes can be located in any energy point of the valence band, hence the spectral extension of the Auger transition is expected to runs from $2E_1$ (both the holes at the bottom of the band) to $2E_2$ (both the holes on the top of the band). If the DOS is approximated to be constant its self-convolution shows a triangular shape. Putting together the expected band-like spectrum is a single-peak triangular shaped with a width of $W = 2(E_2 - E_1)$. This is the case of the Al, as shown in figure 2.4, with $2(E_2 - E_1) = 2(E_1 + 10\ eV - E_1) = 20$ eV.

To get a quantum-mechanical interpretation of the CVV Auger transition let us introduce a basic model. The two valence holes final state of the considered atom can be represented via the ket $|00\rangle$. Such a state is not an eigenstate of the Hamiltonian because of the delocalised nature of these holes driven by hopping mechanism. It is possible to rewrite this state as a linear combination of a complete set of two-holes steady states $|s\rangle$ with time-independent Schrödinger equation

$$H|s\rangle = E_s|s\rangle.$$

The expansion reads

$$|00\rangle = \sum_s |s\rangle\langle s|00\rangle.$$

Putting this expansion in relation (2.9) immediately rises up the sum over all the projections of the $|00\rangle$ state on the two-holes steady states [72]:

$$S(E) \propto N(E) = \sum_s |\langle s|00\rangle|^2 \delta(E - E_s)$$

where the Fourier's transform of $N(E)$ is the correlation function

$$N(t) = \sum_s |\langle 00|s\rangle|^2 \exp(-iEt) = \langle 00|\exp(-iHt)|00\rangle$$

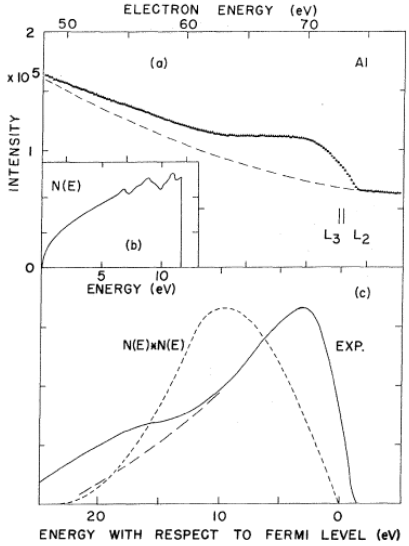

(a) $L_{2,3}VV$ Auger spectrum of Al. In panel (a) the experimental spectrum is given. Vertical bars represent the $L_{2,3}$ binding energies. The assumed background of secondary electron is reported as dashed line. In panel (b) the calculated single-particle DOS from ref. [69] is present. Experimental spectrum in panel (c) given as solid line is obtained after background subtraction. The short-dashed line curve represents the self-convolution of the calculated DOS. The long-dashed line approximates correction for inelastic scattering.

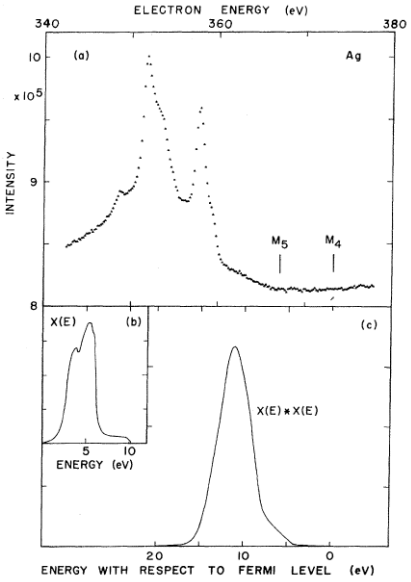

(b) $M_{4,5}VV$ Auger spectrum from Ag. In panel (a) the experimental spectrum is given. Vertical bars represent the $M_{4,5}$ binding energies. In panel (b) the experimental valence band spectrum from ref [70] is shown. Panel (c) contains the self-convolution of the valence band spectrum from panel (b).

Figure 2.4: CVV Auger spectra from Al and Ag. Figures from [68].

describing the time-evolution of the two-holes final state. At this stage the point is to clarify how to express 2-holes-DOS $N(E)$ in terms of known quantity. In an independent-particle picture these two holes are completely uncorrelated so the probability to find them in the same atomic site 0 at a time t is given by the square of the one-particle evolution function $d(t)$. This means that the corresponding 2-DOS $N(E)$ will be

$$N(E) = \int d(E - E')d(E')\, dE'$$

hence given as the self-convolution of local single-particle DOS.

But what happens when these are interacting holes? In order to answer this question let us introduce an interacting term in the Hamiltonian: $H = H_0 + H'$ where H_0 is the non-interacting term, i.e. the part from which the $d(E)$ can be deduced, while H' describes the holes mutual repulsion. Let us now assume that hole-hole repulsion is driven by the short-range contribution of the Coulomb interaction, meaning that the two holes interacts only when belonging to same atomic site, resulting uncorrelated once delocalised throughout the solid. Following the work by M. Cini [72] such an interaction term can be expressed as

$$H' = U n_{0+} n_{0-}$$

with n occupation number operator for the atomic site 0 while $+, -$ represent the spin's projection. In this context U represents a screened Coulomb repulsion due to the polarisation effects of the solid around the two positive charges. Such a choice for the interaction term gives access to an exact determination of the 2-DOS which does not depend upon the unperturbed Hamiltonian part. This exact solution can be expressed in terms of an integral equation [72]:

$$N(t) = N_0(t) - iU \int_0^t dt'\, N_0(t - t'N(t'))$$

where $N_0(t) = d^2(t)$ i.e. the square Fourier transform of the single-particle DOS. Exploiting the relation between the DOS and the Green's function it is possible to express the two interacting particles DOS $N(E)$ in terms of the non-interacting particles ones $N_0(E)$ [31]:

$$N(E) = \frac{N_0(E)}{[1 - UI_0(E)]^2 + \pi^2 U^2 N_0(E)^2} \tag{2.11}$$

where $N_0(E)$ could be given as the self-convolution of the single-particle DOS (from the non interacting particle scheme) and I_0 is the Hilbert transform of $N(E)$

$$I_0 = \mathcal{P} \int dE'\, N_0(E')/(E - E').$$

Let us discuss again the simple case of a constant DOS briefly introduced regarding the Al Auger lineshape. Such a single particle DOS has the form of

$$d(E) = \theta\left(\frac{W}{2} - |E|\right)/W$$

constant between $\pm\frac{W}{2}$ and null elsewhere with W the width of the valence band. The non-interacting 2-DOS is the self-convolution of $d(E)$ i.e.

$$N_0(E) = \left(\frac{1}{W} - \frac{|E|}{W^2}\right)\theta(W - |E|). \tag{2.12}$$

Its Hilbert transform reads:

$$I_0(E) = \frac{1}{W}\ln\left|\frac{E+W}{E-W}\right| + \frac{E}{W^2}\ln\left|\frac{E^2-W^2}{E^2}\right|. \tag{2.13}$$

This example highlights the strong dependence of the Auger lineshape from the ratio $\frac{U}{W}$ once put $I_0(E)$ into equation (2.11): for $U = 0$ the case of non interacting holes is reproduced and the 2-DOS has the form of an isosceles triangle; in the case $\frac{U}{W} << 1$ such a triangular shape suffer a small distortion and the maximum of the spectral intensity is shifted towards higher binding energies, corresponding to lower Auger kinetic energies. The higher the shift of the spectral distribution the narrower the peak. The condition $\frac{U}{W} \simeq 0.72$ represents a critical point: for this and higher values the analytical solution allows for a discrete state that shows itself as a delta-function singularity. This means that from the critical point and increasing the correlation among the two valence holes the Auger spectrum consists of two different contributions, a continuum band-like part and a quasi-atomic peak, as depicted in figure 2.5. The band-like part yields spectral intensity in favour of the quasi-atomic peak upon increasing the correlation. This quasi-atomic peak is also termed as two holes resonance [31].

The results schematically shown in figure 2.5 and briefly discussed above put in evidence that the Auger lineshape is strongly affected by electronic correlations, and in the case of CVV transitions it depends on the competition between the kinetic energies and the repulsion energy of the two valence holes in final state. The approach proposed here in order to predict the CVV Auger lineshape is termed as Cini-Sawatzky theory, from their pioneering works [31, 32] independently developed in 1977.

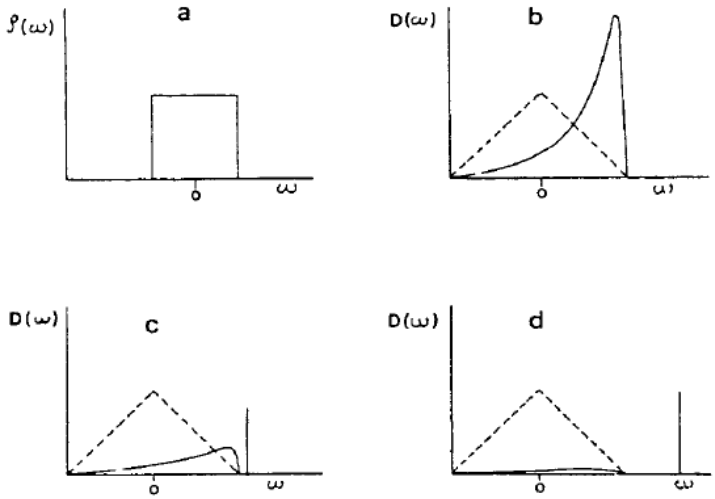

Figure 2.5: Correlation effects on the two-holes DOS, $D(\omega)$, for a system with a constant single-particle DOS, $\rho(\omega)$ in the Cini-Sawatzky model. In panel (a) the model constant single-particle DOS is shown. The corresponding self-convolution (U=0, non-interacting particles) is compared, as dashed line, to the 2-DOS for interacting holes. Panels (b), (c) and (d) shows the 2-DOS for $\frac{U}{W} = 0.5, 0.9$ and 1.5 respectively. As clearly shown by the image, the spectrum consists of a band-like continuum and a split-off bound state represented as a delta-function. Image from ref. [31].

2.3 Auger-PhotoElectron Coincidence Spectroscopy

Photoemission and Auger electron spectroscopies are powerful tools to investigate both chemical composition and electronic structures of surfaces as well as atoms or molecules adsorbed onto a surface. However for systems where electron-electron interactions play a major role a technique not based on an independent-particles approach may be better suited. For example a technique such as Auger-Photoelectron Coincidence Spectroscopy (APECS), where a photoelectron and an associated Auger electron are collected in time coincidence, seems to satisfy this requirement. Such an approach is very powerful indeed because once these electrons are generated by the creation and subsequent annihilation of the same core-hole state, only features coming from that event contribute to the coincidence spectrum. This is schematically shown in figure 2.6 for an inhomogeneous solid composed by atoms of A type and atoms of B type. In a conventional photoemission experiment the spectral distribution is composed by narrow peaks associated to core level-photoemission, a high-kinetic energy broad structure associated to the valence band as well as Auger features, whose interpretation may result too complicated due to the presence of several contributions from both types of atoms. Panel (b) of figure 2.6 shows the capability of APECS to select information coming only from atoms of one type (B in the specific case), resolving different contributions to the Auger spectral intensity in order to obtain information about the local electronic structure of each atom. In the first experiment performed by Haak and Sawatzky in 1978 [27] capability of APECS to resolve different contribution in the Auger lineshape was exploited to unambiguously assign the overlapping main contributions pointing out also the Coster-Kronig-preceded transitions in the $L_{2,3}VV$ transition in Cu. In the same work a large suppression of the multiple inelastic scattering background was also shown.

2.3.1 Basic theory of APECS: one- and two-step description

In an APECS experiment the reaction probed reads

$$\hbar\omega + A \rightarrow A^{++}\left(v^{-1}v^{-1}\right) + e^{-} + e^{-}$$

where the initial state is made of an impinging photon represented by its energy $\hbar\omega$ and an electrically neutral atom target in its ground state, A. In

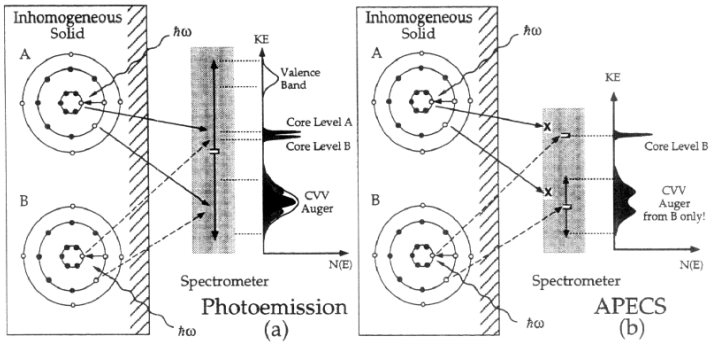

Figure 2.6: Schematic representation of the spectral response in a conventional photoemission experiment (panel (a)) and in an APECS experiment (panel (b)) from an inhomogeneous solid. The inhomogeneity is given by two different types of atom, A and B, which give rise to two different photoemission peaks. APECS is able to isolate contributions from atom A to those from atom B. Image from ref. [73].

the final state a doubly ionised atom $A^{++}\left(v^{-1}v^{-1}\right)$ with two holes in valence levels and the two electrons emitted in the continuum are present. In many-body targets the double ionisation process can also proceed by an indirect channel in which the photon absorption leads to the formation of a core-hole state. Hence the target is left in a singly-ionised state which spontaneously decays, via an auto-ionising process, emitting a second (Auger) electron:

$$\hbar\omega + A \rightarrow A^{+}\left(c^{-1}\right) + e^{-} \rightarrow A^{++}\left(v^{-1}v^{-1}\right) + e^{-} + e^{-}$$

where $A^{+}\left(c^{-1}\right) + e^{-}$ represent the intermediate state where a core-hole is produced in the target and an electron is promoted to the continuum. For this excited state the decay, for our purpose, is driven by an Auger emission. This is the case of APECS. According to the lifetime of the intermediate state this indirect process can be treated in a single- or two-step model: when the lifetime of the intermediate state is long enough to consider it as a well-defined state (fs time scale or larger) the double ionisation process can be considered as a sequential process made by the photoemission and the subsequent Auger emission. In this case the two emitted electrons can be distinguished according to their energy. If the intermediate state has a lifetime shorter than the relaxation time of the core-hole then a single-step model must be used. In this case the two emitted electrons share the excess energy available in the final state becoming completely indistinguishable. Such a distinction was first made theoretically by Gunnarsson and Schönammer [74] and by Ohno and Wendin [75].

The work by Gunnarsson and Schönammer [76, 74, 28], which makes use of the second quantisation formalism, gives the photoemission and Auger emission currents. In this treatment, for the sake of simplicity, the radiative decay channel of the core-hole is neglected. The authors assumed an unperturbed Hamiltonian that does not contain any decay channel for the core-hole and made use of the high-energy approximation for the photoelectron and the Auger one, that means there is no possible decay channel without the presence of an external perturbation. Also the sudden approximation is invoked in order to neglect the mutual interaction between the the emitted electron and the ionic residual. Under these assumptions the photocurrent reads:

$$j_p^{\mathrm{XPS}} = 2\pi f^2 |\tau_{cp}|^2 \sum_i |\langle E_i^{N-1}|\psi_c|E_0\rangle|^2 \delta\left(E_0 + \hbar\omega - E_p - E_i^{N-1}\right) \qquad (2.14)$$

where E_0 and E_i represent respectively the energies for the ground state and for the i-th (N-1)-electron state of the system, ψ_c the annihilation operator for an electron in the $|c\rangle$ state, f the external field amplitude and τ_{cp} the dipole transition matrix element (the subscript c is associated to the core-electron while the subscript p to the photoelectron). In this equation the square modulus matrix element describes the annihilation of a core electron, i.e. the creation of a core-hole, that brings the system from an initial ground state $|E_0\rangle$ to an ionised final state $|E_i^{N-1}\rangle$. The delta function represents the energy conservation of the process. Such a current has been derived assuming no Auger decay channels and it presents the expected form deductible from the Fermi's Golden Rule.
In the case in which an Auger transition plays a role, an optical potential of the form $\Gamma = \sum_{iji'j'} \pi\rho_0 \mathrm{v}_{ijkc}\mathrm{v}_{kci'j'}\psi_i^+\psi_j^+\psi_{j'}\psi_{i'}$ enters in the Hamiltonian. This potential is associated to an Auger transition between an initial state with a core-hole in $|c\rangle$ and a final state with two holes in the i and j sublevels. Here ρ_0 is the density of final states. The index k represents the free electron momentum, while ψ_i^+ the creation operator for an electron in the i-level and $\psi_{i'}$ the annihilation operator for an electron in the i' sublevel. Coulomb matrix elements are indicated via v_{kcij}. If the optical potential is a simple complex number, as in the case of Auger electrons emerging from closed shells, it affects the core-hole lifetime as a simple Lorentzian broadening [76], in other cases, for example if the valence band is involved, this potential acts as a two-particles operator (see ref. [74] for more details).

In the same works the authors derived the Auger current in a one-step model approach which can be expressed as follows:

$$j_k^{\mathrm{A}} = \rho_0(E_k) \sum_n \left| \sum_m \frac{\langle E_n^{N-2}|A_k\psi_c^+|E_m^{N-1}\rangle\langle E_m^{N-1}|\psi_c|E_0^N\rangle}{E_0 + \hbar\omega - E_m^{N-1} - E_p + i\Gamma} \right|^2$$

where the Auger operator containing the Coulomb matrix elements has the form:

$$A_k = \sum_{ijc} \mathrm{v}_{kcij} \psi_i \psi_j .$$

In this equation the argument of the square modulus describes the annihilation of an electron in $|c\rangle$, i.e. the creation of the core-hole, than the creation of an electron in $|c\rangle$, i.e. the annihilation of the core-hole, that is driven by the Auger transition that via the A_k operator annihilates two electrons in the i-th and j-th sublevels, leaving the systems with two final state holes. Now it is possible to determine the pair-emission probability for a photoelectron with energy E_p and an Auger electron with energy E_k applying energy conservation:

$$\begin{aligned} P(E_p, E_k) \quad \propto \quad & \rho_0(E_k) \sum_m \left| \sum_n \frac{\langle E_m^{N-2} | A_k \Psi_c^+ | E_n^{N-1} \rangle \langle E_n^{N-1} | \Psi_c | E_0^N \rangle}{E_0^N + \hbar\omega - E_p - E_n^{N-1} + i\Gamma} \right|^2 \\ & \times \delta(E_0^N + \hbar\omega - E_p - E_k - E_m^{N-2}). \end{aligned} \tag{2.15}$$

The main point to highlight in this one-step description is given by the summation over the complete set of $(N-1)$-electrons states: this implies that the Auger dacay can take place from all the possible $(N-1)$-electrons intermediate states, giving origin to satellite lines on the high kinetic energy side of the main line called "shake-down" satellites. Also the energy conservation plays a crucial role clearly showing that the two emitted electrons can share continuously their total energy, $E_{tot} = E_p + E_k = \text{const}$. The resonant nature of APECS with respect to the direct DPE process mentioned in the Introduction of this thesis can be found looking at equation (2.15): the pair-emission probability for a photoelectron and an Auger electron is maximum when the denominator vanishes, which corresponds to a photoelectron emitted with an energy correspondent to the one expected in a conventional photoemission process (see also equation (2.14)).

In the two-step description of the process the Auger decay is assumed to be independent from the initial core-hole creation, taking place from a stationary state. This is the case in which the core-hole lifetime results longer than the time required by the residual system to relax. Once the core-hole has been created the potential is suddenly changed and this could leave the system in an excited state. Such an excitation can propagate away bringing the system, after a long-enough time, in a sort of local "new ground state". Hence it is assumed that the valence electrons are involved in an Auger transition that takes place in this state which origins from the potential with a core-hole present, $\left|E_0^{N-1}\right\rangle$. This has the effect on equation (2.15) to remove the sum over all the accessible intermediate states with $(N-1)$-electrons,

hence equation (2.15) can be rewritten as:

$$P(E_p, E_k) \propto \rho(E_k) \sum_m \left| \langle E_m^{N-2} | A_k \Psi_c^+ | E_0^{N-1} \rangle \langle E_0^{N-1} | \Psi_c | E_0^N \rangle \right|^2 \times \delta(E_0^N + \hbar\omega - E_p - E_0^{N-1}) \delta(E_0^{N-1} - E_k - E_m^{N-2}).$$

As mentioned before in the two-step model the *primary excitation* and the *secondary Auger emission* are considered independent from each other and the pair-emission probability describes these sequential steps via the two factors in the square modulus: the photoemission process brings an initially neutral charged atom to this $\left| E_0^{N-1} \right\rangle$ state from which the Auger transition takes place. It is quite evident that approaching the process in a two-step model the energy conservation must be taken into account separately for the the photo- and Auger electrons, allowing for their energy discrimination.

2.3.2 AR-APECS

Auger-Photoelectron Coincidence Spectroscopy has shown that the collection of Auger electrons once the parent core ionic state has been defined increases the energy discrimination with respect to the conventional photoemission and Auger spectroscopies. An APECS experiment detects, in time correlation and energy selection, a photoelectron and an Auger electron generated in the creation-decay process of a unique core-hole state in a specific atomic site. Combining the photo- and Auger electron spectroscopies, APECS combines atomic site selectivity with valence band sensitivity, allowing an insight to electron correlation. Coster-Kronig transitions are the best natural candidate to be investigated for this purpose, but not even APECS is capable in distinguishing individual multiplet terms components arising from the two final holes coupling.

APECS results from Ge(100) [35] and Cu(111) [29] have shown the capability of coincidence spectroscopy in disentangling multiplet terms, even if their separation is less than their lifetime broadening, simply by changing the detection angle of the electron-pair. This further discrimination in Angle Resolved-APECS (AR-APECS) experiments gives the possibility of selecting different m- projections of the angular momentum for both the photo- and Auger electron. Hence performing an Angle Resolved coincidence experiment increases the amount of information in the same spirit of Angle Resolved Ultraviolet Photoemission Spectroscopy (ARUPS) allows to map the energy bands of a systems while the conventional UPS gives only informations about the valence band density of states.

An AR-APECS experiment probes the multiple differential Auger current, dI_{Au}, angular ($d\Omega_{\mathrm{Au}}$ and $d\Omega_{\mathrm{ph}}$) and energy (dE_{Au}) resolved as [77]:

$$\frac{dI_{\mathrm{Au}}}{d\Omega_{\mathrm{Au}} d\Omega_{\mathrm{ph}} dE_{\mathrm{Au}}} \simeq \Gamma(E_{\mathrm{Au}}, E^0_{\mathrm{Au}})|T_{\beta\alpha}|^2$$

where the first factor represents the Auger lineshape, while the argument of the square modulus is the Auger decay amplitude. Such a differential cross-section puts in evidence the possibility to perform experiments in different modes. Two possible modes are listed as an example:

- *Energy mode*: by fixing the detection angle and scanning upon the Auger energy working with a fixed photoelectron energy, hence collecting a specific Auger transition;
- *Angular mode*: by fixing the two electrons' energies and the photoelectron detection angle and by scanning the Auger ejection angle, measuring a specific Auger Electron Diffraction (AED).

In the following we will refer only to the *Energy mode*. On the basis of [77] let us interpret an APECS event in the two-step model approach: in the first step a core-hole is created via a core ionisation process and in the second step this core-hole will decay driven by an Auger process as if it were happening independently but in the same isolated atom. In the decay process the energy, the angular momenta and magnetic quantum numbers describing the wavefunctions of the ejected electrons are well defined.

Spherical tensor theory [78] allows to describe the angular distribution of the ejected electron-pair at the atomic site of the primary ionisation. The initial state symmetry is responsible for the ejection anisotropy and to put it in evidence let us rewrite the process reaction underlining the total angular momenta of the different terms:

$$\hbar\omega(j_\gamma)+A(J_0) \rightarrow A^+(\alpha_1 J_1, \alpha'_1 J'_1)+e^-(j_1) \rightarrow A^{++}(\alpha_2 J_2, \alpha'_2 J'_2)+e^-(j_1)+e^-(j_2)$$

where j_γ, J_0 are the angular momenta of the impinging photon and the target atom respectively, $\alpha_i J_i$ the angular momentum of the (single or double) ionised atom, while j_1, j_2 the angular momenta of the ejected electrons. Under the dipole approximation and in the reference frame with light polarisation vector along the z-axis, the angular distribution of Auger electrons can be described as [77]:

$$\begin{aligned}\rho_{k_1,q_1}(\alpha_1 J_1, \alpha'_1 J'_1) &= \sum_{k_e q_e k_r q_r} \frac{1}{2J_0+1}\sqrt{\frac{4\pi}{2k_e+1}} Y_{k_e q_e}(\theta_e, \phi_e) \\ &\quad \times (k_1 q_1, k_e q_e | k_r q_r) \rho_{k_\gamma q_\gamma} \mathcal{I}_{k_e k_1 k_r} \qquad (2.16)\end{aligned}$$

where $\rho_{k_\gamma q_\gamma}$ are the statistical tensors [79] related to the photon, $Y_{k_e q_e}(\theta_e, \phi_e)$ the spherical harmonics of the photoelectron and $(k_1 q_1, k_e q_e | k_r q_r)$ the Clebsch-Gordan coefficients. $\mathcal{I}_{k_e k_1 k_r}$ contains the dynamical parameters and the dipole matrix elements:

$$\begin{aligned}\mathcal{I}_{k_e k_1 k_r} &= \frac{1}{4\pi}\hat{k}_1\hat{k}_e \sum_{l_1 l_1' j_1 j_1' J_r J_r'} (-1)^{J_r+J_0+k_r+j_1'-\frac{1}{2}} \hat{J}_r\hat{J}_r'\hat{l}_1\hat{l}_1'\hat{j}_1\hat{j}_1'(l_1 0 l_1' 0|k_e 0) \\ &\times \left\{ \begin{array}{ccc} j_1 & l_1 & \frac{1}{2} \\ l_1' & j_1' & k_e \end{array} \right\} \left\{ \begin{array}{ccc} 1 & J_r & J_0 \\ J_r' & 1 & k_r \end{array} \right\} \left\{ \begin{array}{ccc} J_1 & j_1 & J_r \\ J_1' & j_1' & J_r' \\ k_1 & k_e & k_r \end{array} \right\} \\ &\times D_{J_1 j_1 J_r J_0} D^*_{J_1' j_1' J_r' J_0}.\end{aligned}$$

In this last equation the notation $D_{J_1 j_1 J_r J_0}$ used for the dipole matrix elements implies that the angular momentum J_1 is coupled to j_1, the photoelectron momentum, via a resonant state characterised by an angular momentum J_r, which in turn is determined by coupling J_0 and j_γ. It is now possible to get the angular correlation function between the two emitted electrons combining these statistical tensors in equation (2.16) with the tensors [80] describing the spin-unresolved detection efficiency [77]:

$$W = \sum_{k_1 q_1 J_1 J_1'} \frac{\hat{J}_1^{-1}}{4\pi} \rho_{k_1,q_1}(\alpha_1 J_1, \alpha_1' J_1') R_{k_1}(J_1 J_1'; J_2) \sqrt{\frac{4\pi}{2k_1+1}} Y_{k_1 q_1}(\theta_2, \phi_2) \tag{2.17}$$

where the spherical harmonics of the Auger electron and the Auger parameter $R_{k_1}(J_1 J_1'; J_2)$ are present. Particularly the Auger parameter is linked to the Auger matrix elements $V_{J_2 j_2 J_1}$ as in the following:

$$\begin{aligned}R_{k_1}(J_1 J_1'; J_2) &= \sum_{l_2 l_2' j_2 j_2'} (-1)^{J_1+J_2+K_1-\frac{1}{2}} \hat{l}_2\hat{l}_2'\hat{j}_2\hat{j}_2'\hat{J}_1(l_2 0 l_2' 0|k_1 0) \\ &\times \left\{ \begin{array}{ccc} J_1 & j_2 & J_2 \\ j_2' & J_1' & k_1 \end{array} \right\} \left\{ \begin{array}{ccc} l_2 & j_2 & \frac{1}{2} \\ j_2' & l_2' & k_1 \end{array} \right\} \\ &\times V_{J_2 j_2 J_1} V^*_{J_2 j_2' J_1'}.\end{aligned}$$

The relation (2.17) highlights a fundamental aspect of AR-APECS which is that different angular components contribute in different way to the total intensity collected at a given angle, particularly each component contributes with a weight mainly due to the sum upon the Clebsh-Gordan coefficients, which in turn are dependent from the magnetic quantum number m_l. This means that selecting the ejection angle electrons from a specific magnetic sublevel are collected. This statement will be discussed in more detail in the remainder of the paragraph.

Let us discuss the case of $M_3M_{45}M_{45}$ Auger transitions, the same transitions investigated in this thesis. In the following we will consider the entire double emission process as realised in two steps in which the emission from the atomic site, for both the photo- and Auger electrons, is then affected by crystal diffraction. The atomic wavefunctions appearing in equations (2.16) and (2.17) act as source waves for the subsequent interaction with the crystal. This means that the diffraction pattern of both the photo- and the Auger electrons must be considered as they are generated after the diffraction process. The interaction is assumed to be elastic, hence a description in which the diffraction process will affect only the flux of probability for the electron-pair to reach the analysers results appropriate. For high kinetic-energy ($E_k > 300$ eV) electrons the diffraction is mainly dominated by the forward scattering, while at low energy large-angle scattering play a role. Simulations of the diffraction pattern have shown that the angular distribution of emitted electrons is affected by both the orbital and magnetic quantum numbers l and m_l [81]. While the orbital momentum dependence arises from a repulsive barrier accompanying Coulomb interaction in describing the overall potential, the magnetic sublevel dependence is associated to a non statistical distribution of the initial sublevels, as in the case of a magnetic sample or by using a well defined polarised probe. Atomic scattering influences pattern anisotropy but leaves almost unaffected the memory on the quantum numbers due to the source wave [29, and ref. therein] and large-angle scattering spreads different magnetic sublevels in an efficient way [82].

In an AR-APECS experiment, properly choosing the collection angle, a specific partial-wave for the emitted photoelectron can be selected. The source wave anisotropy introduced by the core-hole polarisation is accounted for by the introduction of a quantisation axis coincident with the incoming light polarisation vector $\vec{\varepsilon}$. In the case of linear polarisation the core-hole ion polarisation is along this axis. Selection rules for the photoionisation and the subsequent Auger decay act as guide in order to interpret the energy distribution of electron-pairs. The optical dipole selection rules [61, p. 429] govern the photoionisation process. This means that the only partial-waves allowed are reduced to those with an orbital angular momentum that differs for a unity with respect to the core-hole's one, $\Delta l = \pm 1$, with the additional restriction $\Delta m = 0$ in the case of linearly polarised light. This last constraint plays an important role in interpreting the angular distribution of emitted electron-pairs because it states that the photoemitted electron has the identical momentum projection m of the core-hole left behind. In turn the core-hole quantum numbers enter into the selection rules for the Auger

decay according to what reported in [34]:

$$\begin{aligned} l_c + l_1 + k &= \text{even integer} \\ l_A + l_2 + k &= \text{even integer} \\ \beta = m_1 - m_c &= m_A - m_2 \\ |l_c - k| \leq l_1 &\leq l_c + k \\ |l_A - k| \leq l_2 &\leq l_A + k \end{aligned} \tag{2.18}$$

In equations (2.18) l_c, l_A, l_1 ed l_2 are the orbital quantum numbers of the core-hole, the emitted Auger electron and the two final-state holes respectively. In the same way m refers to the corresponding magnetic quantum number. The k and $\beta = \{-k, -k+1, ..., 0, ...k-1, k\}$ coefficients are the orbital and magnetic quantum numbers of the expansion in spherical harmonics $Y_{k\beta}(\theta, \phi)$ of the Coulomb interaction [34]

$$\frac{1}{|\vec{r}_1 - \vec{r}_2|} = 4\pi \sum_{k=0}^{\infty} \frac{1}{2k+1} \frac{r_<^k}{r_>^{k+1}} Y^*_{k\beta}(\theta_1, \phi_1) Y_{k\beta}(\theta_2, \phi_2)$$

where $r_{>(<)}$ represents the greater (lesser) between $\vec{r}_1$ and $\vec{r}_2$.

Now it results possible to characterise the source wave. In the $M_3M_{45}M_{45}$ transition a $3p$ level is ionised hence $l_c = 1$ and because of the dipole selection rules the emitted photoelectron has either an s-character ($l_p = 0$) or a d-character ($l_p = 2$). This means that only final states with $m_c \equiv m_p = 0, \pm 1$ can be accessed[6] (the subscript p stands for photoelectron). The final state of the transition is the one with two d-holes so $l_1 = l_2 = 2$. For such a transition the Auger electron is expected to be emitted mainly with an f-character ($l_A = 3$) [81, 83] hence only the projections $m_A = 0, \pm 1, \pm 2, \pm 3$ are allowed. In the simple atomic case, i.e. neglecting the diffraction process, only spherical harmonics with $m = 0$ can contribute with spectral intensity along the quantization axis (defined by the light polarisation), while the spherical harmonic $Y_{31}(\theta, \phi)$, allowed for the Auger electron, reaches a maximum 40° far from the light polarisation vector. This just to highlight that collecting electrons at different ejection angles it is possible to enhance or suppress the contribution of specific sublevels. Gotter et al. [29] performed a simulation of the diffraction pattern based on the Multiple-Scattering Calculation of Diffraction (MSCD) code properly adapted to get the decomposition in individual m partial-waves (see ref. [29] for more details). Their result, reported here in figure 2.7, shows clearly that different magnetic sublevels contribute to the total intensity with different relative weight at different scattering angles. Because in an AR-APECS experiment the electron analysers are set at

[6] $m_c \equiv m_p$ because of the linear polarisation of the light. This implies that the $m_p = \pm 2$ states cannot be accessed.

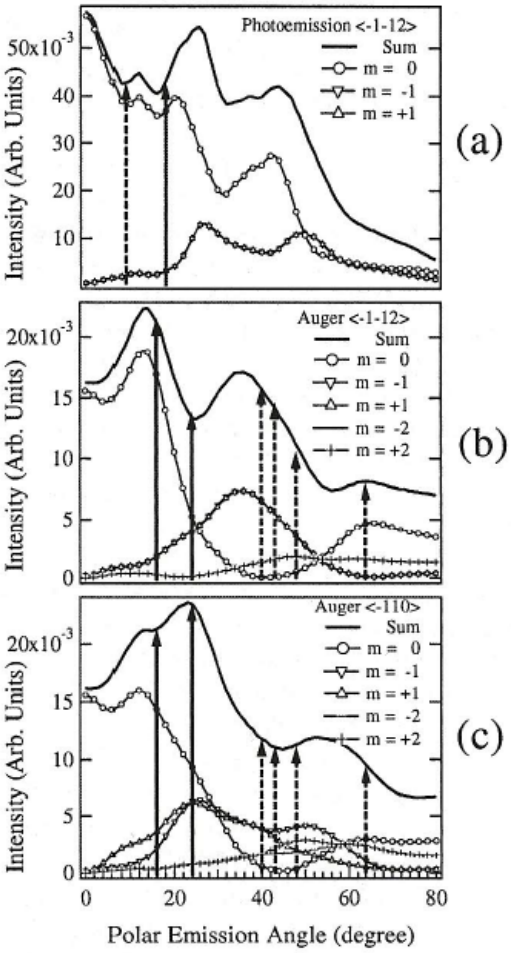

Figure 2.7: m resolved electron-diffraction simulation with MSCD code. In panel (a) the photoelectron polar distribution is shown at an azimuthal angle corresponding to the $< \bar{1}\bar{1}2 >$ direction. In panels (b) and (c) two Auger-electron distributions along the $< \bar{1}\bar{1}2 >$ and $< \bar{1}10 >$ directions are shown respectively. Total intensity (thick solid line) and the different partial waves for $m = 0$ (open circles and line), $m = -1$ (open down triangles and line), $m = 1$ (open up triangle and line), $m = -2$ (minus symbols and line) and $m = 2$ (plus symbols and line) are plotted as a function of the polar emission angle. Image from ref. [29].

specific detection angles, they will preferentially collect electrons with specific quantum numbers instead than others. This aspect is of pivotal importance because selecting specific orbital and magnetic quantum numbers of the two emitted electrons results in selecting the two final state holes spin configuration which in turn determines the multiplet structure of the Auger spectrum. In other words it is possible to access the final state multiplet spin configuration of the system by properly choosing the detection conditions and without any spin detection.

To explain these aspects let us consider the contribution to the total spectral intensity due to the first term of the expansion of the Coulomb interaction, i.e. the case $\beta = 0$. According to the selection rules (2.18) $m_c = m_1$ and $m_A = m_2$, so the magnetic quantum numbers of the two final state holes are identical to those of the photoelectron and Auger electron respectively. This implies that the difference in magnetic quantum numbers of the final state holes is equal to the difference in quantum numbers of the ejected electrons, $\Delta m = (m_1 - m_2) = (m_c - m_A)$. It results useful to better understand how the multiplet-selectivity in AR-APECS is achieved recalling that for the $M_3M_{45}M_{45}$ transition one of the final state hole can show an s- or p-character while the other an f-one. For an electron-pair the spectroscopic notation in LS-coupling results appropriate as put in evidence in [30] and for these two holes the ^3F triplet and the two ^1G,^1D singlets have to be expected to contribute to the total intensity because in a simple closed-shell model the Auger final state can be written as a linear combination of states given by the product of one-electron states with different m value:

$$|L, M\rangle = \sum_{\substack{l_1 + l_2 = L \\ m_1 + m_2 = M}} C^{LM}_{l_1 m_1 l_2 m_2} |l_1 m_1\rangle |l_2 m_2\rangle \tag{2.19}$$

where L is the total angular momentum and M its projection for the final state holes, $C^{LM}_{l_1 m_1 l_2 m_2}$ the Clebsch-Gordan coefficients and $|l_i m_i\rangle$ the one-particle final hole state. Exploiting equation (2.19) it is possible to calculate the relative contribution of the singlet and triplet states as a function of the difference in magnetic quantum numbers for the emitted electrons, Δm. In figure 2.8 the result of this simple calculation is shown as reported in ref. [36]. It is clear from figure 2.8 that the ^3F triplet is weighted towards large $|\Delta m|$ showing no intensity for the case $|\Delta m| = 0$, on the contrary the singlet ^1G is the only contribution in the case of two final state holes characterised by the same magnetic quantum numbers. This is simply a consequence of the Pauli's exclusion principle.

Let us see how the AR-APECS multiplet-selectivity is achieved upon a simple change in the kinematic condition, i.e. the detection angle. As clearly

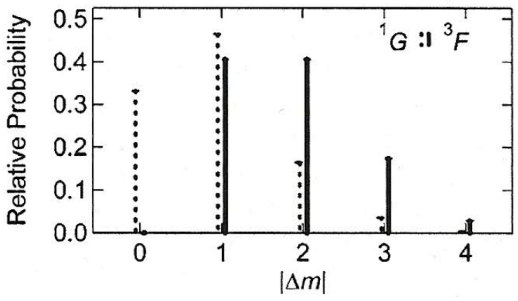

Figure 2.8: Relative contribution of the ^1G and ^3F multiplet terms, predicted according to equation (2.19), as a function of the difference in magnetic quantum numbers Δm of the two final state holes. Image from ref. [36].

shown in figure 2.7 collecting both the photo- and Auger electrons along the light polarisation vector direction will results in two final state holes characterised by $m_1 = m_2 = 0$. In such a case the kinematic configuration is usually labelled as AA geometry where "A" stands for detection direction "aligned" with the electric vector of the light. In this notation the first index is referred to the photoelectron while the latter to the Auger one. Because these two holes belong to the same shell, the d-shell in the case of the $M_3M_{45}M_{45}$ transitions, they have the same spatial quantum numbers, so the two-holes wavefunction has a full symmetric spatial part. The overall wavefunction must be antisymmetric so in this kinematic condition only spin-antisymmetric (singlet) contributions can be accessed. Of the same tendency is the geometry in which both the emitted electrons are collected at an angle larger than 20°. This geometry is usually labelled as NN where "N" stands for "not aligned" with the polarisation vector. As shown in figure 2.7 the greater the detection angle the higher the angular momentum projection m accessible. Also in this condition the dominant configuration is the ^1G [36], but the singlet-selectivity is not so stringent as in the case of the AA geometry. On the contrary collecting one of the two electrons not aligned and the other aligned with the light polarisation vector, $\vec{\varepsilon}$, in a NA geometry, leads to final states in which the dominant contributions arise from $|\Delta m| \geq 1$, so the ^1G singlet contribution results suppressed and a sizeable amount of ^3F triplet appear. Let us consider an hypothetical coincidence apparatus made by five in-plane analysers: what has been just reported above is schematically sketched in figure 2.9 where in the upper panel the AA geometry (an electron collected within 20° far from the polarisation vector can be considered aligned, see figure 2.7) is reported, while in the lower panel the photoelectron is collected in a not aligned direction with respect to $\vec{\varepsilon}$ realising the NA

geometry. According to what has been just reported different kinematics are

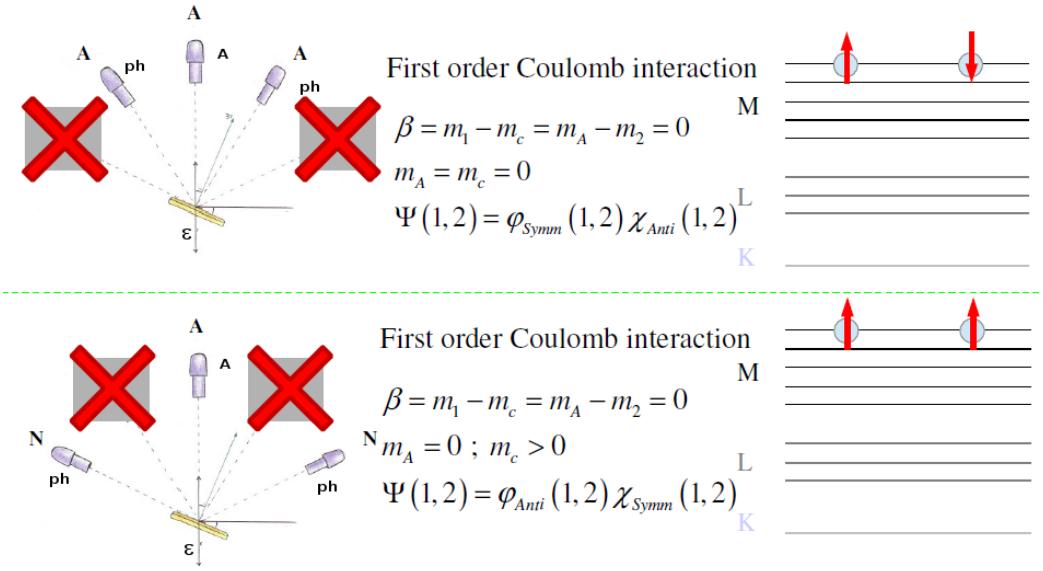

Figure 2.9: Multiplet-selectivity in AR-APECS: the case of two spin $\frac{1}{2}$ holes.
Upper panel: both the photoelectron and the Auger electron are collected within an angle of 20° reproducing the AA kinematic condition. The central analyser is dedicated to the Auger electron collection, while the other two more external analysers are devoted to the photoelectron detection. The most external analysers are neglected in this case. Such a couple of electron-pairs contributes with the singlet to the total intensity.
Lower panel: the Auger electron, collected with the central analyser, aligned with the light polarisation, is coupled with photoelectrons detected at an angle larger than 20°, in the NA geometry. Such a kinematic condition gives access to spin-symmetric (triplet) contributions.

expected to give different partial Auger yield spectra, enhancing or suppressing multiplet spin terms. Hence upon a simple comparison of the lineshape of the spectral distribution collected in different geometries it is possible to get the multiplet-selectivity, having access to the final state hole multiplet spin configuration.

2.3.3 DEAR-APECS

The selectivity of the spectra collected upon changing the kinematic conditions can be characterised by a dichroic effect in AR-APECS called DEAR-

APECS, defined as the asymmetry in these spectra [36]:

$$\text{DEAR-APECS}(E) = \frac{\text{AN}(E) - \text{AA}(E)}{\frac{1}{2}\sum_i \text{AN}(E_i) + \text{AA}(E_i)}$$

or in an equivalent manner instead of the AA configuration the NN one can be put in. It has been shown on a $(\sqrt{3} \times \sqrt{3})$R30°-Sn/Ge(111) sample [36] that the Sn $M_5N_{45}N_{45}$ transition is characterised by a singlet component with a negative asymmetry, while the triplet shows it positive. In this case the Sn MNN transition involves all closed-shell levels, so no intrinsic preferred orientation is present. In an open-shell system, on the contrary the finite magnetic moment anisotropy due to the different population of the m sublevel can be revealed. This is the case for materials with ferromagnetic or antiferromagnetic ordering.

Chapter 3

Experimental set-up

In this thesis the coincidence spectroscopy described in the previous chapter will be used to investigate magnetic properties of thin films. In the following an introduction to a typical experimental apparatus for electron coincidence spectroscopy will be given. In the specific, the set-up used for the experiments proposed in this thesis will be described.

Auger-Photoelectron Coincidence Spectroscopy is a two particles technique in which two emitted electrons, the photoemitted and the Auger ones, selected according to their kinetic energies and momenta (ejection angle), have to be simultaneously collected.

In the initial state a photon, impinges on a neutral target A. This absorption process leads to a singly ionised state where a core hole is created and a photoelectron is emitted in the continuum. That core hole undergoes a decay process leading to a final state in which the target is doubly ionised and two electrons are emitted to the continuum.

The specificity of APECS resides in the fact that is a technique able to disentangle electron-pairs in the final state coming from independent event, e.g. two different photon absorption, with respect to those pairs made by correlated electrons, i.e. coming from the creation-annihilation of the same core hole, or in other words emitted from the same, and then unique, photon absorption process. To satisfy this condition is of fundamental importance to realise an acquisition chain able to measure the time-coincidence of detected electrons.

In order to understand this fundamental aspect of coincidence spectroscopy, let us see in its schematic a prototypical coincidence experimental apparatus, as reported in figure 3.1, which consists of:

- an ultra high vacuum (UHV) chamber;
- a primary source (X-ray or UV lamp as well as Synchrotron radiation);

- a couple of independents electron analysers (at least);
- a dedicated coincidence acquisition chain.

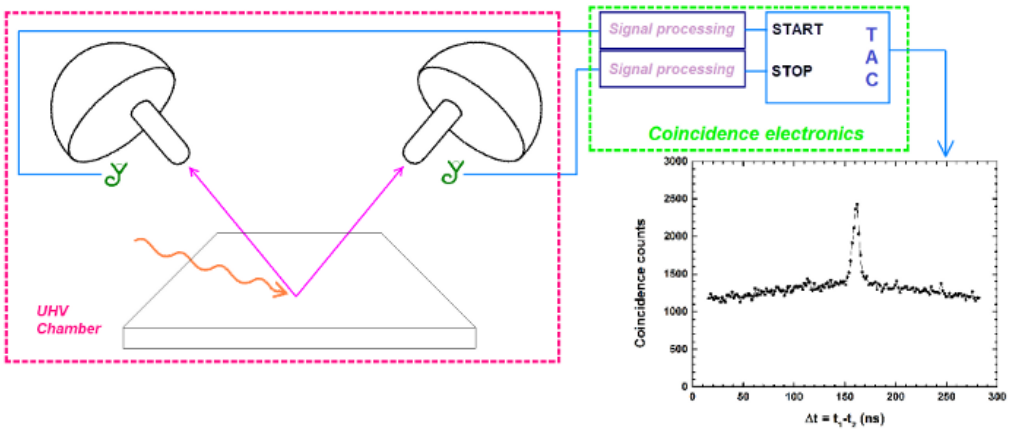

Figure 3.1: Schematic view of a coincidence set-up.

After the photon absorption the two emitted electrons are selected according to their energy and momentum via a couple of independent electron-analysers and arrive to the detectors. A coincidence electronics analyses the signals produced by the detectors: if the delay in the arrival time of the two electrons on the detectors is within a certain allowed time window (usually few hundreds of nanoseconds) the electron-pair is detected, on the contrary the two electrons remain undetected. The coincidence acquisition chain makes possible to record the time delay in the arrival time of the electrons to the detector, $\Delta t = t_1 - t_2$, realising the so called "time spectrum" of the experiment. This time spectrum is simply an histogram reporting the occurrence of the arrival time delay Δt of those electron-pairs properly selected in energy and momentum.

The electron-pairs time distribution contains information to distinguish true coincidence events among all the electron-pair emitted from the sample. The totality of electron-pairs recorded is composed by true coincidence events, those pairs made by two electrons coming from the same radiation-matter interaction event, and accidental events, any other event in which two uncorrelated electrons came from two different photon absorption processes occurred within time resolution.
It is possible to disentangle true coincidence events with respect to accidental ones because of their characteristic time distribution: while accidental coincidence events are distributed in a continuous background over the whole

time window allowed, true coincidences, because the two electrons coming from the same physical event have to reach the detectors simultaneously, that means within the time resolution of the experiment, are expected to follow a peaked distribution centred at specific arrival time delay. By removing the accidental coincidence background the number of correlated electron-pairs is obtained. Reporting the true coincidence counts acquired at fixed photoelectron energy as a function of the kinetic energy (ejection angle) of the Auger electrons, it is possible to obtain the so called APECS (AR-APECS) spectrum.

The experiments proposed in this thesis have been performed at the ALOISA beamline of the Elettra Synchrotron Radiation Facility of Trieste, Italy, and in the remainder of this chapter a detailed description of this experimental apparatus will be given.

3.1 Light source

The light source used to perform the experiments presented in this thesis is the Synchrotron radiation generated at the Italian Synchrotron radiation facility ELETTRA. A Synchrotron is a peculiar light source consisting of a circular evacuated pipe in which electrons are forced to move circularly under the action of several magnets placed along the path with the aim to bend trajectories or focus the electron beam. Once the expected relativistic energy has been reached by means of linear accelerator and circular boosters, the electrons are in a quasi-stationary condition: travelling in the storage ring they lose energy every time they are compelled to turn, emitting the so called Synchrotron radiation [84, chapter 1] [85] and regaining energy in passing through radio frequency cavity placed along the vacuum pipe. If high field magnetic structures, like undulators, dedicated to the production of high quality light are placed in the straight sections of the storage ring we are talking about *third generation synchrotron radiation facility.* ELETTRA is one of them.

3.1.1 Synchrotron Radiation

It is well established that when a particle is accelerated it emits light. In the case of non-relativistic particles the total power radiated scales with the square of the acceleration following the so called Larmor formula. On the contrary, when electric or magnetic fields act on a charged particle forcing it to move with relativistic speed, the radiated light instead of being a dipole-type, spatially distributed as a $sin^2\theta$, where θ is the angle between

the acceleration vector and the observer, it collapse in a narrow cone along the direction of the motion under the effect of a Lorentz transformation. In figure 3.2 a qualitative representation of the emission pattern is given.

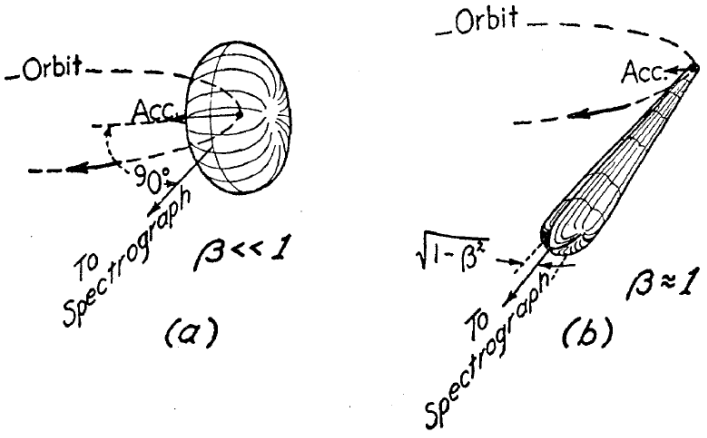

Figure 3.2: Qualitative radiation pattern due to charged particles moving along a circular path: left panel (a) for non-relativistic particles ($\beta = v/c << 1$) shows a typical dipole pattern that is boosted in a narrow cone in case of relativistic particles as in the right panel (b). From ref. [86].

Synchrotron radiation emitted by electrons is an extremely intense and collimated light and it spans on a broad energy range from the infrared up to hard X-rays. These are only some of the interesting properties of such a high brilliance light source because it is characterised also by a high degree of polarisation, a pulsed time structure due to the bunches in which electrons are packaged in the storage ring, a high degree of coherence and a high beam stability.

3.1.2 The insertion device

For the ALOISA beamline the light is produced using an undulator, a so called *insertion device*, (ID). An ID is a periodic magnetic structure, made by the repetition of magnets properly shaped and oriented with a spatial period λ_u, installed in a straight section of the storage ring. When an electron passes through these devices is subjected to a periodically high magnetic field, normally applied with respect to the orbit plane and changing direction upon two adjacent periods, that force it to wiggle following a sinusoidal path on the horizontal plane around its former trajectory, as reported in figure 3.3.

This means that the entire structure, with an L length, is made by N periods, $L = N\lambda_u$. In this way electrons emit light at every turn.

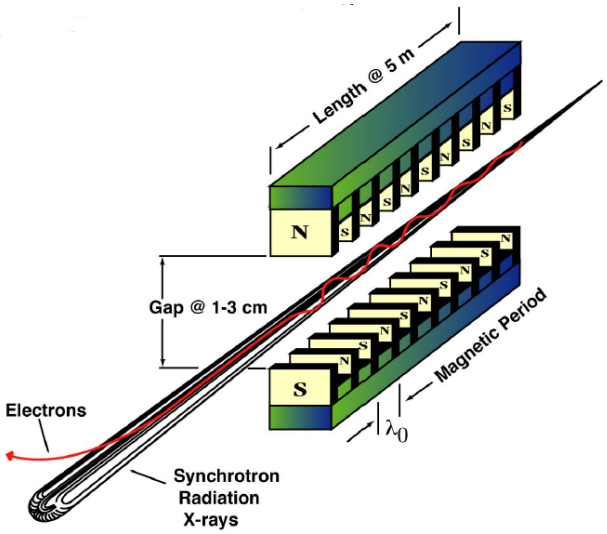

Figure 3.3: Schematic view of an undulator. S and N mark the different magnetic poles, λ_0 is the magnetic period. In figure an example for the values of the total length of the structure and the gap between the upper and lower multipole arrays are given. In red the sinusoidal trajectory of the electron beam in the plane of the orbit. A sketch of the emitted light is also present. Figure from the web [87].

In a classical picture an oscillating charge emits light with a spectral peak centered at the charge oscillation frequency ν, and a quantum mechanical approach doesn't radically change the picture, so for an electron wiggling inside an undulator an emission of light with a spectral response centered at a specific frequency is expected.
An electron moving at the speed of light sees the array of magnets of the undulator as a periodic magnetic field coupled with a periodic electric field of the same frequency, so it looks as an electromagnetic wave with frequency

$$\nu = c\gamma/\lambda_u \tag{3.1}$$

where the wavelength is given by the period of the array divided by the γ factor due to Lorentz contraction [88]. Under the interaction with this electromagnetic wave, the electron moving into the ID emits a radiation with a frequency that in the laboratory frame is not given by equation (3.1), but Doppler shifted:

$$\nu \approx 2\gamma^2 c/\lambda_u \tag{3.2}$$

The γ^2 factor reflects the contribution of two different relativistic effects, the Lorentz contraction and the Doppler shift. In order to characterise the emission of an insertion device it is useful to introduce the dimensionless parameter K given by the ratio between the natural emission cone aperture, $1/\gamma$, and the wiggling angle in a quarter of period made by the electron beam inside the device, α. Such a coefficient is related to the magnetic field inside the device and the period length via the following formula [85]:

$$K = \frac{e}{2\pi mc}\lambda_u B = 0.934\lambda_u[\text{cm}]B[\text{T}]$$

For an undulator $K \ll 1$ that means α smaller than the aperture of the emitted radiation cone. This implies that interference occurs between the radiation pulses coming from the same electron in different points of the trajectory and a coherent superposition of the pulses must be taken into account, leading to an emission intensity growing with the square of the number of periods, N^2.

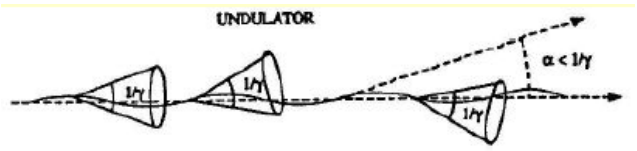

Figure 3.4: Schematic sketch of emitted light from an undulator. The wiggling angle α that quantifies the spread among emission cones is less than the semi-aperture of the emitted light cone. Figure from [85].

As reported in [85], considering the phase shift existing between photons emitted from the same electron at different point along the path in the periodical array of magnets, the observed radiation at a given angle θ with respect to the undulator axis is

$$\lambda = \frac{\lambda_u}{2\gamma^2}\left(1 + \frac{K^2}{2} + \gamma^2\theta^2\right).$$

Because the magnetic field intensity can be expanded in Fourier series of fundamental wavelength λ, it is possible to obtain also higher harmonics

$$\lambda_n = \lambda/n$$

and on the axis of the undulator ($\theta = 0$) only odd ones are emitted.
Such an emission appears to be narrow in frequency. The bandwidth for each

harmonic approximately is:

$$\frac{\Delta\lambda}{\lambda} = \frac{1}{nN} \tag{3.3}$$

where N is the number of periods in the undulator and n the harmonic order. Anyway it is important to keep in mind that the pulse duration is not the key factor for the bandwidth, determined instead by the diffraction-grating-like behaviour of the magnet array, as clarified by equation (3.3), where the number N of periods assumes the role of the groove density of a grating. This last point highlights the necessity to tune the emitted band from the undulator and the subsequent step of monochromatisation along the optical path toward the experimental chamber. The harmonic selection can be done changing the gap between the two arrays of magnets composing the insertion device. The gap value affects the magnetic field inside the poles indeed, moving the central emission wavelength.

In table 3.1 the principal parameters of the undulator of the ALOISA beamline are given.

Besides the wide spectral distribution, another fundamental characteristic of the light produced by an undulator is its high polarisation degree:

in the orbital plane the light is completely linearly polarised, while above and below this plane, a phase shift between the two electric field components is responsible for an elliptical right and left polarisation.

3.2 The ALOISA beamline

Advanced Line for Overlayer, Interface and Surface Analysis (ALOISA) is a multipurpose beamline in use at the ELETTRA synchrotron radiation facility dedicated to the study of surfaces. This beamline permits to exploit the capability of several analytical techniques such as Surface X-Ray Diffraction, Photoemission Spectroscopy, X-Ray Absorption, Photoelectron Diffraction, Angle-Resolved XPS, Angle-Resolved Coincidence Spectroscopy and Electron Diffraction in Reflection, combining structural investigation with electron spectroscopies, in order to probe different characteristics of a sample.

3.2.1 Light transport

The light for the ALOISA beamline is produced by an undulator and transported to the experimental chamber across several optical elements schematically depicted in figure 3.5. In order to keep divided the optical hutch (all the vacuum pipe and the optics dedicated to the light transportation) and the storage ring a shutter and a stopper are interposed. Once these two

Table 3.1: Parameters of ELETTRA and the ID 7.2 undulator from [89, 90].

Nominal electron energy	2.0 GeV (75% users time) 2.4 GeV (25% users time)
Ring current	300 mA at 2.0 GeV 140 mA at 2.4 GeV
Machine operation mode	top-up
Injection in top-up	1 mA every 6 minutes at 2.0 GeV 1 mA every 20 minutes at 2.4 GeV
Machine Critical Energy†	3.2 keV at 2.0 GeV 5.5 keV at 2.4 GeV
ID source point horiz/vert	241/15 (μm) at 2.0 GeV 283/16 (μm) at 2.4 GeV
ID Number of periods	19
ID Period length λ_0	80.36 mm
ID Total length L	1.527 m
ID Minimum gap	21 mm
ID Critical Energy (gap = 26 mm)	2.0 keV

† $E_c = \frac{hc}{\lambda_c} = \frac{3hc\gamma^3}{2R}$.
$\lambda_c = (4/3)\,\pi r \gamma^{-3}$ is a parameter of the storage ring called critical wavelength which corresponds to the wavelength that splits the total emitted power spectrum into two equal parts and gives information about the spectral emission range of the facility. Typically the spectral distribution is non zero up to few times this value. Equations from [85].

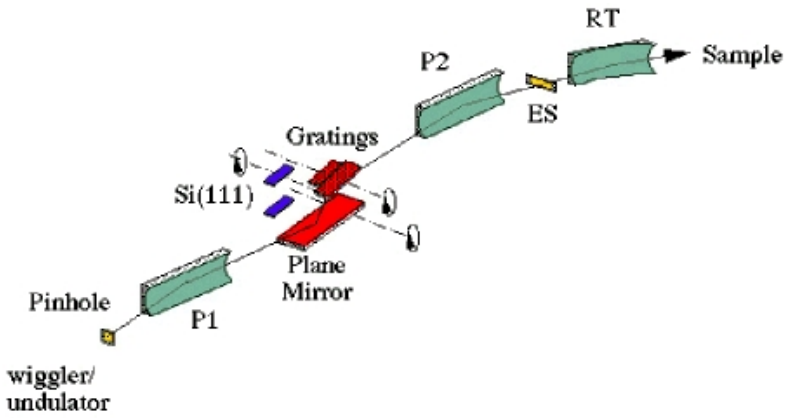

Figure 3.5: In figure the main optical components of the ALOISA beamline are sketched. Besides the monochromator three focusing mirrors ($P1$, $P2$ and RT), a pinhole and an exit slit (ES) are presented. Figure from [90].

blocking elements are opened the light produced in the undulator can pass through the optical hutch.

Subsequently the radiation is selected in angle passing through a pinhole. As mentioned in section 3.1.2, this affects the linear polarisation degree of the light, which is, in this case, linear. A first paraboloidal mirror, $P1$ in figure 3.5, collects the light to collimate and focus it onto the dispersive element in sagittal configuration.

The monochromator is a peculiarity of this beamline. The dispersive element is composed by two different monochromators covering the spectral range from 120 eV up to 8000 eV. The light beam impinges onto the energy dispersive device that can be, depending upon the spectral interval required, a plane mirror coupled with a plane grating for the (120 - 2000) eV or a Si(111) double-crystal for the rest of the spectral range (2000 - 8000) eV. The mirror-grating system, mainly used for spectroscopic purpose, guarantees an energy resolution at energy E given by $E/3000$ that can reach the value $E/5000$ optimizing the optics of the beamline. The energy selection is based on light interference leading to a diffraction pattern. The angular intensity profile of the emitted light will result in a series of fringes due to the interference between the light scattered by different grooves whose envelope is its diffraction pattern. Let θ be the angle between the incident and the emitted light, D the distance between two subsequent grooves and n the diffraction order. The condition to have a maximum of interference is

$$sin\theta = \pm n\frac{\lambda}{D} \tag{3.4}$$

where λ is the wavelength of the emitted light. The peak width decreases proportionally to $\frac{1}{N}$ with N number of grooves. From these considerations it is easy to understand that different energies are emitted at different angles in narrow cones.

The second dispersion device is a double Si crystal cut along the (111) surface. This element is employed in structural measurements, covering the spectral range from 2000 eV up to 8000 eV. In this case the energy selection is obtained exploiting the Bragg scattering process. In this case atomic sites of a crystal act as coherent sources for the scattered light, playing the role of the slits of an optical grating. As in the previous case energy selection is obtained through the interference process. Equation (3.4) is still valid substituting D with twice the atomic planes distance $2d$. In this case the energy resolution, that is affected by crystal reflectivity, is of the order of $E/7000$. In both cases the beam is subjected to two reflections in order to have the out-coming beam parallel with respect to the incoming one, hence the (linear) polarisation plane of the light is preserved.

Once monochromatized, the beam is focused via a second paraboloidal mirror, $P2$ in figure 3.5, onto the exit slits, ES in the figure, which act performing the energy selection, hence reducing the bandwidth. Beyond ES there is another mirror, RT in figure, which focuses the beam at the center of the experimental chamber. This toroidal mirror is equipped with an electrical contact onto its gold coating used to determine the photon flux via the drained current: the current in this circuit is proportional to the photon absorption, that in turn is proportional to the incident flux. A photon flux of 5 x 10^{10} photons/s is available working at higher energies, instead it reach $> 10^{11}$ photons/s working at lower energy. Due to the *top-up* mode of working at the storage ring, in which every few minutes[1] a new electrons' injection is performed, this flux is highly stable. The typical spot size at the center of the experimental chamber is 30 x 200 μm. In order to keep the experimental chamber separated from the transportation optics, a valve between the toroidal mirror and the chamber is interposed.

3.2.2 The end station

The ALOISA UHV chamber is composed by two different parts separated via a gate, as shown in figure 3.7. These two chambers are kept at a pressure of 10^{-10} hPa via several vacuum pumps.

The so called preparation chamber is devoted to sample preparation, hence is equipped with an Ar gas-line and an ion-gun in order to sputter the

[1] See table 3.1

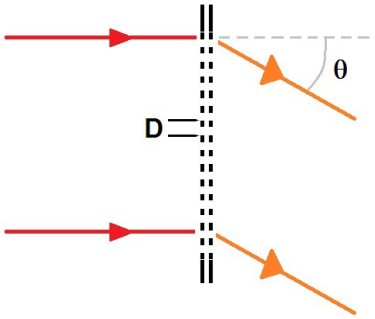

(a) Schematic representation of a diffraction grating. D is the grating periodicity, θ the angle at which outcoming light is collected. For a given energy of the incoming light, maxima of emission are given by equation (3.4).

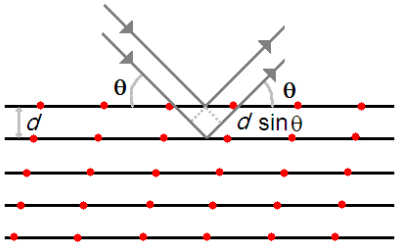

(b) Schematic representation of a crystal: every dot represents a lattice site while solid line are guide for eyes to underline atomic planes. d is the lattice constant, and θ the angle between the light momentum and the crystal plane.

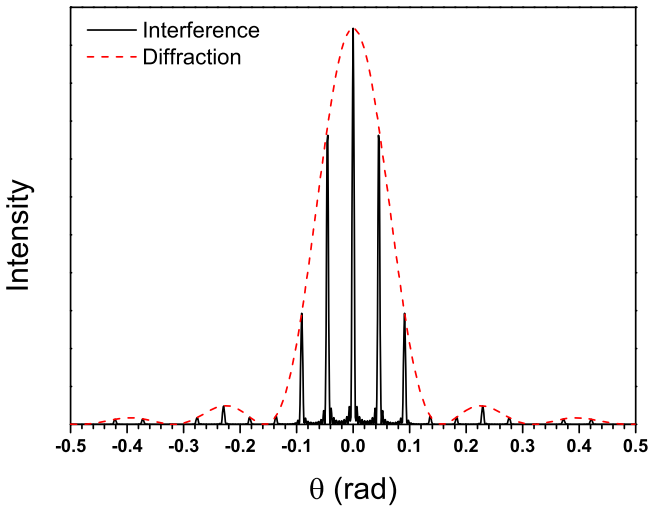

(c) In figure the intensity of emitted light from a diffraction grating is reported as a function of the emerging angle θ for a fixed wavelength. Fringes due to interference and the envelope diffraction pattern are also marked.

Figure 3.6: Light scattering geometry for a diffraction grating and for a crystal.

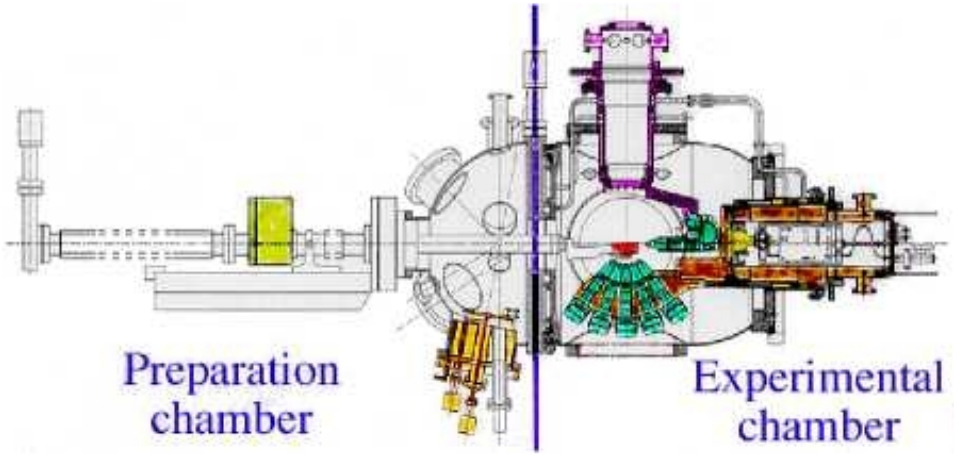

Figure 3.7: The section of the ALOISA UHV chamber is shown. Roughly: the preparation chamber, on the left, is equipped with a RHEED apparatus, an ion-gun and some evaporation-cells (yellow in the bottom side of the pre-chamber), while the experimental chamber hosts six electron analysers in two different frames (green in the figure). Figure from [90].

sample surface. A Reflection High Energy Electron Diffraction (RHEED) set-up is used to keep under control the crystallographyc quality of the surface and to properly align high-symmetry direction of the crystal with respect to the radiation beam. In order to grow different films onto a substrate surface a Molecular Beam Epitaxy (MBE) cryopanel with four slots for knudsen cells and electron-bombardment evaporators besides two quartz-microbalances is present. Other gas-lines, e.g. an O_2 one, are mounted and used to prepare samples in different atmospheres.

The experimental chamber is equipped with six different electron analysers hosted in two independent and movable frames called *axial frame* and *bimodal frame*. On the axial frame five among these six analysers, 18° apart, are placed; on the bimodal frame instead a single multichannel analyser, one channeltron for Partial Electron Yield measurements in XAS and photodiodes (two in total current mode and one in energy resolved mode) are present. In order to fulfill the stringent and partly conflicting requirements imposed by the several experimental techniques available at the ALOISA beamline, this peculiar array of electron analysers had to be specifically designed and realised [91]. Every single analyser can be individually powered and tuned in energy in order to satisfy the energy selection requirements of energy-resolved experiments like in coincidence measurements performed to investigate the pair-electron emission from the same physical event but with

different kinetic energies. The hardest task in designing such a spectrometer has been the capability to fulfill the angular resolution requirements in angle-resolved coincidence and non-coincidence measurements as well as the necessity to work with a manageable coincidence count rate obtainable enlarging the angular acceptance of the analysers at the expanses of time and momentum resolution. To overcome such a bottleneck these analysers with an individual narrow angular acceptance are mounted in an array fashion in order to increase the total angular acceptance for coincidence measurements without any time and momentum degradation [91].

The two frames and the whole experimental chamber can be moved independently: experimental chamber can rotate around the Synchrotron radiation (SR) beam axis, for the axial frame is the same, instead the bimodal frame is free to rotate around the synchrotron axis. The movement extension and the corresponding resolution are give in table 3.2. The sample holder has six degrees of freedom, three translational and three rotational. One of the three translations is along the beam axis ($\hat{x}$) and the other two are mutually perpendicular and both orthogonal to the beam axis ($\hat{y}$ and $\hat{z}$). One of the three rotations, $R1$, is around the SR beam axis, a second one, $R2$, around the sample surface normal and the third one, $R3$, orthogonal with respect to the previous two, allows to change the grazing angle of the incident beam. In table 3.2 the rotation limits are given. A sample's temperature in the range $150 - 1100$ K is achievable.

The combination of the rotation available in this beamline allows to cover near the entire 2π solid angle over the surface with the bimodal analyser. Additionally combining the chamber rotation with one of the manipulators rotation it is possible to perform two identical measurements with a different light polarisation orientation with respect to the surface.

3.3 Electrons detection

In most of the experiments the energy-selection is a required capability of the detection system. Electrostatic lenses as well as the dispersive elements are included into the electrons detection apparatus. All these elements are made by several electrodes properly polarised in order to collect, transport, focus and energy-select electrons emitted by a sample. As will be discussed in the following the hemispherical analyser acts as a band-pass filter, while the transport optics can act as a frequency-shifter. In this section a brief description of the basic concepts of these elements is given.

Table 3.2: Rotational degrees of freedom for the experimental chamber of the ALOISA beamline as reported in [90].

Rotating element	Rotation axis	Extension	Resolution
Experimental chamber	SR*beam	$\pm 120°$	$0.00015°$
Axial frame	SR beam	$\pm 120°$	$0.0002°$
Bimodal frame$^+$	Perpendicular SR beam	$\pm 100°$	$0.0002°$
Sample holder $R1$	SR beam	$\pm 185°$	$0.005°$
Sample holder $R2$	Surface normal	$\pm 95°$	$0.004°$
Sample holder $R3$	Grazing angle	$-2°; +10°$	$0.004°$

* SR = Synchrotron Radiation.

$^+$ solidal with the chamber

3.3.1 Electrostatic lenses

Electrostatic lenses, sketched in figure 3.8a, are usually axially symmetric electrodes that, once biased, produce equipotential surfaces similar, in shape, to the physical surfaces of optical lenses as shown in figure 3.8b. A charged particle, passing through these surfaces can be accelerated or retarded, focused or defocused, depending upon the polarisation of the electrodes. Considering the particle velocity as the electrostatic equivalent of the optical refractive index the parallel with respect to optical lenses is quite straightforward. Electrostatic lenses are placed as previous stage with respect to the energy-selection and their role is double, on one hand they focus the electron beam coming out of the sample towards the entrance slit of the dispersive element, on the other they accelerate or retard the beam in order to tune the particles kinetic energy to the pass-energy[2] of the analyser. This last aspect makes such lenses of pivotal importance for the energy-selection because a standard way to operate consists in working with a fixed pass-energy and varying the voltages applied to the lenses in order to change the kinetic energy E_k that will be, at the end of the optical transport, equals to the pass-energy. As an example, working with a pass-energy of 20 eV if one want

[2]Pass-energy is the energy value for which an electron can travel across the dispersive element coming out from the exit slit. The concept of pass-energy will be discuss in section 3.3.2

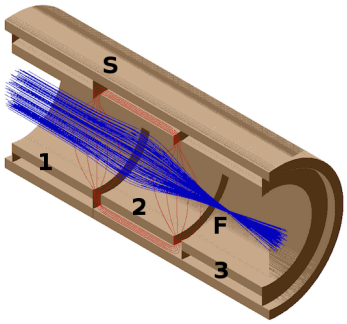

(a) An array of three electrostatic lenses (labelled as 1, 2 and 3) is sketched. A circular source is positioned on the left side. Forced by the electrostatic potential due to the cylindrical polarised electrodes, paraxial electrons are focused in the F point. The blue lines inside the electrodes are representing the electrons trajectories. S marks the electrostatic shield.

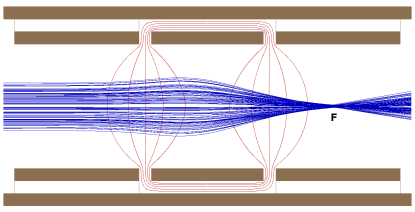

(b) Side view of the same array of lenses reported in panel (a). Equipotential lines are shown besides the electrons' trajectories. Equipotential surfaces act on a charged particle like physical surfaces of optical lenses do on rays of light.

Figure 3.8: Example of electrostatic lenses. Figures courtesy of Mr. Valerio Lollobrigida.

to analyse incoming electrons with $E_k = 100$ eV a retarding potential of 80 eV has to be applied. Electrons with $E_k = 101$ eV will be retarted in this case at 21 eV which is different from the utilised pass-energy and so will not able to pass through the dispersive element. Hence in order to detect electrons with different kinetic energy the applied voltages must be changed.

Another operation mode instead foresees to keep constant the retard varying the pass-energy according to the kinetic energy of the incoming electrons.

Typically the sample is grounded and in the same way the first electrode, in order to avoid electrostatic fields that will affect the trajectory between the sample and the lenses. The last electrode is biased with a potential value V_p defined by the pass-energy E_p. As a general rule an electron that passes across the i-th electrode has an energy of

$$E_i = E_k + eV_i$$

where E_k is the kinetic energy of the emitted electron and V_i the voltage applied to the i-th electrode. This implies that the voltage of the last lens is easily determined

$$V_p = \frac{E_p - E_k}{e}.$$

The intermediate lenses have the role to transport the electron beam and focus it onto the entrance slit of the analyser. When a charged particle enters an electric field it will result accelerated or decelerated and its trajectory will depend upon the angle of incidence with respect to the equipotential surfaces. The same is for an entire electron beam inside an electrostatic lens array where the (de-)focusing effect is manifested passing from a region with a potential V_1 to one with a potential V_2. Called α_1 and α_2 the incident and refractive angles respect to the normal of the equipotential surfaces, the parallel momentum conservation law

$$mv_{1\parallel} = mv_{2\parallel} \Rightarrow mv_1 sin\alpha_1 = mv_2 sin\alpha_2$$

along with the fact that for a charged particle that originates at ground potential with no kinetic energy the relation

$$\frac{1}{2}mv^2 = eV \tag{3.5}$$

is valid, leads to the equivalent, for electrostatic lenses, of the Snell's law:

$$\sqrt{V_1} sin\alpha_1 = \sqrt{V_2} sin\alpha_2. \tag{3.6}$$

This last relation shows clearly that when an electron beam passes from a region with a potential V_1 to a region with potential V_2, if the values are in the relation $V_1 < V_2$ the beam is squeezed, whereas in the opposite case ($V_1 > V_2$) is broadened. Equation (3.6) can be written in a more suitable form accounting for the beam diameter and divergence in the so called Helmoltz-Lagrange relationship [92]

$$d_1\alpha_1\sqrt{E_1} = d_2\alpha_2\sqrt{E_2} \tag{3.7}$$

where d is the diameter and α the divergence of the beam. In our case the two points labelled as 1 and 2 correspond to the source and the entrance slit of the analyser, so these two energies are E_k and E_p respectively.

Starting from equation (3.7) it is possible to define the magnification of the system

$$\sqrt{\frac{E_k}{E_p}} = \left(\frac{d_2}{d_1}\right)\left(\frac{\alpha_2}{\alpha_1}\right) = Mm$$

both linear $M = \frac{d_2}{d_1}$ and angular $m = \frac{\alpha_2}{\alpha 1}$.

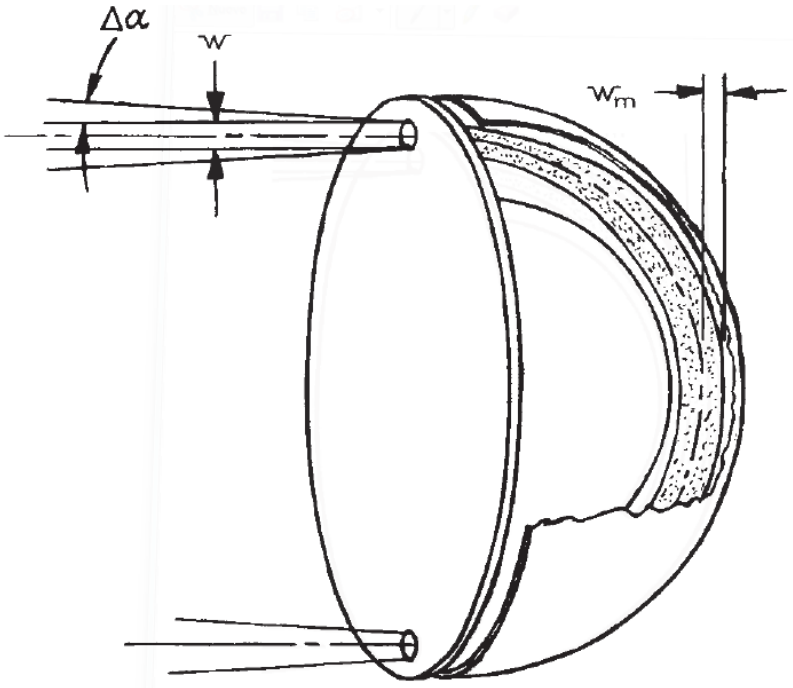

Figure 3.9: Schematic picture of a 180° hemispherical detector. The two hemispheres and the base plate are shown. On the base plate the entrance and exit slits are also sketched. w is the aperture of the entrance and exit slits, $\Delta\alpha$ the maximum angular deviation of an incident trajectory, and w_m the maximum deviation of a trajectory from the central path through the analyser. From [92].

3.3.2 Hemispherical analysers

The dispersive elements in use at the ALOISA beamline are 180° hemispherical electron analysers. Such devices are made by two concentric spherical electrodes across which a central field is established. As depicted in figure 3.9 these two hemispheres are mounted onto a base plate in which an entrance and an exit slits are located. The working method of an hemispherical analyser is quite simple: properly biasing the spherical plates, only electrons arriving perpendicularly to the center of the entrance slit with a particular energy value, named pass-energy E_p, are able to centrally escape from the exit slit after having travelled along an arc of circumference with radius R_0, given by the simple relation

$$R_0 = \frac{1}{2}\left(R_{\text{ext}} + R_{\text{in}}\right)$$

where $R_{\text{ext (in)}}$ represent the radius of the external (inner) sphere. Electrons with higher or lower energy, but inside the energy resolution, are able to escape from the exit slit in different positions, hence using a position sensitive detector it is possible to achieve the energy discrimination and a parallel acquisition. These analysers can work in a constant pass-energy mode and it results simple to determine the correct voltages which must be applied as a function of the chosen pass-energy.

The motion of an electron with $E_k = E_p$ inside the analyser is driven by the proper balance between the Coulomb and the centripetal forces. Such a balance can be expressed as

$$\frac{mv^2}{r} = e\mathcal{E}(r). \tag{3.8}$$

The electric field inside the analyser reads

$$\mathcal{E}(r) = \frac{\Delta V}{r^2}\left(\frac{1}{R_{\text{in}}} - \frac{1}{R_{\text{ext}}}\right)^{-1} \tag{3.9}$$

Now combining equations (3.8) and (3.9) for $r = R_0$ it is possible to obtain the relation between the potential difference among the analyser's plates ΔV and the pass-energy E_p:

$$\Delta V = \frac{2E_pR_0}{e}\left(\frac{1}{R_{\text{in}}} - \frac{1}{R_{\text{ext}}}\right)$$

so, for a given couple of hemisphere plates, the pass-energy define the bias voltage.

When a particle enters the analyser, its incident angle and energy will determine its trajectory and if these values are too far from the working parameters of the analyser this particle will be lost. The slits mounted onto the base plate play a significant role in determining the energy resolution via their width: let's assume a slit's width W, a mean radius R_0 and an incident angle α with the normal direction from the entrance slit plane, the energy resolution reads [92, chapter 5]

$$\frac{\Delta E}{E_p} = \frac{W}{2R_0} + \frac{1}{2}\alpha^2 \tag{3.10}$$

The central field inside an hemispherical analyser drives the particles' motion to follow a branch of a conic curve. The energy window expressed by equation (3.10) limits maximum deviation of a trajectory from the central path with radius R_0 for an electron able to outcome the analysers [92, chapter 5]:

$$\frac{\alpha_{\max}}{R_0} = \frac{\Delta E}{E_p} + \alpha + \frac{1}{2\alpha}\left(\frac{W}{2R_0} + \frac{\Delta E}{E_p}\right)^2.$$

In the experiments presented in this thesis we used the six analysers equipping the experimental chamber of the ALOISA beamline whose angular acceptance is of $\sim \pm 2°$. The five axial analysers have a mean radius of $R_0 = 33$ mm and entrance and exit slits of $W \simeq 2$ mm aperture, while for the bimodal one $R_0 = 66$ mm and no exit slits are present because a position sensitive detector is placed at the end of the dispersive element. The analysers' energy resolution depends upon the chosen pass-energy as expressed in equation (3.10): for the axial analysers ΔE is the $\sim 3.5\%$ of the pass-energy, while for the bimodal only the 1%. For this thesis we worked with axial analysers at a pass-energy of $E_p = 120$ eV and the bimodal one at $E_p = 100$ eV, so the energy resolutions were $\Delta E_{\text{axial}} \simeq 4.3$ eV and $\Delta E_{\text{bim}} \simeq 1$ eV.

3.3.3 Channeltron, Micro-channel Plate and Delay anode

Channeltrons and Micro-channel Plates (MCP in the following) are respectively single- and multi-channel electrons detectors. Let us spend, first, few words on a channeltron detector. In figure 3.10a a channeltron picture is shown. Such a device has an inner coating made by particular material with high secondary emission rate. This in order to permit the emission of at least two secondary electrons per every impinging electron. For such an aim, peculiar paths have been designed and an example is given in figure 3.10b. Large

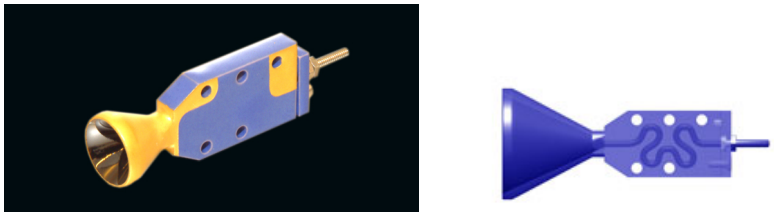

(a) (b)

Figure 3.10: External view (a) and designed path (b) of a single channel electron multiplier. Figures from [93].

voltage, of the order of few kV, is applied between the mouth and the rear of the channeltron. This means that starting with a single electron, not able to trigger alone the electronics, we are able to collect a measurable current at the collector as schematically depicted in figure 3.11. As presented in this figure the current pulse shows a time spread even if the electron path is designed in order to minimize differences in electrons' trajectories. Its nature is statistical and depends on the impact position of the incoming primary electron. Typical values are around $\Delta t \simeq 2$ ns and in order to reduce the time spread, the use of high voltages can give an help, because high electron energy means low energy uncertainty. The time spent by the electrons in covering the whole path is called average electron transit time and usually is around $20 - 80$ ns.

For an electron multiplier a gain coefficient can be defined as

$$\delta = \frac{N_s}{N_p}$$

where N_s represents the number of secondary electrons while N_p the number of incoming primary ones. An incident electron produces δ secondary electrons. The cascade process is such that in the second stage of emission δ^2 electrons are produced, δ^3 will be produced in third stage and so on, leading to an overall gain of

$$G = \delta^n.$$

Such a gain is a function of the applied voltage ΔV_{ch} between the mouth and the rear of the channeltron and its behaviour is reported in figure 3.12. The higher the bias the higher the electron energy, so a deeper electron impact into the channeltron's walls has to be expected upon increasing ΔV_{ch}, hence the multiple scattering process leads to the emission of more secondary electrons per primary electron impact. For this reason a first increase of the gain upon increasing the applied bias is expected. Anyway at a certain point space charge effects inside the channel will prevent the gain from increasing further

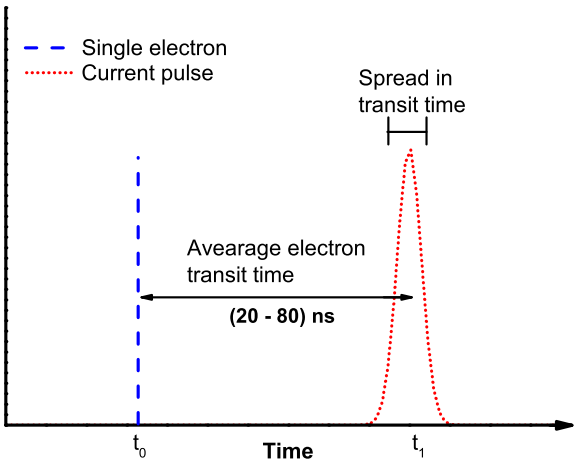

Figure 3.11: Effect of the transit time inside a channeltron: the impinging electron, represented as a delta function, starts the production of an electron avalanche which travels across the multiplication path of the channeltron. The average transit time and the time spread due to differences in electron trajectories are graphically explained.

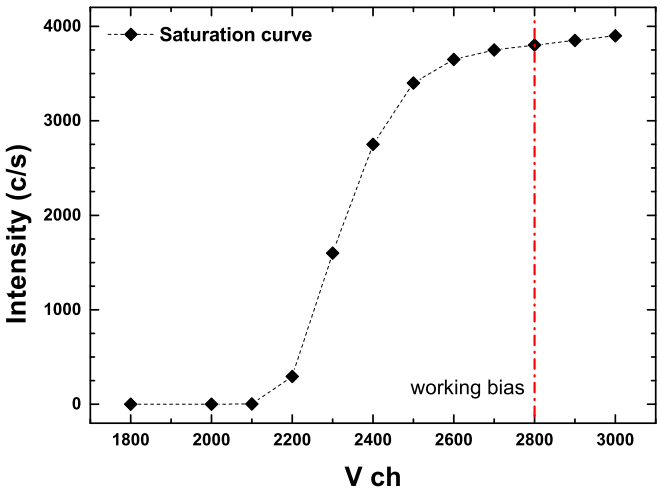

Figure 3.12: An example of saturation curve of a channeltron: the count rate, black filled diamonds, at the end of an electron multiplier is given as a function of the applied voltage. Electrons impinging onto the entrance cone have a fixed kinetic energy. After a linear increase a plateau is reached. The working applied voltage is marked with a red dash-dotted line. This signal is proportional to the channeltron's gain, hence it represents the gain vs voltage behaviour.

and saturation will be reached, hence the δ-factor becomes bias-independent, that represents the best working condition.

For single pulse operation typical gains for a channeltron are $\delta = 10^6 - 10^8$ and its mean-life, so the time in which the multiplier is usable, is around 10^{10} counts.

An MCP is instead a two-dimensional position sensitive detector made by a matrix of $10^4 - 10^7$ electron multipliers similar to a channeltron but miniaturised to a $10 - 100\,\mu m$ diameter tubes and aligned to one other as reported in figure 3.13. The length of such straight channels is given in terms of the length-to-diameter ratio, α, and typical values are $\alpha = 40 - 100$. These channels are usually realised inside a lead-glass plate properly optimised for the secondary emission, i.e. reducing the work function as in the case of a channeltron, and rending semiconductive the inner walls of each channel in order to restore the number of electrons, once emitted, via an external bias. A multiplication factor of $10^4 - 10^7$ is obtained polarising these

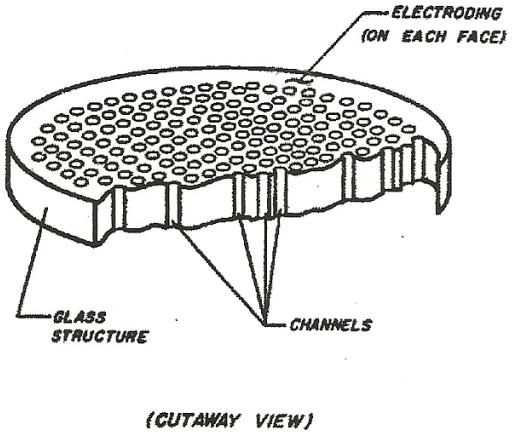

Figure 3.13: Schematic view of a lead-glass plate of an MCP. Figure from [94].

channels via two Nichrome or Inconel electrodes deposited on both sides of the plate and the side-to-side impedance is of the order of $10^9\,\Omega$. The spatial resolution is determined by the channel diameter and the center-to-center distance respectively $12\,\mu m$ and $15\,\mu m$, while the time resolution is less than 100 ps [94]. For a straight channel and for secondary emission normal to the walls it is possible to define a gain given by [95]:

$$G = \left(\frac{AV}{2\alpha V_0^{1/2}} \right)^{4V_0\alpha^{1/2}/V} \tag{3.11}$$

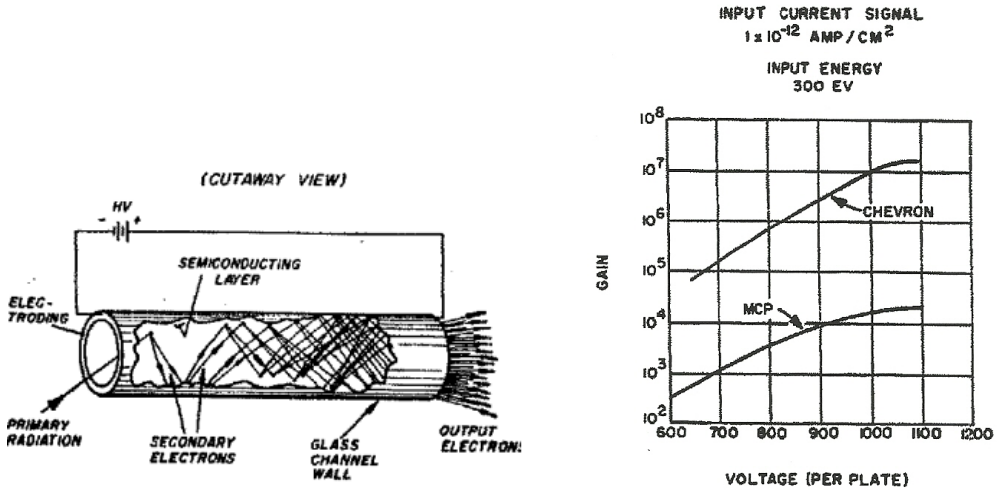

(a) (b)

Figure 3.14: A straight channel electron multiplier is sketched in its basics in panel (a). The Gain vs Voltage characteristics of an MCP is given in panel (b). Figures from [94].

where A is a proportionality constant that bonds the electron energy collision V_c to the number of emitted electrons δ via the simple relation $\delta = AV_c^{\frac{1}{2}}$, α is the length-to-diameter ratio, V_0 the initial energy of an emitted secondary electron (typically 1 eV) and once again a dependence from the applied voltage V is shown. As well as the case of a single-channel electron multiplier, increasing the applied voltage the gain increases up to reaching a saturation as reported in figure 3.14b. Equation (3.11) exhibits a maximum in the gain as a function of the α-ratio, and imposing $\frac{\partial lnG}{\partial \alpha} = 0$ it is found [94]:

$$\begin{aligned} \alpha_M &= \frac{AV}{3.3V_0^{\frac{1}{2}}} \simeq \frac{V}{16.5} \\ G_M &= exp\left(0.184A^2V\right) \simeq exp(0.0074V) \end{aligned}$$

with α_M and G_M the length-to-diameter ratio and gain at the maximum point respectively.

In the straight channel of the detector reflections due to positively-charged ions lead to the spurious-pulses generation. These ions are produced mainly in the last stage of the multiplication channel under the electron bombardment of the residual gas (typically at a pressure $> 10^{-6}$ hPa) desorbed by the channel's walls. These ions, drifting back to the beginning of the multiplication tube, can produce additionally secondary electrons. In order to

reduce such an effect, two (or more) different plates, with channel orientation properly biased with respect to one other (typical angles are around 8°), can be used in the so called *Chevron configuration* shown in figure 3.15. Such a configuration guarantees that ions produced in the last section of the last MCP cannot reach the beginning of the multiplication stage, increasing the multiplication factor up to 10^7. This can be achieved not only because the multiplication length is increased, but also because passing through different plates, because of the bias angle, electrons coming from a single channel in the first plate will involve more than one channel in the second plate.

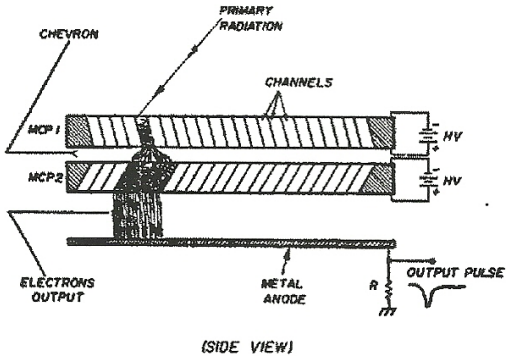

Figure 3.15: Two MCP in Chevron configuration. The primary radiation starts the electron avalanche in the front plate and at the end plate more than one channel is involved in multiplying electrons reaching a gain of 10^7. Due to the bias angle (typically 8°) ions produced in the last sector of the rear plate cannot drift back to the first one. Figure from [94].

The peculiarity of this kind of devices remains the possibility to couple them with proper position sensitive devices in order to discriminate the arrival position of the electrons. This characteristic can be exploited in energy-resolved experiment in order to simultaneously acquire electrons with different kinetic energies coming out a dispersive element. The arrival position information can be achieved using a so called *cross delay line*, XDL, as in the case of the MCP equipping the bimodal frame. A XDL consists in a couple of orthogonal serpentines crossed in order to realize a two-dimensional lattice [96]. When the electron avalanche reaches the anode, the induced signal inside the XDL starts to propagate itself across the two lines towards the four ends of the lattice. Introducing a proper delay line it is possible to obtain the spatial position from the arrival time delay at the ends of the lines. This delay is linearly proportional to the travelled path inside the line, hence the information about the spatial coordinates is obtained. This information

can be digitalized cabling the wire ends of each serpentine to the start and stop input of a time to digital converter (TDC) as reported in figure 3.16.

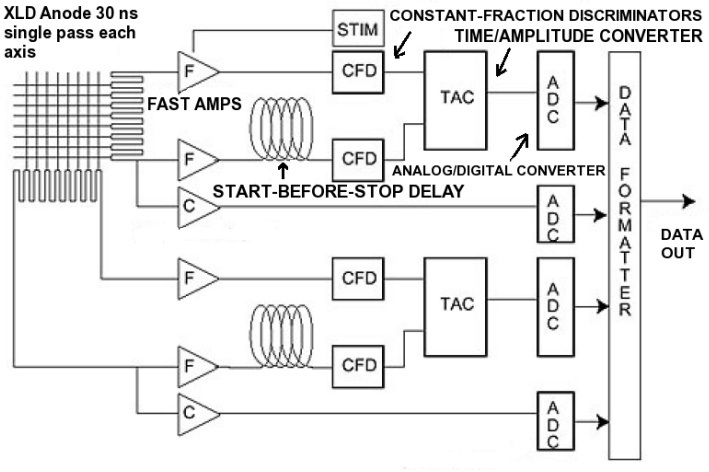

Figure 3.16: Scheme of electronic processing chain for a XDL. The low-level charge pulse is amplified and for one end of each serpentine a delay, slightly more than the overall delay of the anode, is added. The fast signals are processed by CFDs and the output time difference among signals coming from the ends of the same line is converted in an analog value via a TAC. The analog-to-digital conversion at the end gives back the digital information of the centroid position of the charge pulse onto the 2D-lattice. Figure redrawn on the base of [97, Fig. 5].

3.4 Coincidence acquisition chain

In a coincidence experiment the time information of the emitted electrons plays a fundamental role in disentangling true coincidence events among all the electron-pairs emitted. For this reason a dedicated acquisition chain must be used. For the experiments proposed in this thesis a common coincidence acquisition chain was employed, and in the following a brief description will be given.

The coincidence acquisition chain equipping the ALOISA beamline is schematically depicted in figure 3.17. The signals coming out the MCP of the bimodal analyser is given as start input, while the signal coming out the axial analysers as stop input of a time-to-amplitude converter (TAC). In their basics the acquisition chains consist of a pre-amplifier (pre-amp in the following), a constant-fraction discriminator (CFD), a digital delay generator

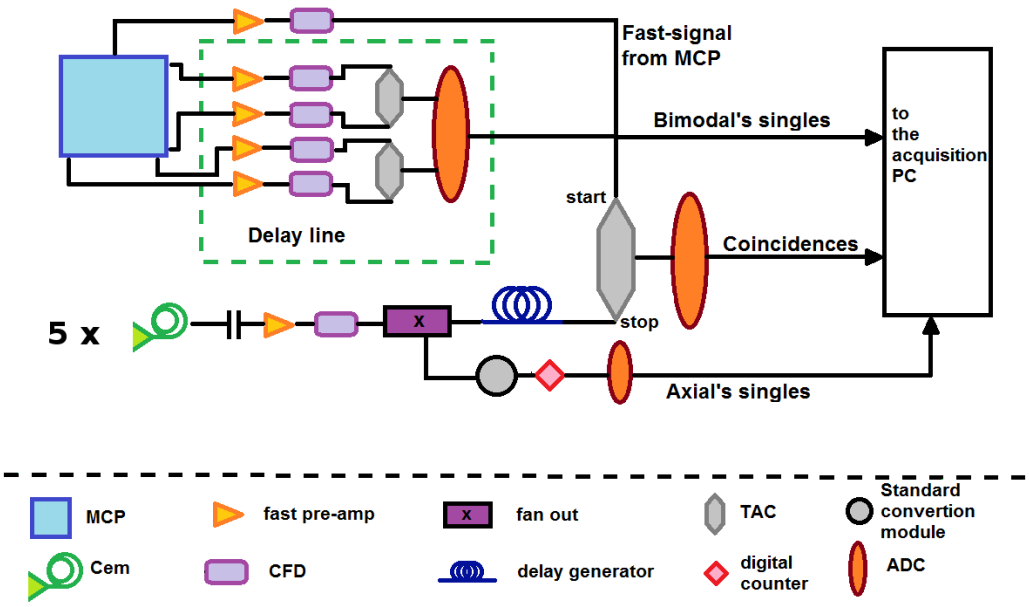

Figure 3.17: Coincidence acquisition chain schematically sketched: the fast signal coming from the MCP and the signal coming from one of the axial analysers are given as start and stop input of a TAC respectively. For a kinetic energy pair (E_1, E_2) the difference in arrival time of the detected electrons is recorded.

unit (or a delay line), a TAC and an analog/digital converter (ADC). Modules for conversion stages of signal-standard (e.g. NIM to TTL) can be present. The pre-amps at the beginning of the acquisition chain have the role to amplify the low-level pulse coming from the detector into a high-level pulse able to trigger the electronics. In order to distinguish true signal against the noise or pulse-replicas, coming from signal reflections, a CFD is used. In a CFD a signal that exceeds a threshold value is triggered at a constant fraction of the input pulse height, overtaking the so called problem of *time walk*[3] preserving the time information. While the fast signal coming from the bimodal's analyser is sent to the start input of a TAC, in the axial's electronics chains a delay generator have the role to shift in time the signal travelling, in a way that the simultaneous emission of two electrons will result at a specific delay. This second pulse is given as the stop input of the TAC. The difference in arrival time $\Delta t = t_1 - t_2$ between the photo- and Auger electrons is converted in a pulse whose intensity is proportional to such a delay. A subsequent multichannel pulse-amplitude analyser histograms the number of electron-pairs that show a certain delay. In order to prevent the formation of spurious pulses, such as replicas of the coincidence signal, the electronics is provided with an inhibition circuit that cannot permit the processing of two consecutive starts signals before a stop has arrived, that means it is not possible to collect a second Auger electron if a photoelectron has not arrived yet.

In this way the difference in arrival time distribution is fully determined for each kinetic energy pair (E_1, E_2) of the experiment and the so called *time spectrum* is achieved.

3.4.1 Raw data: time spectrum

In figure 3.18 a time spectrum collected in one of the experiments proposed in this thesis is presented. It consists in a peak located at $\Delta t = 160$ ns due to electrons promoted in the continuum in the same physical event superimposed to a continuous background due to uncorrelated electrons. While between correlated electrons, that are coming from the same event, a fixed

[3]The use of a discriminator in time measurements is affected by two main problems called "time walk" and "time jitter". The first one, typical for threshold discriminators, is due to the fact that also if two pulses take place simultaneously, if characterised by two different pulses height, they exceed the threshold in different times, resulting as if they occurred not at the same moment. Time jitter is, instead, a time uncertainty contribution coming from the fact that the rise of a pulse is not completely smooth, but is modulated and this make difficult to properly determine the exact moment in which the signal exceeds the threshold.

delay (set-up in the acquisition chain as shown in figure 3.17) is found, for uncorrelated ones a continuous distribution on the whole accepted time window (300 ns in this case) is expected. The background due to random coincidence events reported in figure 3.18 is clearly triangular and this because it reflects the source properties, in this case Synchrotron Radiation, representing the self convolution of the ring fill pattern[4] [91]. About the true coincidence

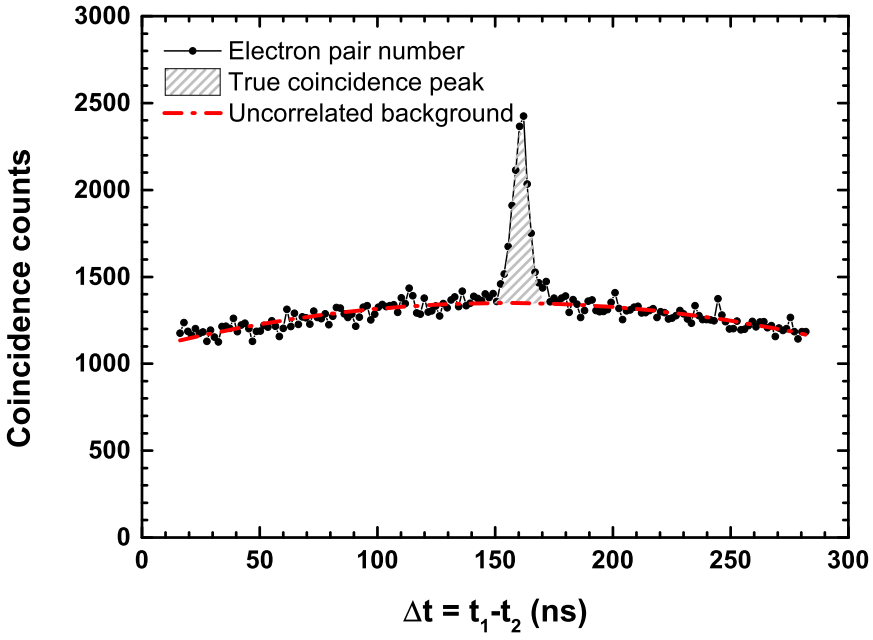

Figure 3.18: A collected time spectrum. The true coincidence peak, grey area, is superimposed to a continuous background due to uncorrelated electrons that reflects, via its shape, the self convolution of the ring fill pattern. A polynomial choice of background is reported as dot-dashed red line. Background subtraction under the peak area permits to obtain the true coincidence events number.

peak width, of ($\delta t \simeq 8$ ns),this is mainly due to differences in transit time of electrons inside the analyser.

Further consideration on the optimisation for a coincidence experiment will discuss in the following. A central problem in such an experiment is the low coincidence count rate and, as shown in figure 3.18 the high background

[4]The ring fill pattern has a square-wave profile and the self convolution of a square-wave is a triangular wave.

from accidental coincidences. To understand which parameters can be optimised in order to reduce the time needed to collect a spectrum, let us briefly discuss the emitted electron current contributing to true and accidental coincidences.

Following the approach proposed by Haak in his thesis work [98, chapter 2] let ρ be the rate of production of photoelectrons per unit length inside a sample (in the following represented by the subscript ph), their escape rate (E_{ph}) is obtained integrating over all the possible distances of production, x, from the surface and considering an exponential attenuation with a mean free path λ_{ph}

$$E_{ph} = \int_0^\infty \rho e^{-\frac{x}{\lambda_{ph}}}\, dx = \rho\lambda_{ph}.$$

A target with a core-hole will decay via both fluorescence or auto-ionising (Auger) processes. If D is the fraction of photoionisations that will decay via the Auger process under investigation, the escape rate of Auger electrons (E_A) is

$$E_A = \rho\lambda_A D$$

where λ_A is the Auger electrons' mean free path. To collect a coincidence event the escape of both the photoelectron and the Auger electron is required, hence the rate $E_{ph,A}$ at which both electrons emerging from the surface is given by

$$E_{ph,A} = \int_0^\infty D\rho e^{-x\left(\frac{1}{\lambda_{ph}}+\frac{1}{\lambda_A}\right)}\, dx = \rho D\frac{\lambda_{ph}\lambda_A}{\lambda_{ph}+\lambda_A}. \tag{3.12}$$

The rate of photoelectrons (Auger electrons) $P_{ph}\,(P_A)$ detected depends upon the angular acceptance α_{ph} (α_A) and efficiency C_{ph} (C_A) of the dedicated electron analyser:

$$\begin{aligned} P_{ph} &= \rho\lambda_{ph}\frac{\alpha_{ph}}{4\pi}C_{ph} \\ P_A &= \rho\lambda_A\frac{\alpha_A}{4\pi}DC_A. \end{aligned}$$

Taking into account for equation (3.12), the true coincidence count rate results:

$$I_T = \rho\frac{\lambda_{ph}\lambda_A}{\lambda_{ph}+\lambda_A}\frac{\alpha_{ph}}{4\pi}\frac{\alpha_A}{4\pi}C_{ph}DC_A$$

while for accidental coincidence events, because they originate from uncorrelated events, the count rate is given by the simple product of the photoelectron and Auger electron detection rate and by the resolving time τ that is the accepted time window in which two emitted electrons, even if uncorrelated, are considered as coincident:

$$I_{Ac} = \rho^2\lambda_{ph}\lambda_A\frac{\alpha_{ph}}{4\pi}\frac{\alpha_A}{4\pi}C_{ph}DC_A\tau.$$

The true to accidental ratio is straightforwardly determined:

$$\frac{I_T}{I_{Ac}} = \frac{1}{\rho\,(\lambda_{ph} + \lambda_A)\,\tau}. \tag{3.13}$$

As reported by Jensen and co-workers [99] the accuracy achieved in a coincidence experiment is ruled by the $\frac{I_T}{I_{Ac}}$ ratio. Such a ratio is inversely proportional to the incident photon flux, $\frac{1}{I_0}$, and to the coincidence resolving time. Equation (3.13) is enough to show that the higher the incident photon flux (that means high ρ) the lower the true-to-accidental ratio. In the same work it is also pointed out that the acquisition time t shows the same $\frac{1}{I_0}$ dependence and is inversely proportional to the accepted solid angle of the coincidence apparatus. This means that once a saturation condition has been reached, the lower level of incident photon flux has to be used. Ultimately, the best compromise is to work with a proper photon flux in order to get $\frac{I_T}{I_{Ac}} \simeq 1$. This last condition sets the singles rate for a given true coincidence rate.

Let us now express the true and accidental coincidence rate in another way. Let R be the rate per unit volume of photoionisation in the sample, τ the resolving time of the experiment and t the total acquisition time. Let $F_{ph}(x, y, z)$ and $F_A(x, y, z)$ represent respectively the probability that a photoelectron is produced in (x, y, x) and, consequently, an Auger electron is detected, including in the first one the angular acceptance and the probability of no-loss escape and in the latter the fluorescence yield and the branching ratio for the Auger transition of interest. Hence the rate of detection of photoelectrons, R_{ph}, and Auger electrons, R_A result as follow:

$$R_{ph\,(A)} = R \int_V F_{ph\,(A)}(x, y, z)\, dV$$

where the integral is over the illuminated volume of the specimen. Going to explicit the fluorescence yield contribution, $h_{ph\,(A)}$ (position independent), the probability that an electron falls within the accepted angle $\alpha_{ph\,(A)}$ (position independent), the contribution for the escape probability $e^{-\frac{z}{\lambda cos\theta}}$ with z perpendicular to the sample surface, λ the escape depth (assumed identical for both electrons) and θ the angle between the escape direction and the surface normal, chance and true rates read [98, chapter 3]:

$$\begin{aligned} C &= R_{ph}\, R_A\, \tau = R \int_V F_{ph}\, dV\; R \int_V F_A\, dV\; \tau \propto R^2 \lambda^2 \tau h_{ph} h_A \alpha_{ph} \alpha_A A^2 \\ T &= R \int_V F_{ph} F_A\, dV \propto R \left(\frac{\lambda}{2}\right) h_{ph} h_A \alpha_{ph} \alpha_A A. \end{aligned} \tag{3.14}$$

A represents the sample area, while angular dependence has been neglected. From equations (3.14) the true-to-accidental ratio results

$$\frac{T}{C} = \frac{1}{2\lambda RA\tau} \propto \frac{\alpha_{ph}\alpha_A}{\tau}$$

showing that there is no advantage in using large samples and in order to maximise the $\frac{T}{C}$ ratio the increasing of the accepted solid angle or the reduction of the resolving time is requested. Of course these requirements are in conflict with energy and angular resolution.

The width τ of the true coincidence peak, or resolving time, rises from several contribution that will be illustrated following the work by Völkel and Sandner [100]. Let us consider a single couple of electron analysers collecting electron-pairs, the total resolving time is give by the sum of the time spread affecting the electrons travelling from the sample towards the detector for each detection line

$$\tau = \Delta t_{ph} + \Delta t_A.$$

This spread $\Delta t_{i=ph,A}$ can be decomposed as follows:

$$\Delta t_i = \Delta {t_i}^{\text{vol}} + \Delta {t_i}^{\text{energy}} + \Delta {t_i}^{\text{geometric}} + \Delta {t_i}^{\text{detector}} + \Delta {t_i}^{\text{electronics}}.$$

Let us now briefly discuss the role of each term:

1. $\Delta {t_i}^{\text{vol}}$ represents the time spread that electrons undergo inside the interaction volume. This can be expressed as the ratio between the escape depth of the electrons and their velocity

   $$\Delta {t_i}^{\text{vol}} = \frac{d}{v} = \frac{d}{\sqrt{2E/m}}.$$

   It is quite easy to verify that this contribution is absolutely negligible, e.g. for electrons with escape depth of $5 - 10$ Å and few tens of eV this value is less than 10^{-6} ns.

2. $\Delta {t_i}^{\text{energy}}$ represents the contribution arising from the finite energy resolution of the electron analyser. A difference in transit time of the electrons inside an hemispherical analyser is present also if we consider electrons entering the analyser with a fixed incident angle α_0 because of its energy resolution ΔE. Indicating D the distance between the sample and the detector such a time spread (neglecting the fact that the electron kinetic energy varies inside the lens due to the applied bias) reads

   $$\Delta {t_i}^{\text{energy}} \sim \frac{D}{2}\sqrt{\frac{m}{2E}}\frac{\Delta E}{E}.$$

We can estimate D considering the arc of circumference inside the analyser plus the sample-analyser distance d (considering both the distance between the sample surface and the length of the lens array), hence $D = d + \pi R_0$. For $R_0 = 33$ mm an overall distance $D \sim 300$ mm has to be considered. For electrons of $E = 100$ eV and an energy resolution of $\frac{\Delta E}{E} \sim 2\%$ this term contribute with $\Delta t_i{}^{\text{energy}} \sim 1$ ns.

3. $\Delta t_i{}^{\text{geometric}}$ represents the time spread due to different paths followed by electrons with a fixed energy but entering the analyser with different incidence. Such a term depends upon the analyser type, its angular divergence $\Delta\theta$, the total transit time, hence the field experienced by the particles. For an hemispherical analyser this term can be expressed using the approximated scaling relationship

$$\Delta t_i{}^{\text{geometric}} \sim \text{size}\, \Delta\theta\, E^{-1/2}$$

where "size" stands for the entrance slits dimension as well as mean radius respectively, taking into account for a contribution of both. Typical range for an hemispherical analyser is $\Delta t_i{}^{\text{geometric}} \sim 1 - 10$ ns. This represent the main contribution to the resolving time.

4. $\Delta t_i{}^{\text{detector}}$ represents the contribution due to the transit of the electronic avalanche inside the (single-) multi-channel electron multiplier detector. As reported in section 3.3.3 a couple of nanoseconds for a single channel electron multiplier and $\Delta t_i{}^{\text{detector}} \sim 100$ ps for an MCP must be considered.

5. $\Delta t_i{}^{\text{electronics}}$ represents the time jitter coming from the entire acquisition chain. Using fast-amplifiers and CFDs this value can be kept below the nanosecond.

As discussed above the main contribution to the resolving time comes from the different geometrical paths that electrons follow inside the optics and the hemisphere. In order to decrease this term the reduction of the accepted solid angle has to be considered, but again this is in contrast with requirements for the reduction of the total acquisition time and the attempt to find the proper compromise among all the parameters involved makes difficult to perform a coincidence experiment.

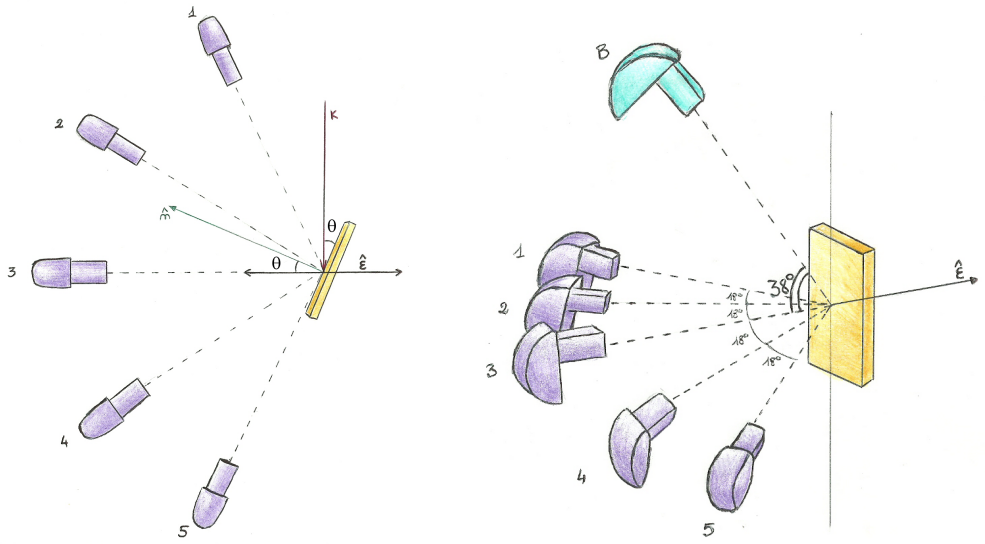

(a) (b)

Figure 3.19: The experimental geometry for coincidence measurements is reported. The five light purple axial analysers, labelled from 1 to 5 are dedicated to collect photoelectrons, the light blue analyser, labelled as B, is the bimodal one dedicated to scan the MVV Auger spectral region. In the top-view of panel (a) the light momentum and polarisation are shown. θ represents the tilt angle.

3.5 Experimental geometry in AR-APECS experiments

As explained in section 2.3.2 it is possible to probe electron-pairs contributing to the partial Auger yield belonging to different multiplet spin terms, so the knowledge of the experimental geometry is an essential information. In the following the geometries used in the experiments proposed in this thesis will be discussed.

The experimental apparatus used in these experiments consists in the six electron energy-analysers equipping the experimental chamber of the ALOISA beamline. As discussed in previous sections, these analysers are mounted on two different frames called Axial frame, which hosts five single channel analysers, and Bimodal frame, which host a multichannel analyser. In the following the analysers will be labelled as An1 to An5 for the Axials, while B for the Bimodal, according to figure 3.19b. In figure 3.19a a top view of the axial analysers is given. The optical axes of these analysers are directed to the sample surface lying in the plane defined by the momentum $\vec{k}$ and the polarisation $\hat{\varepsilon}$ of the photon beam, i.e. perpendicular to the sample

surface. They are located 18° apart to each other in order to get the axis of An3 aligned with $\hat{\varepsilon}$, An2 and An4 18° apart from the polarisation vector, finally An1 and An5 36° far from the electric vector of the impinging photon. In the experiments proposed in this thesis the bimodal analyser is oriented 38° apart with respect to the axial plane. It is straightforward to determine the two different kinematics used in our experiments, since the Auger electrons are collected only with the B analyser, they are always Not aligned (N) with respect to the polarisation vector $\hat{\varepsilon}$, which acts as quantization axis. Regarding the photoelectrons, collected by the axial analysers, it is possible to distinguish two different conditions: when electrons are collected within $\sim 20°$ from $\hat{\varepsilon}$ they can considered Aligned (A) with $\hat{\varepsilon}$ and this is the case of electrons collected by analysers An2, An3 and An4. On the contrary electrons collected by analysers An1 and An5 have to be considered Not aligned (N). This kinematics attribution is made on the basis of what is reported in [29] where it is shown that both Auger electrons of 56 eV and photoelectrons of 156 eV, similar to those detected in our experiments, if collected within $\sim 20°$ with respect to the light polarisation, will be mainly characterised by the angular momentum projection $m = 0$, while at larger angles $m = \pm 1, \pm 2$ became considerable.

Combining analyser-pairs it is possible to realise two different kinematic conditions: electron-pairs collected using analysers B with An2, An3 or An4 give rise to the AN geometry (where the first letter refers to the photoelectron and the second to the Auger electron), electron-pairs collected using analysers B coupled with An1 or An5 give rise to the NN geometry. The use of all this

Analyser	Kinematics
B	N
An1	N
An2	A
An3	A
An4	A
An5	N

Analyser-pair	Geometry
An1 + B	NN
An2 + B	AN
An3 + B	AN
An4 + B	AN
An5 + B	NN

Table 3.3: Experimental configuration for electron analysers in coincidence measurements.

six analysers is of great importance in our experiments not only because it enlarge the effective accepted angle without degrading the time and angular resolution of the spectrometer, but also because this allows to span the Auger spectral region for both the geometries at the same time. This guarantees that differences in AR-APECS spectra coming from the two kinematics, if

any, have their origin in the physical properties of the sample and they are not related to surface degradation.

Conventional (single) Auger spectrum is simultaneously collected for both the kinematics. Such a spectrum can be used as reference to show how APECS is a powerful tool to unravel multiplet terms not accessible in conventional spectroscopies.

Furthermore Gotter *et al.* have shown that collecting simultaneously both the single and the coincidence spectra in two different geometries (using a different analyser configuration with respect to the one reported in this thesis) for a Co/Cu(001) magnetic film single spectra were perfectly identical once superimposed while the AR-APECS spectra were characterised by a dichroism (DEAR-APECS). These findings have proven not only the already known selectivity of AR-APECS in the core hole state spin polarisation, but on the initial state spin polarisation as well [101], laying the basis for the use of this technique in the characterisation of magnetic materials.

In order to collect all this five electron-pairs simultaneously a proper alignment of the field of view of the analysers is necessary. The field of view of each analyser is the portion of space that falls within its accepted solid angle. This operation is needed in order to align the six fields of view and the impinging photon beam at the same point on the sample. This is realised moving both the beam, through the toroidal mirror, and the sample, via the manipulator. An example of a proper alignment is given in figure 3.20 where for each analyser is reported signal intensity for electrons with fixed energy as a function of the beam position moved acting on the toroidal mirror position. The best condition is obtained when the largest superposition of the different fields of view is achieved.

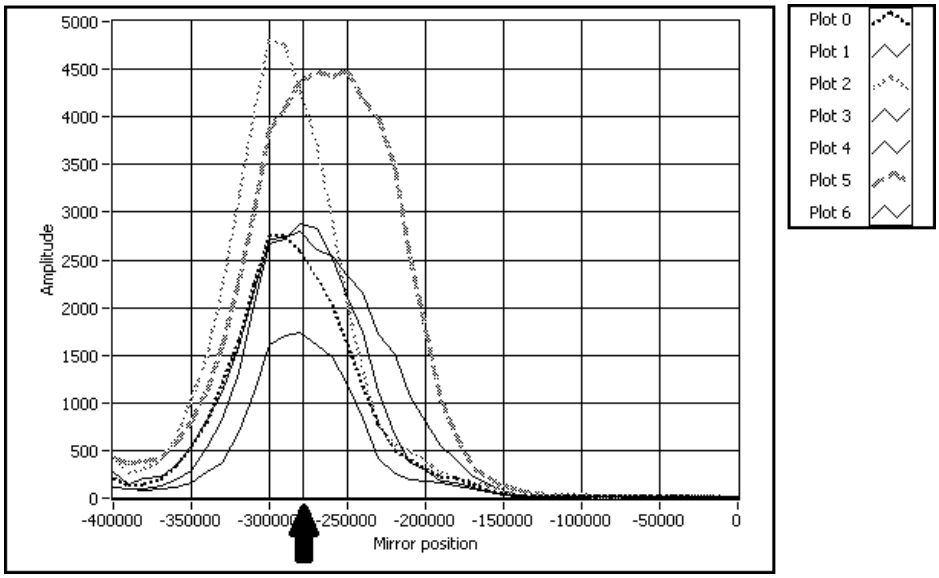

(a)

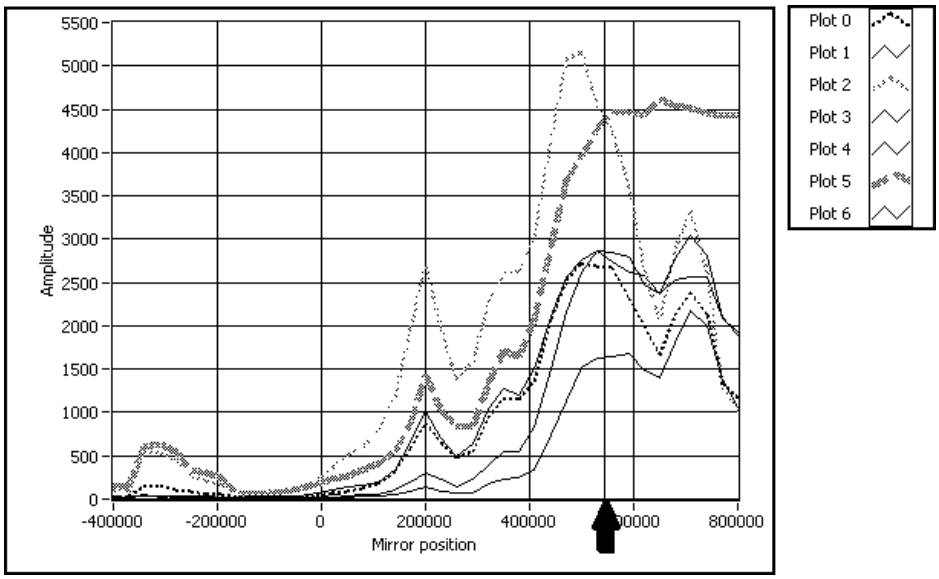

(b)

Figure 3.20: The field of view of the six analysers equipping the experimental chamber is given. For a given position of the manipulator, signal intensity for electrons of fixed energy is reported as a function of the mirror position. In panel (a) the independent variable is the rotational degree of freedom of the toroidal mirror, in panel (b) the translational one. Axial analysers are labelled as Plot0 to Plot4, bimodal one as Plot5. Plot6 is referred to an old configuration of the experimental chamber and is no longer used.

Chapter 4

Investigation of electronic spin coupling in magnetic systems by APECS

The origin of the magnetic properties of systems at atomic scale is a fundamental issue in magnetism. In solving this issue the comprehension of what happens around a single atom crossing the magnetic phase transition temperature is necessary.

Recent results [102, 103] seem to claim that in the $3d$-metal oxides the magnetic moments are atomically non zero well above the Néel transition temperature, anyway this issue still remains controversial and no unique view has been reached. In order to solve it a local sensitive spectroscopy, able to probe both FM and AFM systems, is desirable. It must be took into account that in the case of AFM systems probing the local magnetic order is more complex with respect to FM ones due to the fact that the spins change direction on scale of the first-neighbourous and very few techniques are able to give information (X-ray Magnetic Linear Dichroism is one of them).

Combining the element selectivity of the core level photoemission, which in turn means atomic site selectivity, with the sensitivity to the valence band correlation of the Auger spectroscopy, APECS shows itself as a suitable tool to probe electron correlation at atomic scale. Its locality is guaranteed by the fact that the two holes final state is projected onto the core hole state. The Coulomb matrix element involved, because it scales as $1/r$, suppresses decay channels in which the core hole of a certain atom is filled by the valence electron of a different site, leaving as the main contribution only those Auger processes involving a single atom.

In this work APECS has been applied to probe the $M_{23}M_{45}M_{45}$ Auger transition in $3d$ metals and their oxides. For these systems the magnetic

properties are strongly dictated by the behaviuor of their $3d$ levels. This means that we can investigate their magnetism probing electron correlation in the valence $M_{45} \equiv 3d$ levels. Particularly the AR-APECS capability to be sensitive to magnetic state, proved both on FM [104] and AFM [37], without having to rely on crystal periodicity or bulk thermodynamic measurements make this technique valid to contribute in solving the issue about the local origin of magnetism.

4.1 Unravelling final state spin multiplet terms in Antiferromagnetic system, the case of NiO

In this section the experiment performed on a NiO thin film [105] is presented. We measured the AR-APECS spectra in two different kinematics collecting the MVV Auger electrons coupled with $3p$-photoelectrons emitted upon the absorption of linearly polarised photons with $\hbar\omega = 250$ eV. In this way the $M_{23}M_{45}M_{45}$ partial Auger yield has been accessed. We measured such a spectral distribution once collecting the photoelectrons aligned with the polarisation vector of the light while the Auger electron was detected far from it, another time with both electrons collected not aligned with the electric vector. As expected with the use of the linearly polarised light we have been able to increase or decrease the relative intensity of different multiplet contributions (singlet, triplet and quintet) of the final state holes upon changing kinematic conditions. By comparing the experimental result with a cluster calculation based theoretical model an unambiguous assignment of the different spin spectral features has been obtained.

The AR-APECS spectra have been measured upon crossing the magnetic transition temperature, i.e. performing the experiment both below and above the Néel temperature and hence probing the system both in antiferromagnetic (AFM) and paramagnetic (PM) states. While $M_{23}M_{45}M_{45}$ Auger lineshape results different upon changing kinematics for the AFM phase, on the contrary the PM phase shows no differences in the spectral distribution.

4.1.1 The NiO/Ag(100) sample

Bulk NiO is an antiferromagnetic insulator of type-II at room temperature. It is characterised by a crystal structure of the NaCl type with a lattice parameter of $a_0 = 4.177$ Å. Its spin structure is characterized by a ferromagnetic order on the (111) planes, with magnetic moments aligned along a

$\langle 11\bar{2} \rangle$ direction, stacked antiferromagnetically along the $\langle 111 \rangle$ direction [106]. In our experiment a NiO thin film, grown on a silver substrate, has been investigated.

The NiO/Ag(100) samples have been grown in situ by means of electron bombardment of high purity rods of the corresponding metal onto the clean and well ordered, from a crystallographic viewpoint, (001) surface of a single crystal silver substrate. Cycles of Ar^+ ion sputtering and an annealing at about 750 K have been used to clean and order the substrate surface, resulting in x-ray photoemission spectra free of carbon and oxygen. The crystalline order has been checked by Reflection High-Energy Electron Diffraction (RHEED). We choose a silver substrate, even if characterised by a face centred cubic symmetry while the NiO shows a "rock salt" structure, because it allows for a NiO pseudomorphic growth (i.e. in register with the substrate) due to the little lattice mismatch close to 2% (schematic in figure 4.1). NiO have been obtained by depositing Ni atoms in an oxygen atmosphere with a partial pressure of $1 \cdot 10^{-7}$ hPa with the Ag(100) substrate kept at room temperature, followed by a post-annealing at 540 K in an oxygen atmosphere at pressure of $1 \cdot 10^{-6}$ hPa. It is known that such a procedure prevents the formation of metallic Ni cluster embedded in the Ag substrate [107, 108]. The crystalline structure of the grown NiO layer was monitored using the RHEED pattern which has shown the same (001) crystallographic surface of the substrate. Unfortunately we are lacking in RHEED patterns for NiO to show because they have not been recorded, saving precious time to perform the remainder of the experiment. The evaporation rate of about 0.2 Å/min was calibrated with a quartz-crystal microbalance. Photoemission spectra collected after the sample preparation were used to evaluate the thickness of the NiO layer.

4.1.2 Thickness estimation

As discussed in section 1.2.2 the transition temperature in a thin film, as well as the magnetisation direction, shows a thickness dependence. In our case we are interested in the determination of both the transition temperature and the plane in which magnetic moments are lying, hence, because the sample used in our experiment has been grown *in situ*, a proper characterisation is required.

As will be illustrated in the next section, discussing the case of FM systems, electron diffraction experiments can assist the sample growth, making the thickness estimation accessible. It is well known that NiO grown onto the Ag substrate shows electron diffraction intensity oscillations [109] and it is characterised by a layer-by-layer growth mode which take place after the

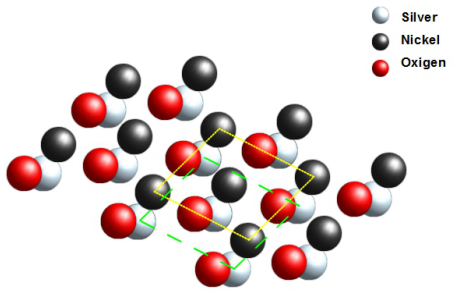

Figure 4.1: Schematic representation of the NiO/Ag(001) overlayer. Silver atoms (light grey spheres) of the (001) surface are ordered in a face centred cubic fashion, while the NiO atoms (Ni: grey spheres, O: red spheres) show a rock salt arrangement. The same (001) orientation of the NiO with respect to the Ag substrate, typical for a pseudomorphic growth, is sketched reporting the surface cell for both the Ag (dashed green) and NiO (dotted yellow) layers.

nucleation of two-monolayer-thick islands. Unfortunately, the geometry in our disposal in performing this experiment was such as to have the electron gun aligned to the back of the sample holder, thus preventing us to carry out the diffraction experiment. In order to fulfill the necessity of a proper characterisation of the sample, thickness estimation has been made on the basis of the models proposed in equations (2.5) and (2.6). The first one is the simple exponential attenuation model, better known as Lambert-Beer-Bouguer law, while the second is a model proposed by Fadley [59]. In order to satisfy the requirements for equation 2.5 a photoemission signal from the substrate has been collected both on the clean substrate and after the evaporation. The Ag-3d photoline is the best candidate due to its large cross-section, about 2 Mbarn at $\hbar\omega = 670$ eV, energy to collect survey spectra. By reverting equation (2.5) the film thickness can be obtained once the intensity of these photolines, shadow area under the peaks in figures 4.2a and 4.2b, and the electron mean free path inside the NiO layer are provided. The model of equation (2.6) is more complex instead and requires the acquisition of a signal coming from the substrate, again the Ag-3d, and one from the NiO overlayer, in this case we selected the O-1s line. The photoemission cross-section for both the Ag-3d and O-1s signals must be included in the model along with three different electron mean free paths: electrons coming from the substrate with energy $E_{\text{kin}} = E_k = E_{Ag_{3d}}$ have to travel first inside the Ag substrate and then inside the NiO layer, while electrons coming from the

Table 4.1: Atomic cross-sections and inelastic mean free paths used to estimate the film thickness from models (2.5) and (2.6).

Parameters for models (2.5) and (2.6) @ $\hbar\omega = 670$ eV	
$\Lambda_l(E_k = 290 \text{ eV})^+$	8 Å†
$\Lambda_l(E_l = 130 \text{ eV})^+$	5 Å†
$\Lambda_k(E_k = 290 \text{ eV})^+$	6 Å†
$\left.\frac{d\sigma}{d\omega}\right\|_l \equiv \left.\frac{d\sigma}{d\omega}\right\|_{O-1s}$	0.31 Mbarn *
$\left.\frac{d\sigma}{d\omega}\right\|_k \equiv \left.\frac{d\sigma}{d\omega}\right\|_{Ag-3d}$	2 Mbarn *

$^+$ Values obtained with TPP-2M algorithm [110].
† A 10% uncertainty has been considered.
* Values from [111].

overlayer with energy $E_{\text{kin}} = E_l = E_{O_{1s}}$ have to travel only inside the NiO film. In table 4.1 these values are given.

Numerically solving the model of equation (2.6) the film thickness can be obtained.

In order to calibrate the sample growth a series of NiO film has been realised and the thickness was calculated according to both models proposed above. The result is reported in figure 4.3 were the thickness estimation is given as a function of the nominal (from the quartz-crystal microbalance) value. As shown in the figure a systematic shift between the results from the two model affects the estimation. The simple attenuation model proposed by Lambert-Beer-Bouguer can be easily managed, but unfortunately it requires two different spectra whose acquisition cannot be done in a unique spectrum, so it results affected by the different conditions in which the two measures are performed, e.g. the incident current. This aspect can introduced some systematic errors we are not able to account for, affecting the thickness estimation. On the contrary the more suitable model proposed by Fadley has the difficulty of containing more parameters whose uncertainty contribute to increase error bars in determining thickness value, particularly three inelastic mean free paths that represent the main uncertainty source.

In the light of the results reported in figure 4.3 we used for our experiment the two films marked with an arrow declaring a (15 ± 5) Å-thick NiO film given as the average between the values coming from both the aforementioned

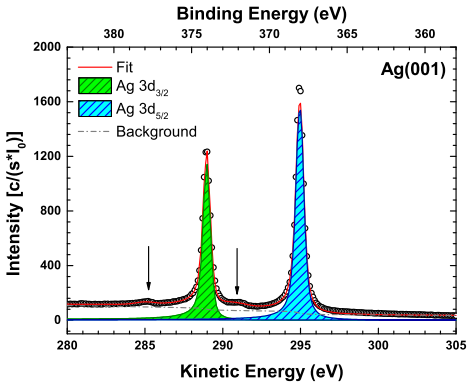

(a) Ag 3d photoemission peaks from the (001) Silver substrate excited with $\hbar\omega = 670$ eV photons: the spin-orbit doublet is follows by two satellites structures due to the energy lost in exciting a crystal plasmon (marked with arrows). Red solid line is a fit of the experimental data.

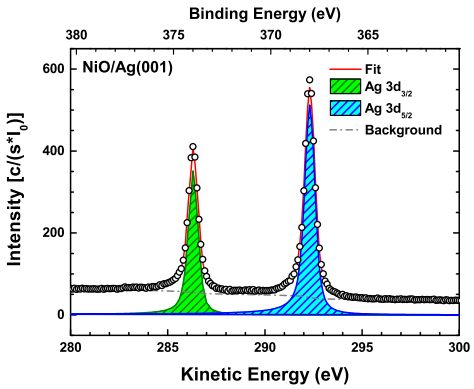

(b) Ag 3d photoemission peaks from NiO/Ag(001) thin film. The primary excitation energy is $\hbar\omega = 670$ eV. Red solid line is a fit of the experimental spectrum.

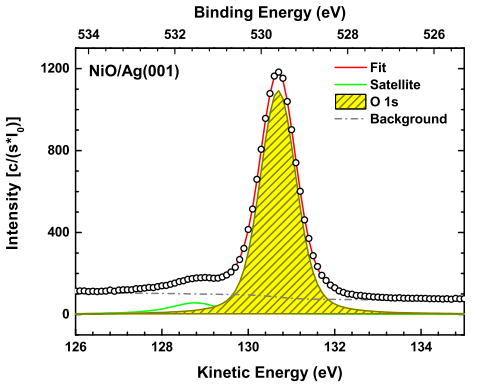

(c) O 1s-photoline from NiO/Ag(001) thin film excited with primary photons of $\hbar\omega = 670$ eV. The main line is followed by a satellite peak due to impurities which intensity was not considered in the thickness determination. Fitting result is given as the red solid line.

Figure 4.2: Photoemission peaks used in determining the film thickness.

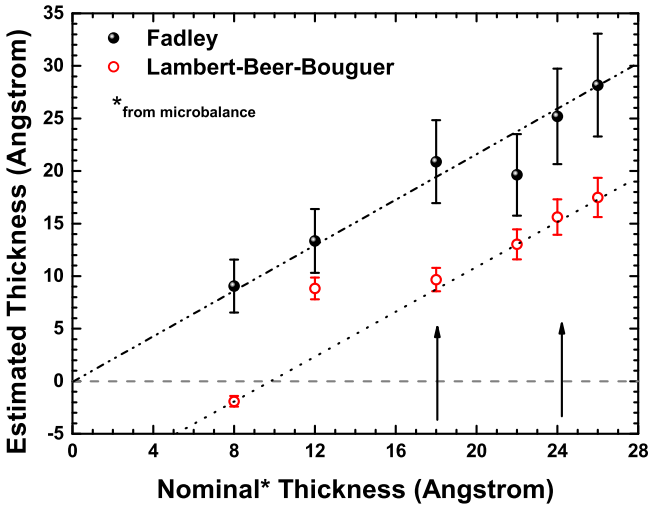

Figure 4.3: Thickness estimation for NiO thin films. Estimation based on the photoemission line intensity is reported as a function of the nominal (from the quartz-crystal microbalance) value. Both the (2.5) and (2.6) models have been used. NiO films measured in coincidence are marked with an arrow. A 15 ± 5 Åthickness was considered obtained by the average between the values coming from both the models with an uncertainty given by the dispersion of the estimated values.

models and its uncertainty as the dispersion of the reported values.

4.1.3 Magnetic phase transition

NiO/Ag(001) thin film has been magnetically characterised using the magnetic-origin dichroism signal in X-ray absorption of linearly polarised photons arising from the Ni-L_2 edge. Measurements have been realised in the conventionally called p polarisation reported in figure 4.4, i.e. with the electric vector of the impinging photons perpendicular to the film magnetisation vector, which lyies, for this range of thicknesses, in the surface [112, 113]. X-ray magnetic linear dichroism (XMLD) at the Ni-$L_{2,3}$ edge has been used to determine the magnetic structure as a function of the temperature in NiO grown on different substrates [51, 113, 114, 115]. It has been shown by Alders *et al.* [51] that the intensity of the absorption spectra components is related to the sample magnetisation, i.e. to its magnetic state. In the same work and lately by Altieri *et al.* [113], has been proven that the magnetic phase change can be detected using the temperature dependence of the intensity ratio of the main components of the Ni-L_2 absorption edge measured with linearly polrised light with polarisation perpendicular to the main spin projection. Hence collecting X-ray absorption spectra (XAS) as a function of the temperature of the specimen, in the geometry represented in figure 4.4, the behavior of the magnetisation can be monitored, as well as the magnetic phase transition. Such an approach is therefore valid to measure the value of the Néel temperature of our film.

The absorption of the systems was evaluated using the "partial electron yield" method. In such a technique the number of the Auger electrons, emitted from the decay of the core-hole created in a specific level ($2p$ in this case) upon the photon absorption, is reported as a function of the photon energy. The number of emitted Auger electrons is proportional to the number of decaying-holes which in turn is proportional to the number of photo-absorption events, hence the absorption spectrum is obtained. For our measurement an energy uncertainty of $\Delta E \simeq 0.02 * \hbar\omega$ comes mainly from the monochromator.

We collected Ni-L_2 absorption spectra from NiO/Ag(001) as a function of the sample's temperature. As reported in figure 4.5a Ni-L_2 absorption edge, involving electron transitions from $2p^6 3d^8$ configuration towards $2p^5 3d^9$ final states, shows itself as a doublet and this is an effect of the octahedral distorsion of the NiO [51] that can be ascribed to the strain induced by the lattice mismatch with the substrate. As reported in literature the Ni-L_2 absorption edge from NiO samples is properly reproduced using atomic-multiplet based models [115, 116, 117] in terms of the $^3A_2$ ($t^3_{2g\uparrow} e^2_{g\uparrow} t^3_{2g\downarrow}$), multiplet term

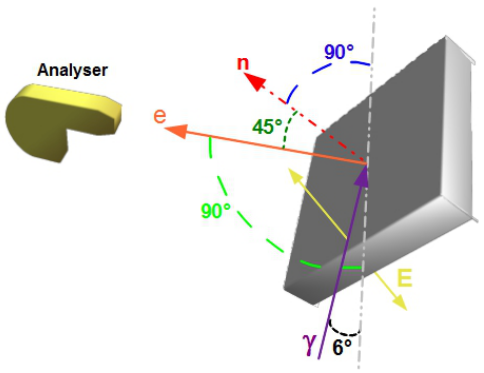

Figure 4.4: Schematic representation of the experimental geometry in XAS measurements. Auger electron emitted upon photon absorption are collected 45° apart from the surface normal. Linearly polarised photons are impinging at grazing angle of 6° with the electric vector normal to the sample surface, where the magnetic moments are lying, in the so called *p*-polarisation.

of the Ni^{2+}, ($3d^8$) configuration, ion. Calculations have shown that the difference in intensity of the two main components (peaks A and B in figure 4.5a) is induced by exchange interaction, as shown in the inset of figure 4.5b. This means that differences in intensity are expected upon changing the sample's temperature because they reflect the temperature dependence of the exchange interaction, see figure 4.6. Hence following the temperature evolution of the intensity ratio for these two components we have access to the temperature dependence of the magnetic interaction. The temperature dependence of the intensity redistribution was investigated reporting the intensity ratio of the two main peaks, $R_{L2} = \frac{I(peakA)}{I(peakB)}$, as a function of the temperature. To do this the prototypical deconvolution shown in figure 4.5a was applied to all the spectra collected at different temperatures. In doing so no relative energy shift among the different Voigt components has been allowed and also their widths have been taken fix, letting only the intensities free of varying. In table 4.2 parameters used in the fitting procedure for the two main components are reported. This deconvolution mainly reflects the model of the $^3A_2$ multiplet contribution with an exception for the low-energy component ($\sim$ 870 eV) not accounted for in the atomic-multiplet approach. Peak intensity ratio for our 15 Å-thick NiO/Ag(001) film is reported as a function of the temperature in figure 4.7. Two different behaviours can be

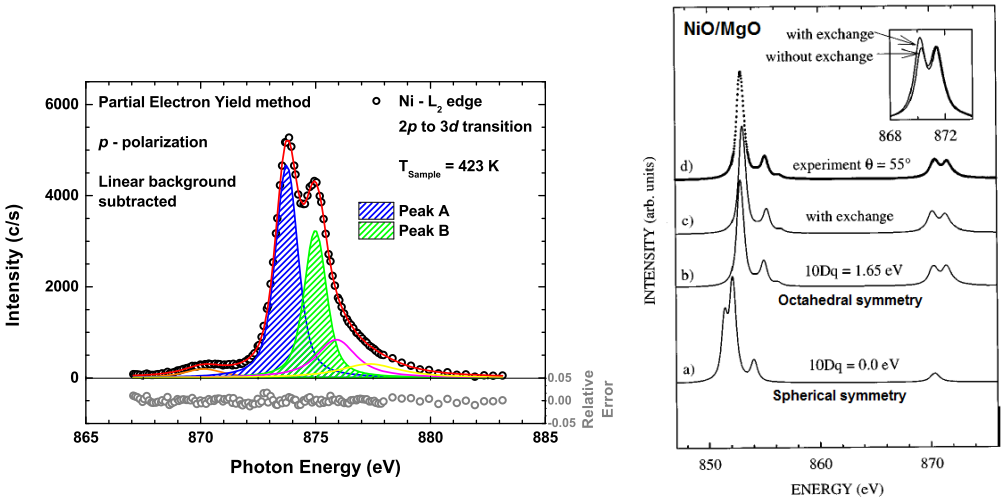

(a) (b)

Figure 4.5: Ni-L_2 absorption spectrum from NiO in X-ray absorption spectroscopy: in panel (a) Ni-L_2 absorption edge from NiO/Ag(001) collected using the partial electron yield method. The spectrum has been collected at a temperature of 423 K in the so called *p*-polarisation geometry. A linear background has been subtracted in the same spirit of ref. [118]. A deconvolution of the absorption edge made with five Voigt curves is also present: the two main components used in evaluating the magnetic linear dichroism are marked as shadow areas. The red solid line is the fitting result. See also table 4.2. In panel (b) Ni-$L_{2,3}$ absorption edge from NiO/MgO(001). The isotropic spectrum was calculated for a Ni^{2+} ion in spherical symmetry (calculated spectrum labelled as (a)) and in octahedral symmetry (calculated spectra labelled as (b) and (c)). While in (c) an exchange field was considered on the contrary in (b) exchange interaction was neglected. Exchange field influence is better highlighted in the inset. A Lorentzian lifetime broadening has been included. The experimental isotropic spectrum from a 20 monolayer NiO/MgO(001) at $T = 298$ K is also reported (experimental spectrum labelled as (d)). Figure adapted from [51].

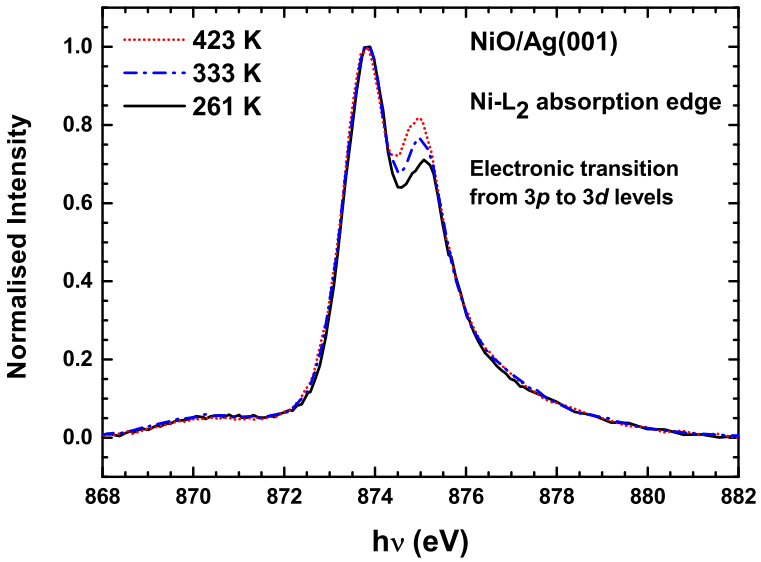

Figure 4.6: Ni-L_2 absorption edge for a 15 Å-thick NiO/Ag(001) film in XAS collected at three different sample's temperature: $T = 423$, 333, 261 K. Spectra, after a linear background subtraction, have been normalised to unity at the low-energy peak to show the redistribution of intensity for the main components of the edge as a function of the temperature.

Table 4.2: Parameters used in the Ni-L_2 absorption edge deconvolution.

Component	Energy position (eV)	Gaussian Width (eV)	Lorentian Width† (eV)
Peak A	873.74	0.80	0.59
Peak B	874.98	0.80	0.49

† The difference in Lorentian width between the two main components could be interpreted in terms of the multiplet contribution from the $^3A_2$ term of Ni^{2+} ion which foresees two components very closed in energy for the 873 eV peak (not resolved here) while a single contribution for the 875 eV peak [116].

found in the temperature range sampled, which extend from 233 K up to 433 K: from 233 K the intensity ratio decreases, near linearly, from 1.45 down to 1.18 reached around $T = 380$ K and than it remains constant. It is possible to interpret these different behaviors in terms of the magnetic order of the system. As mentioned before the exchange interaction is responsible for the different intensity shown by the two main components of the absorption edge, see inset of figure 4.5b and ref. [51]. This means that the intensity ratio has to be affected by the temperature dependence of the spin-spin interaction, particularly the magnetic linear dichroism signal in XAS (XMLD) results proportional to the mean value of the square of the magnetisation , $\langle M^2 \rangle$. Hence, when the sample goes from a high-ordered towards a low-ordered antiferromagnetic phase, i.e. approaching the Néel temperature from below, the reduction in magnetisation manifest itself as a lower intensity ratio, in agreement with [51]. Once the Néel temperature is exceeded the long-range order is lost and the system enters in a paramagnetic phase. In this condition the magnetisation in each domain is randomly oriented so the net magnetisation, as well as its square, results null. Hence above T_N any temperature change is expected to have no effects on the intensity ratio. This allows us to consider our film in its antiferromagnetic phase at any temperature below $T = 380$ K and in a paramagnetic phase above.

To get some physical information, e.g. the transition temperature of the film, a power-law fitting procedure has been applied. The fitting function

$$\begin{cases} A + B\left(1 - \frac{T}{T_N}\right)^c & \text{if} \quad T < T_N \\ A & \text{if} \quad T > T_N \end{cases}$$

used as free parameters the Néel transition temperature T_N, the critical exponent c , the scale factor B and the crystal-field contribution to the linear dichroism[1] represented by A. The result of the fit is reported in figure 4.7

[1]Such a dichroic signal allows to unravel the magnetic contribution to the linear dichro-

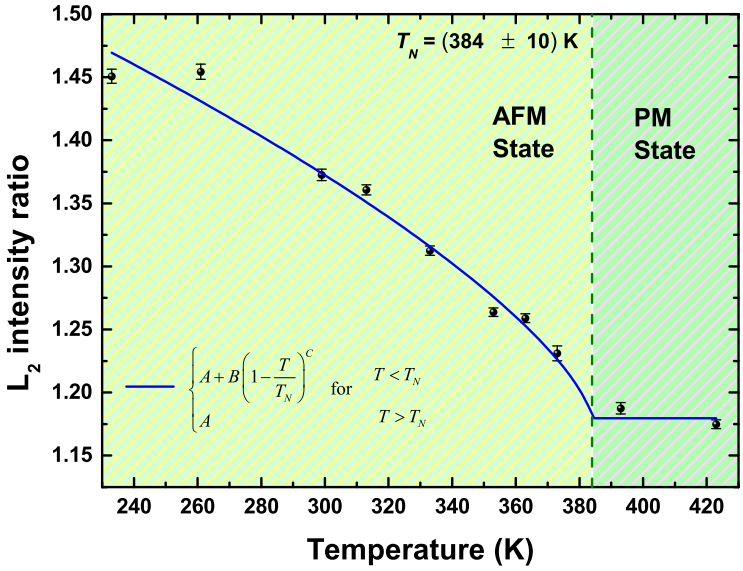

Figure 4.7: In figure the R_{L2} intensity ratio is given as a function of the temperature. An approximately linear reduction of the intensity ratio up to $\sim$ 380 K precedes a constant-ratio region. In the temperature range below 380 K the temperature dependence of the intensity ratio is addressed to the reduction in magnetic order of the system, hence the constant behavior above that temperature is an hint for the lost of long-range order. In this way the magnetic transition from an antiferromagnetic to a paramagnetic state can be followed and the Néel temperature T_N of the film determined. The blue solid line is a power-law fit of the data. The non-zero value of the dichroism above T_N is due to the crystal field.

as the blue solid line. Peak-intensity ratio reduction is quite linear as highlighted by an exponent of 0.69 ± 0.14 up to the reaching of a steady value above the Néel temperature, as expected for such a system [52]. The critical exponent, characteristic for the universality class which the system belongs, is compatible (within its uncertainty) with a surface 3D Ising behavior as in the case of an antiferromagnetic FeF_2 (0.80 ± 0.04) by Lederman *et al.* [119]. As mentioned before and discussed in ref. [51] when the spin-spin interaction has no effects on the system (as in its paramagnetic phase) the same intensity for the two main components of the Ni-L_2 absorption edge must be expected. Hence an intensity ratio equal to unity is to be found above the transition temperature. This is true if only the magnetic dichroism is taken into account, but on the contrary the strain induced by the lattice mismatch between the silver substrate and the NiO film introduces another source of dichroism. The crystal-field contribution, which has been taken into account via the A coefficient in the fitting function, has been evaluated to be $A = 1.18 \pm 0.01$. The goal for these absorption measurements was to get the Néel transition temperature and according to this fit a transition temperature of $T_N = (384 \pm 10)$ K has been obtained.

4.1.4 AR-APECS from NiO below and above the transition temperature

AR-APECS spectra on NiO/Ag(001) films have been measured once above ($T_{\text{Sample}} = 420$ K) and once below ($T_{\text{Sample}} = 300$ K) the Néel temperature of the film ($T_N = 384$ K), hence probing the sample in both its magnetic phases (paramagnetic and antiferromagnetic). Experimental geometry is reported in more details in section 3.5 and only a brief summary will be given here. Monochromatic photons of 250 eV, linearly polarised, impinged on the sample with a 6° grazing-angle. Such an energy excite the Ni $3p$ core level photoelectrons and allows to obtain Auger electrons in a spectral region were no superposition with others core feature is present. This shrewdness allows to reduce the accidental coincidence background in the time spectra. The sample was positioned with its normal lying in the plane defined by the electric vector, $\vec{\varepsilon}$, and the wave-vector, $\vec{k}$, of the light. The axes of the five axial analysers are lying in the same plane. These analysers, one aligned with $\vec{\varepsilon}$, two $\pm 18°$ apart and two more $\pm 36°$ apart from it, were used to collect Ni $3p$ core level photoelectron within an energy window of 4.3 eV, fixed by the energy resolution of the analysers, in order to acquire the entire Ni $3p$

ism (temperature dependent) with respect to the crystal field one (temperature independent).

main peak. The bimodal analyser were used to collect the whole $M_{23}M_{45}M_{45}$ Auger spectrum of the Ni analysing the kinetic energy via a microchannel plate based multichannel analyser. Auger electrons were collected in a plane perpendicular to the one containing the photon propagation vector and the light polarisation at an angle of 38° with respect to $\vec{\varepsilon}$.

In such a geometry the three axial analysers positioned within 20° with respect to $\vec{\varepsilon}$ collect photoelectrons with a dominant contribution from partial waves with $m = 0$, while the two outermost collect a sizeable amount of $m = \pm 1$, see figure 2.7 on page 67. In the same manner the bimodal analyser collects Auger electrons showing a dominant contribution of $|m| > 0$. In the following we will define as aligned (A) those analysers collecting dominant contribution from $m = 0$ and not-aligned (N) the others collecting $|m| > 0$. Therefore, the kinematic conditions reported in table 3.3 on page 107 are possible.

In such a 1-photon in $\rightarrow$ 2-electrons out process several combinations of photoelectrons and Auger electrons magnetic quantum numbers combine giving rise to spin multiplets. Exploiting the photoemission and Auger emission selection rules and properly choosing the experimental geometry it is possible to weight in a different way the several m contributions thus achieving the spin selectivity discussed in section 2.3.2.

In figure 4.8 AR-APECS spectra for a 15 Å-thick NiO/Ag(001) film are reported. In panel (a) the MVV partial Auger yield in coincidence with the Ni $3p$ photoelectrons collected at different ejection angle have been taken at low temperature, hence with the NiO in an antiferromagnetic state, while in panel (b) the same transition has been measured at a temperature of 420 K, higher than the Néel transition value. The spectra are shown as true coincidence counts versus kinetic energy of the Auger electrons. The spectrum with red open circles and error bars is referred to the NN geometry while the one with green open triangles and error bars to the AN geometry. Roughly the spectra are characterised by an onset around 59 eV showing a broad main line centred at 49 eV of kinetic energy. A measurable dichroism between the AN an the NN geometries is present in the AR-APECS spectra collected at room temperature. This dichroism completely disappears, within the error bars due to the achieved statistics, once the Néel temperature is exceeded. A similar behaviour has been observed in the antiferromagnetic CoO/Ag(001) [37, 120]. Also in this latter system the dichroism in AR-APECS spectra shown below the Néel temperature completely disappear once the transition temperature is exceeded. Thus such a behaviour seems to be not an isolated case of the CoO but a more general aspect associated to antiferromagnets and it requires a proper interpretation.

The large dichroism shown at room temperature (below T_N) makes possi-

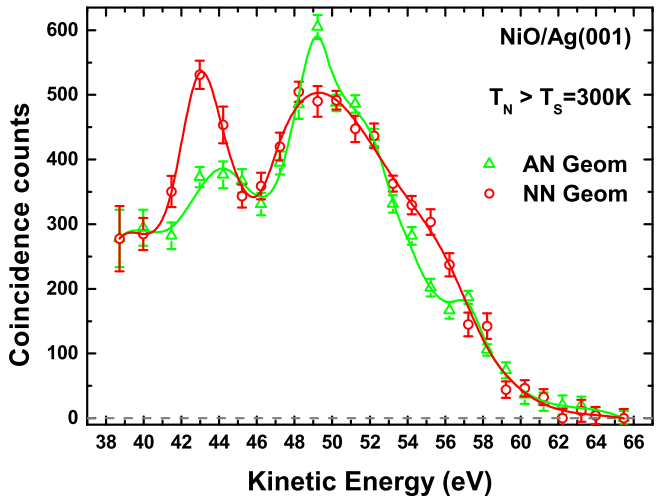

(a) AR-APECS spectra from a 15 Å-thick film of NiO/Ag(001) at room temperature ($T = 300$ K).

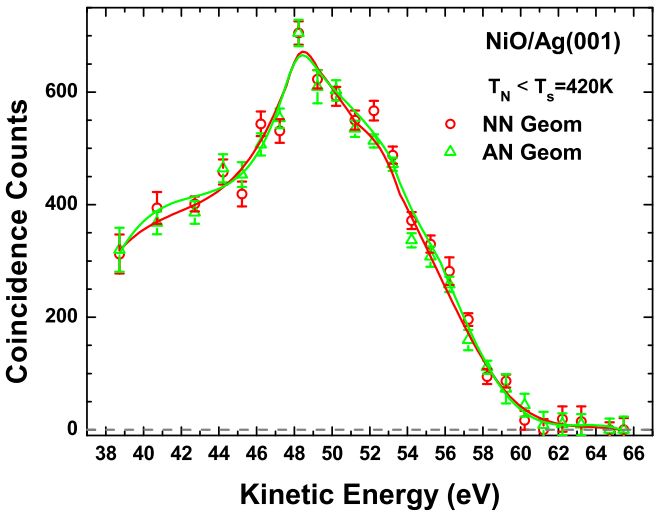

(b) AR-APECS spectra from a 15 Å-thick film of NiO/Ag(001) at a temperature of $T = 420$ K.

Figure 4.8: AR-APECS spectra from NiO/Ag(001) 15 Å-thick film: two different kinematics has been collected. The partial Auger yield of the $M_{2,3}M_{4,5}M_{4,5}$ transition in coincidence with Ni $3p$ core level photoelectrons is reporte as true coincidence events versus kinetic energy of the Auger electrons. Spectra from AN geometry and NN geometry (realised according to table 3.3 on 107) are reported as green open triangles and red open circles respectively. Solid lines are guides to eye.

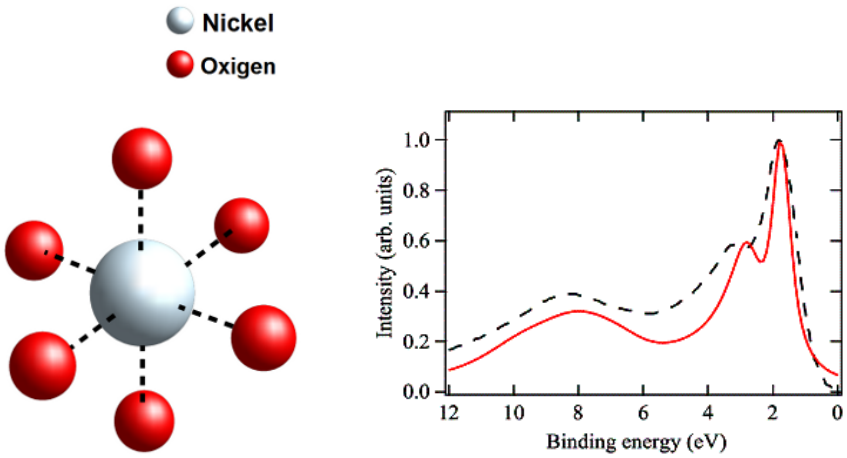

(a) The octahedral NiO_6 cluster used to represent the AFM NiO system.

(b) Comparison of experimental (red dashed line) and calculated 0.8 Ni + 0.2 O (black solid line) valence band photoemission spectra. Experimental spectrum from ref. [121].

Figure 4.9: Modeling NiO system.

ble to distinguish several atomic-like multiplet terms and in order to correctly assign spin values to each term a theoretical model developed by M. Cini and briefly described in the following[2] has been applied.

To describe the band state an octahedral NiO_6 cluster centered in the Ni^+ ion was parametrised for NiO. The hybridisation between the $2p$ level of the ligand oxigen and the $3d$ valence level of the metal has been included along with the $d-d$ Coulomb repulsion among the Ni d-holes. The cluster has been parametrised by comparing the calculated single-particle local density of states (LDOS) with an experimental XPS spectrum following an approach similar to those proposed by Fujimori and Minami [121] and by Zaanen *et al.* [122] but computing 2,3,4-hole spectra of the cluster. In figure 4.9b the calculated LDOS for a 2-holes ground state cluster (d^8 configuration) is shown as a solid line, while the dashed line is the experimental NiO valence band photoemission spectrum by Kowalczyk *et al.* as reported in [121]. According to the Hund's rule the d^8 ground state was taken to belong to maximum spin $S=1$. The relative intensity and position of the three main peaks are very sensitive to the free parameters of the model and the good agreement shown in figure 4.9b guarantees a good cluster parametrisation. After choosing the parameters that best reproduce the XPS spectrum of NiO, Auger spectrum is calculated with no adjustable parameters. A 1 eV lorentian broadening was

[2] A complete description in [105].

convoluted with the calculated Auger spectra in order to simulate lifetime and other broadening effects.

The NiO_6 cluster hosts four holes after the Auger decay (the ground state is a d^8 configuration, hence it hosts two valence holes and two more holes are created in the creation/annihilation of the core hole via the photoemission and the Auger decay). Combining their four spin Singlet, Triplet and Quintet multiplet contribution must be accounted in the model. Calculated spin-resolved Auger spectrum (the full configuration interaction problem is made up by 210 quintets, 990 triplets and 825 singlets) is compared in figure 4.10 with the experimental spectrum. Features in the AN geometry result well accounted by Triplet and Quintet contributions: the main peak at 50 eV find correspondence in the absolute maximum of the Triplet (marked by E), while the shoulder at 52 eV can be attributed to the spectral contribution of the Quintet (maximum and shoulder marked by D). The relative maximum between 44 and 46 eV corresponds to the relative maximum (labelled as H) in the Triplet contribution, while the maximum around $57 - 58$ eV can be interpreted in terms of the high energy relative maximum of both Triplet (B) and Quintet (A) contributions. About the features in the NN geometry a sizeable contribution from the singlet, at expenses of spectral intensity from quintet and triplet, is present: the broad main peak around 49 eV can be interpreted considering only the triplet and the singlet maxima (marked as E and F respectively) while the two distinct features at 43 eV and 55 eV correspond to the relative maxima (I and C) of the singlet term. As in the case of CoO [37, 120], once the theoretical and experimental spectra are aligned on the energy scale, a good agreement for the whole pattern of peaks is achieved as underlined by the correspondence of the maxima of the theoretical curves and the feature in the difference plot. The relative difference in the spectral region between 40 and 45 eV, where the I and H maxima are falling, as well as between 53 and 57 eV, where the C and B maxima are located, reaches 20%.

In order to highlight the theoretical shape of the Auger spectrum coming from this model and to compare it with the experimental one a fitting procedure has been applied separately for both geometries. The three theoretical curves (Singlet, Triplet and Quintet) have been used as components of the fitting function. The relative energy position has been kept fixed as from the theoretical model. Also the lineshape of each theoretical component suffered no distortions. The energy position of the whole pattern has been left free of varying in order to get the proper allignement between theoretical curves and experimental spectra. Spectral intensity of each multiplet term has been used as fitting parameter. An integral background has been added. About this latter, in building the trial function, the background is obtained integrat-

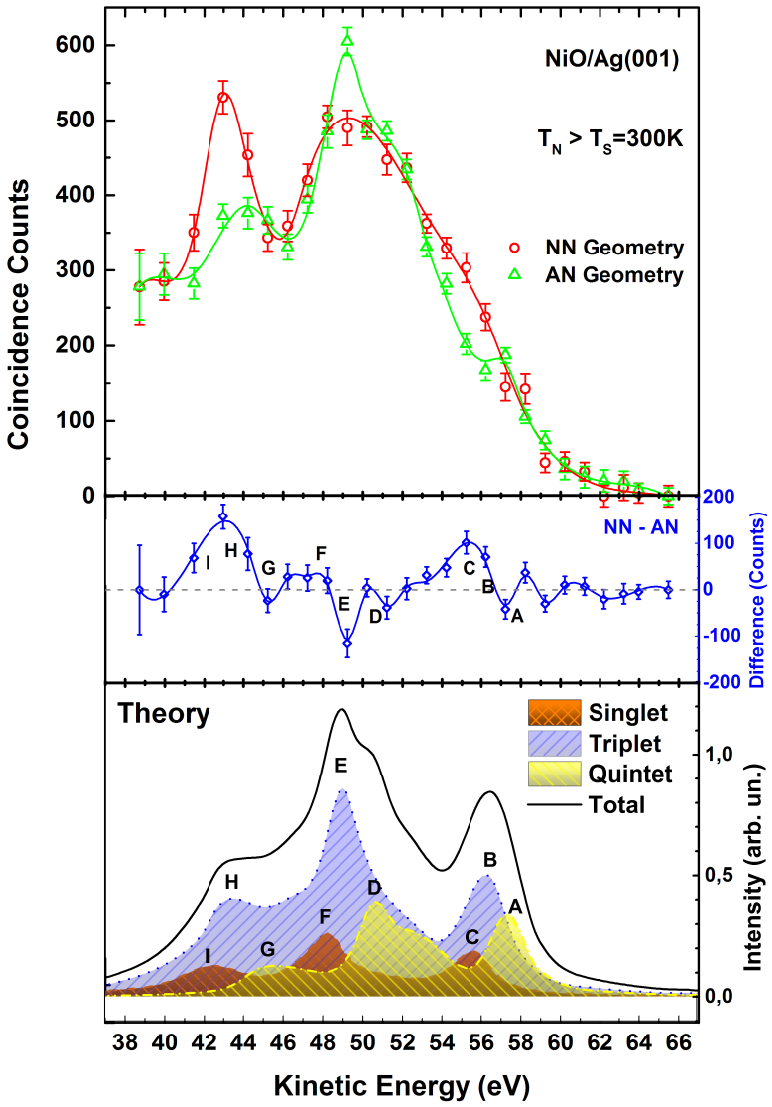

Figure 4.10: Comparison between the spin-resolved calculated Auger spectrum and the experimental one collected for NiO/Ag(001) 15 Å-thick film at room temperature. In the upper panel the experimental spectrum is reported: AN geometry is given as green open triangles with error bars, while NN geometry as red open circles with error bars. Solid lines are guides to eye. In the central panel the difference between the spectra collected in the two geometries is given as blue open diamonds. In the lower panel the theoretical spectrum is shown. Multiplet spin contribution are given as follow: Singlet ($S = 0$) as the dashed profile with orange shadow area, Triplet ($S = 1$) as the dotted profile with light blue shadow area and Quintet ($S = 2$) as the dash-dotted profile with light yellow shadow area. Capitol letters assigned to the main features of the theoretical curves have been reported on the plot of the difference for an easier comparison.

ing the experimental spectrum, then its offset (the value at the high kinetic energy side of the spectrum) and its slope (which affects the height-difference between the high- and low-energy side) are processed as fitting parameters togheter with the others aforementioned for the multiplet contributions. In this way we are trying to describe the experimental spectrum as linear combination of Singlet, Triplet and Quintet terms piled up the background. In figure 4.11 the result of the fitting procedure is shown: the best reproduction of the experimental spectrum, on the basis of the fitting function discussed, is reported for both the AN (upper panel) and NN (lower panel) geometries. As discussed describing figure 4.10 there is a good agreement between the whole pattern of multiplet terms arising from this cluster model and the features in the experimental spectra and such an aspect is confirmed by the fitting procedure. Anyway the comparison reveals a certain discrepancy which affects significantly the spectral region from the onset up to the main peak. The lack of spectral intensity seems related to a low Quintet contribution in both the lineshapes. The impossibility to enhance the Quintet contribution is mainly due to the large spectral intensity with respect to the main peak of the high kinetic energy feature shown by both Triplet (peak B) and the Quintet (peak A). The enhancement of Quintet contribution to recover spectral intensity between 50 and 55 eV will lead to an overestimation on the high kinetic energy spectral region. This behaviour seems to characterise the comparison in both the geometries. In the light of this result the model proposed seems to overestimate the high kinetic energy spectral weight of the multiplet terms described. Anyway using these fits it is possible to put on a more quantitave ground the fact that AN curve is mainly a combination of Triplet and Quintet (from this analysis the Singlet contribution results completely suppressed) while NN curve is mainly Triplet and Singlet, and the main difference upon changing kinematics from AN to NN is an increase of Singlet at expenses of Triplet. Hence this approach highlights what we expressed in section 2.3.2: AN geometry results more "high-spin" (Quintet and Triplet) sensitive with respect to the NN one which is more "low-spin" (Singlet) sensitive.

As for CoO also for NiO spin contributions are energy shifted according to the Hund's rule: the Singlet falls at the low kinetic energy side of the spectrum (higher binding energies), the Quintet is in the opposite region an the Triplet in between. In this case anyway the analysis is more difficult because while for CoO different spin contributions are more separated and different in shape one from the other, in NiO such differences are not as sharp.

What happens to AR-APECS spectra in NiO crossing the Néel temperature T_N is quite similar to what was observed for CoO: while below the

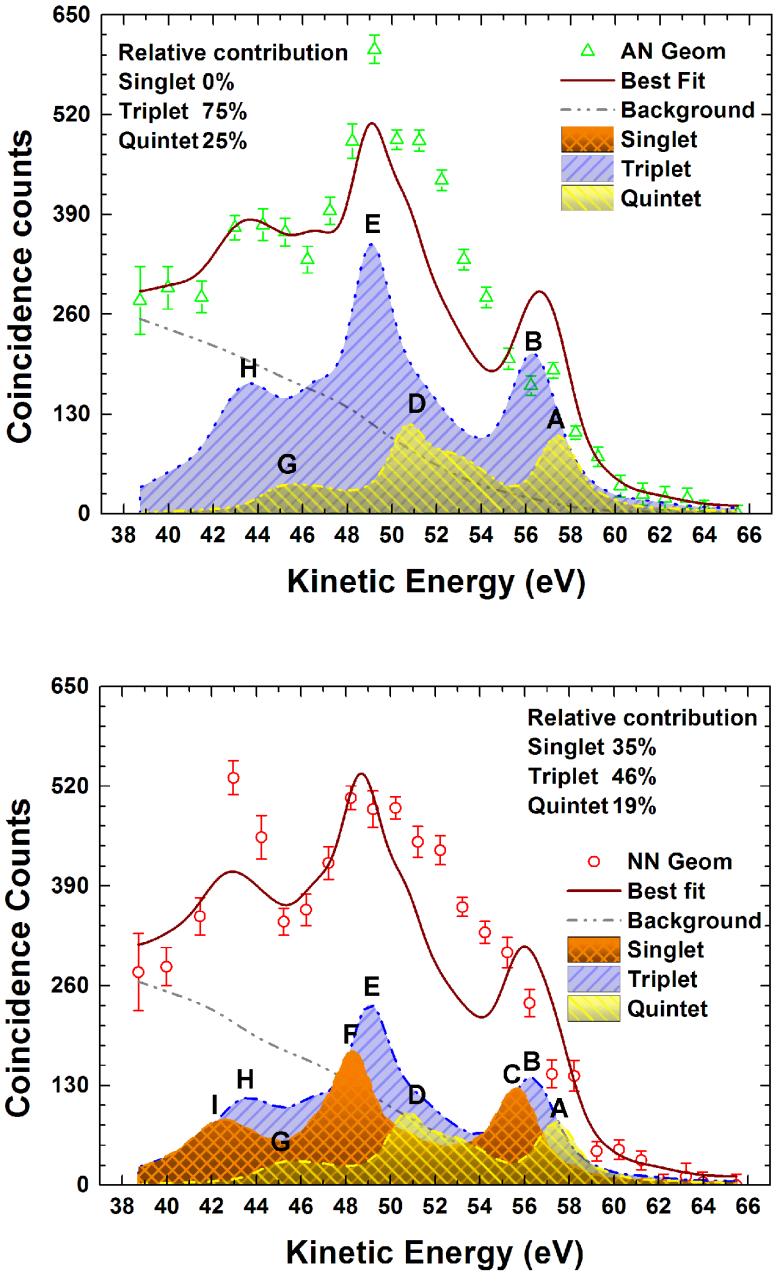

Figure 4.11: Comparison between experimental and theoretical lineshape for AR-APECS spectra of NiO. In the upper panel is shown the AN geometry while in the lower panel the NN one. Solid line is the best fit of the spectra (see text for more detailes). The relative contribution of the three (S, T, Q) terms is also reported. Capitol letters assigned to the main features of the theoretical curves have been reported on the plot according to previous definition to help the reader.

magnetic phase transition temperature a dichroic effect in AR-APECS spectra is present, a complete collapse of such an effect is observed crossing T_N. High temperature spectra show themselves as broader and featureless with respect to the others collected at room temperature, but they cannot be interpreted in terms of a different degree in electron correlation. This because the Cini-Sawatzky theory [31, 32] foresees a redistribution of spectral intensity towards the Fermi level (higher kinetic energies) going from atomic-like to band-like behaviour, that in our measurements has not been observed.

Following the interpretation given for CoO [37, 120], the disappearance of any dichroism can be assigned to two different mechanisms:

1. changes in screening channels;

2. presence of magnetic moments affecting the APECS matrix elements.

In a sequential two-step model framework in the double ionisation process due to a single photon absorption three vectors with kinematic relevance must be considered: the direction of the two emitted electrons (photoelectron $\hat{\mathbf{n}}_\mathbf{1} = (\theta_1, \phi_1)$ and Auger electron $\hat{\mathbf{n}}_\mathbf{2} = (\theta_2, \phi_2)$) and the direction of the target polarisation $\hat{\mathbf{a}}$, which is in our case the sample's magnetisation M. The APECS cross-section calculated for an isolated polarised (magnetic) atomic target is then affected by these vectors and reads [123]:

$$\begin{aligned} \frac{d^3\sigma}{d\Omega_1 d\Omega_2 dE_1} &= \frac{\pi\alpha\omega}{\Gamma/2\pi} \sum_{k_r k_0 k_\gamma k_1 k_2} \hat{J}_1^{-1} \bar{\rho}_{k_0 0}(\alpha_0 J_0) B^{k_1 k_2}_{k_0 k_r k_\gamma}(J_0, J_1) \times \\ &\times A_{k_2}(J_1, J_2) F^{k_1 k_2}_{k_0 k_r k_\gamma}. \end{aligned} \tag{4.1}$$

Here in equation (4.1) α is the fine-structure constant, ω the photon energy, Γ the total width of the intermediate state with angular momentum J_1, $\hat{J} \equiv \sqrt{2J+1}$ and E_1 the photoelectron energy. $F^{k_1 k_2}_{k_0 k_r k_\gamma}$ represents a kinematic factor which depends on the photon polarisation and the collection angles of the ejected electrons, while $B^{k_1 k_2}_{k_0 k_r k_\gamma}(J_0, J_1)$ describes the photoionisation process and $A_{k_2}(J_1, J_2)$ the Auger decay of the core-hole. $\bar{\rho}_{k_0 0}(\alpha_0 J_0)$ defines the polarisation state. The complete collapse of the dichroism in AR-APECS spectra shown in figure 4.8 upon crossing the Néel temperature can be interpreted in terms of a dramatic change in the cross-section. The loss of long-range magnetic order upon exceeding the Néel temperature is not enough to justify such a change. As proposed by Altieri *et al.* [113], the stabilisation of magnetic domains in $3d$ systems is influenced by lattice strain. As mentioned before our films are characterised by a magnetisation within the surface plane. Because exceeding the transition temperature no changes in the tetragonal strain affecting the NiO film are expected, even if

randomised, the magnetisation still lies on the surface plane. On the contrary the two unbound electrons are still collected at fixed angles in a plane perpendicular to the surface. Thus the AR-APECS cross-section results not averaged over all the possible relative directions of the relevant vectors and a dichroic effect is still expected. Hence the loss of any dichroism in AR-APECS spectra would be related to the loss of one of the three kinematic vectors. The emitted electrons were collected in the same geometries above and below the transition temperature, hence no changes in their momenta must be expected and because the only difference in the two measures is the sample's temperature, that means a different magnetic phase, the loss of the third vector, the magnetisation, must be considered. Hence exceeding the transition temperature the loss of short-range magnetic order occurs.

It is therefore possible to attribute such collapse of the spin-selectivity to the electron-screening channel because NiO is an open d-shell system and electrons of neighboring atoms screen the core-hole. The capability of electrons with a proper spin to participate in the screening process can be affected by the magnetic correlation between adjacent atoms, as in the case of ferromagnetic systems were a spin-dependent screening has been observed [124]. This means that the temperature, i.e. the magnetic phase, affects the screening mechanism.

4.2 Investigation of electron correlation in Ferromagnetic thin films, the cases of Ni and Fe

In this section the experiments performed on two ferromagnetic systems, Fe and Ni, are presented. We measured the $M_{23}VV$ Auger electrons in time coincidence with the $3p$-photoelectrons emitted, again, upon the absorption of linearly polarised light. We probed this Auger transition collecting the photoelectrons and Auger electrons in both the kinematic conditions presented before. As expected satellites structures whose origin must be searched in electron correlation have been enhanced.

The AR-APECS spectra have been measured on the Fe film below the Curie temperature in order to probe the metallic layer in its ferromagnetic alignment, while for Ni the measures have been collected upon crossing the magnetic transition changing both the temperature and the thickness, i.e. performing the experiment both below and above the Curie point for a specific film thickness and probing, at the same temperature, two films with different thickness, and consequently different Curie temperatures. While

the main line of the $M_{23}M_{45}M_{45}$ Auger transition shows a little dichroism with the system in its ferromagnetic state, it result affected by no differences in the two kinematics for the paramagnetic phase, but the main dichroic contribution upon changing the kinematics remains a low kinetic energy feature.

4.2.1 Experimental

In these experiments we performed AR-APECS measurements on Ni and Fe thin films grown onto a non magnetic substrate. Our choice for substrates falls on Cu for the Ni film because it allows for a good pseudomorphic growth mode (in register with the substrate) due to the same fcc crystal symmetry and a reduced lattice mismatch less than 2.5% responsible for a tetragonal distortion [125, 126]. For the Fe film an Ag substrate was selected not only for the reduced lattice mismatch (the Ag lattice cell, $a_{Ag} = 4.09$ Å, is $\sqrt{2}$-times longer than that of the bulk Fe) which guarantees a pseudomorphic growth with the cell rotated 45° with respect to the substrate [127], but also because such a choice allows for a comparison with the case of Fe/Cu(001) [104] and with the Fe/CoO/Ag(001), presented in the following of this thesis, in order to highlight substrate effects if any. As for NiO, also Ni and Fe ultrathin films have been grown *in situ* by means of electron bombardment of high purity rods of the corresponding metals. Cycles of Ar^+-ion sputtering have been used to clean the surface of respective substrates, resulting in x-ray photoemission spectra free of carbon and oxygen. Ni has been deposited onto the clean and crystallographically well ordered (001) surface of a Cu single crystal, while the Fe layer has been grown onto the clean and well ordered Ag(001) surface. In both cases the surface order has been obtained via an annealing of the substrate up to 700 K for Cu and 750 K for Ag. The crystalline structure was monitored using Reflection High Energy Electron Diffraction (RHEED) pattern.

We realised two different films of Ni/Cu(001) with thicknesses of 4 and 6 monolayers (ML). Thickness calibration has been realised using intensity oscillations of the (0,0) spot in electron diffraction (RHEED) which assisted Ni evaporation. The oscillations of the electron diffraction signal are good tool to follow the growth evolution of systems for which a layer-by-layer growth mode is expected [43]. Their interpretation relays on the growth mechanism: when, during the growth, an atomic layer results complete a maximum in the diffraction spot intensity is observed. This because the 2D-periodicity of the topmost layer is nearly ideal and the diffraction process takes place from an array of atoms periodically displaced acting as coherent sources. Going on with the deposition, before completing a new layer having a new maximum in the spot intensity, the topmost layer shows a certain amount of disorder

due to irregularly displaced atoms or to islands. In such a condition the disorder enhances the background intensity (scattering from incoherent sources) at expenses of the coherent diffraction spot intensity, which decreases down to a minimum value reached for a half-filled layer. Then a new increase of the spot intensity leads to the new maximum condition. Hence counting the maxima it is possible to counts the atomic layers. As an example in figure 4.12 RHEED oscillation for the 4 ML-thick Ni/Cu(001) film investigated is reported in panel (a). The mechanism reported just above is also sketched. In order to prevent interdiffusion [128, 129] no annealing after the film growth has been performed.

About the Fe film, again the growth was monitored calibrating the evaporation time using RHEED oscillations. In figure 4.12b such oscillations are shown. A 3 ML Fe film has been grown on a Ag substrate kept at 240 K in order to reduce interdiffusion and Ag surface segregation [130, and ref. therein], and to record RHEED oscillations, clearly visible at a temperature below $T = 300$ K [131]. No post annealing has been performed to prevent intermixing. At the end of the sample preparation photoemission spectra were collected to check the absence of contaminants in both Ni and Fe layers while the surface quality has been checked using RHEED patterns. For a matter of time such patterns have not been recorded in the case of Ni, hence they are shown only for Fe. In figure 4.13 the electron diffraction pattern of a 3 ML-thick Fe film grown onto the Ag(001) surface, in panel (b), is reported beside the Ag substrate one, shown as reference in panel (a). As discussed previously magnetic behaviour in thin films is intimately affected by film thickness, so proper magnetic characterisation is always required. For Ni films the thickness dependence of the Curie transition temperature has been determined by Huang and co-workers using the Magneto-Optic Kerr Effect (MOKE). Such a technique exploits the fact that light scattering from a surface, for a magnetic system, is affected by the magnetisation. Changes in the magnetisation, i.e. in the magnetic state of the system, leads to a variation in polarisation and intensity of the scattered light with respect to the impinging photons. By means of this magneto-optic effect is therefore possible to get informations about the system magnetisation, hence its magnetic phase, giving access to the determination of the Curie point of the system. For a 4 ML Ni/Cu(001) film a $T_C = 280$ K while for a 6 ML-thick a $T_C = 380$ K have been found [132].

Also the magnetisation results affected by the film thickness and Ni/Cu(001) thin films have shown a spin reorientation transition around a critical thickness of $t_c \simeq 7$ ML: for thicknesses below t_c the magnetisation lies in the surface plane, while for values higher of t_c a perpendicular magnetisation component begins to develop [132, 133]. Also for the Fe film in the ultrathin

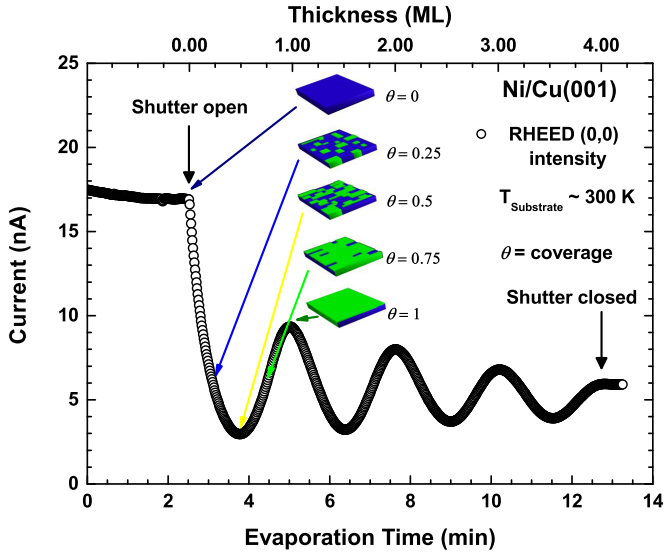

(a) RHEED oscillation for a 4 ML-thick Ni/Cu(001) film. The inset sketches the mechanism discussed in the text.

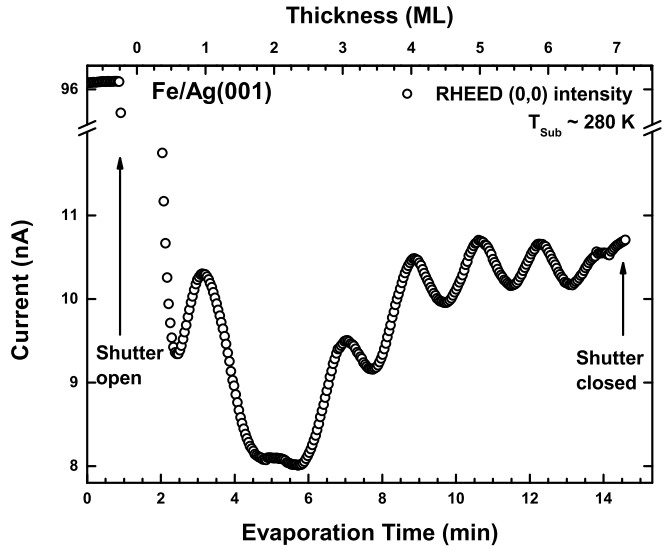

(b) RHEED oscillation from a Fe/Ag(001) thin film: this signal was used to calibrate the evaporation time for the Fe film growth.

Figure 4.12: Oscillation of the RHEED (0,0) spot intensity as a thickness monitor: intensity of the specular reflected spot is collected using a photodiode mounted onto the phosphorus plate of the RHEED apparatus.

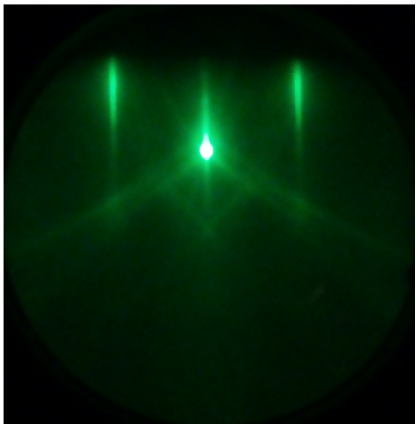

(a) Ag (001) single crystal .

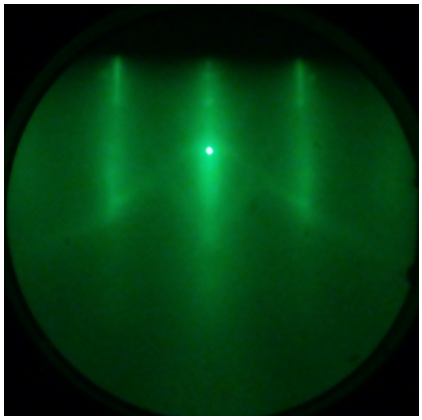

(b) 3 ML-thick Fe/Ag(001) film. The Fe contribution is superimposed to the Ag one, still visible, underlining the 45° rotation of the Fe cubic cell with respect to the one of the Ag substrate.

Figure 4.13: Electron diffraction patterns from Ag and Fe/Ag samples. RHEED patterns have been used to check the surface quality of our samples.

regime the Curie temperature is very close to room temperature or even below it. As reported by Lang and co-workers in [134] for a 3 ML-thick film a $T_C \simeq 300$ K has been expected. The magnetisation behaviour has been investigated by Schaller *et al.* as a function of morphology and roughness, that means both temperature and thickness, in the range between 0 and 10 ML and from room temperature up to ~ 520 K [135]. In such a work a spin reorientation transition has been observed, and for a 3 ML-thick film not annealed, as in our case, the magnetisation has an in-plane main component.

This means that our films, both for Ni and Fe, are characterised by an in-plane magnetisation.

4.2.2 AR-APECS spectra from ferromagnetic Ni/Cu(001) and Fe/Ag(001)

AR-APECS spectra have been collected for both Ni and Fe films. Again we performed these experiments in the same manner of the NiO case proposed before. Impinging photons of $\hbar\omega = 240$ eV and $\hbar\omega = 200$ eV were used to ionise respectively Ni and Fe atoms and the emitted photo- and Auger electrons were collected according to the geometry detailed in section 3.5.

For Fe/Ag(001) spectra of the Super-Coster-Kronig $M_{23}M_{45}M_{45}$ Auger transition, which represents the main decay channel for the $3p$ core-hole, have been collected at a temperature lower than 170 K, probing the Fe layer in a ferromagnetic condition.

AR-APECS spectra of the Fe/Ag(100) are shown in figure 4.14 as true coincidence counts versus kinetic energy of the Auger electrons. The conventional (singles) Auger spectrum is shown as orange dashed line. The spectrum with red open circles is referred to the NN geometry and the one with green open triangles to the AN geometry. Both the two different kinematics show spectra dominated by a main line that falls at 43 eV due to the conventional Auger process

$$3p^6 3d^n \rightarrow (3p^5 3d^n)_{\mathrm{sc}} + e_{\mathrm{ph}} \rightarrow (3p^6 3d^{n-2})_{\mathrm{sc}} + e_{\mathrm{Auger}} \tag{4.2}$$

followed by different features in the low kinetic energy side and with an onset at 49 eV. A measurable difference in AR-APECS spectra is evident. The 36 eV feature that characterises the spectrum collected in the AN geometry could be interpreted as a Cini-Sawatzky resonance of the up-up spin coupling in the same spirit of the interpretation of AR-APECS in Fe/Cu [104]. In this latter work the authors have calculated the individual APECS contributions for all the four configuration of spin coupling ($\uparrow\uparrow, \uparrow\downarrow, \downarrow\uparrow, \downarrow\downarrow$), particularly they found that in order to interpret the low energy resonance, the Cini-Sawatzky

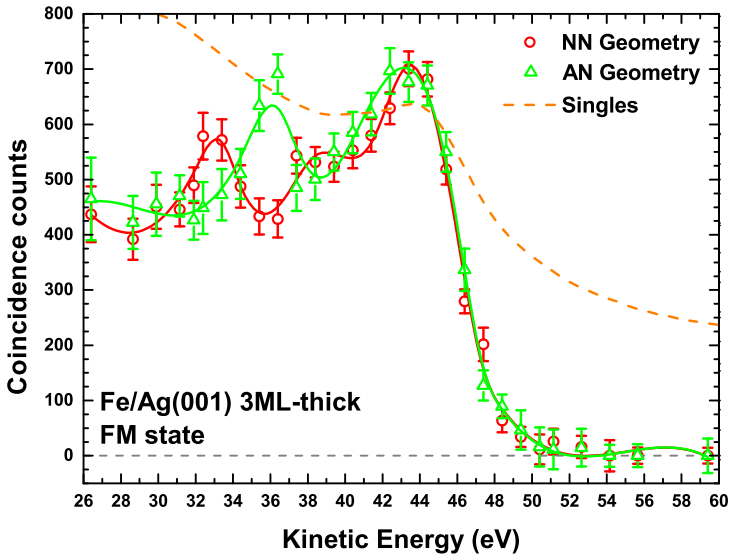

Figure 4.14: AR-APECS spectra for a 3 ML-thick Fe/Ag(001) film for $T < 170$ K: AN geometry, green open triangles, is characterised by a main line due to the conventional Auger transition followed by a distinct feature at lower kinetic energy similar to the Cini-Sawatzky resonance for the up-up ($\uparrow\uparrow$) spin coupling found in [104] for Fe/Cu. The NN geometry, red open circles, shows a main line followed by two secondary features at lower kinetic energies. Conventional (single) Auger spectrum is reported as orange dashed line. The solid lines interpolating the experimental data are guides for eye.

theory, describing the hole-hole interaction, must be considered. The effect observed is a shift toward lower kinetic energies of the ($\uparrow\uparrow$) coupling, involving both electrons from the majority population, revealing the existance of a localised state in the majority valence subband. In the light of this result the majority valence electrons are the more localised, hence subjected to a strong mutual interaction.

About the spectrum collected in the NN geometry, it shows two peaks at 33 and 38 eV not present for the corresponding spectrum from Fe/Cu, whose nature is not known yet.

A possible explanation for this difference could be found in the different crystal structure of Fe, grown on the two different substrates. While Fe presents a bcc configuration upon growing on Ag, Fe on Cu shows, in the early stages of growth, a complex scenario, involving fcc crystal structure

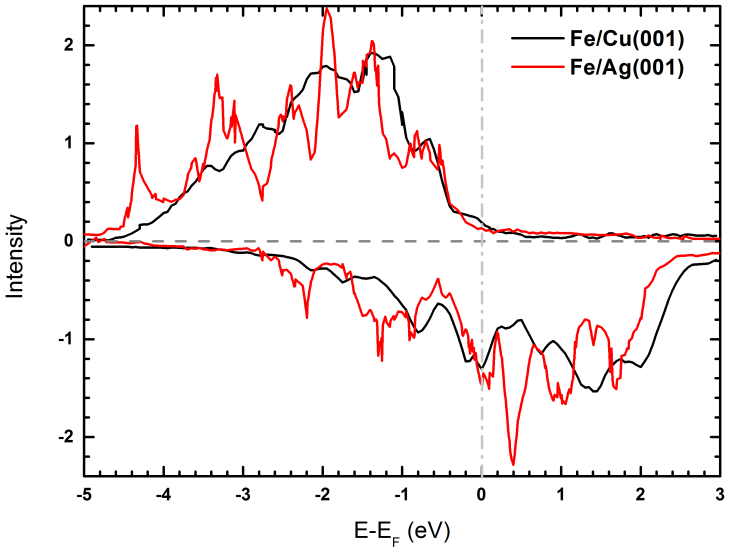

Figure 4.15: Effect of the substrate on the DOS of Fe: DOS for Fe/Cu from Gotter *et al.* [104] while DOS for Fe/Ag is redrawn on the basis of the calculation by Rhee [127, figures 1 and 2] obtained as the sum of the e_g and t_{2g} contributions for the topmost layer of a 3 ML-thick Fe film extracted digitalising the curves from the cited figures.

and tetragonal distortions [136, and reference therein]. The different strain and crystallographic behaviour may be responsible for a different magnetic structure which in turn affects the AR-APECS spectra.

Another possible explanation could be found in a different DOS of the Fe grown onto these two different substrates. In figure 4.15 a comparison between the DOS of Fe/Cu and Fe/Ag is given: DOS for Fe/Cu is reported as in ref. [104], while DOS for Fe/Ag is obtained on the basis of [127, figures 1 and 2], digitalising the curve from the correspondent images and combining the e_g- and t_{2g}-DOS for the topmost layer of a 3 ML-thick Fe film. From the comparison the Fe/Ag DOS seems to be more structured with respect to the one for Fe/Cu and its complexity could be responsible for the features in the NN geometry spectrum cited above. Also the better energy resolution of this last experiment could play a role.

For Ni/Cu(001) the $M_{23}M_{45}M_{45}$ Auger spectrum has been measured both above and below the Curie point crossing the magnetic phase transition upon changing the temperature at fixed thickness and, viceversa, upon changing

the thickness at fixed temperature, as summarised in table 4.3. With this

Thickness (ML)	T_C (K)	T (K) for AR-APECS	Magnetic state
4	280	300	Paramagnetic
4	280	220	Ferromagnetic
6	380	300	Ferromagnetic

Table 4.3: Temperature and thickness values for the Ni specimens probed by APECS

choice of thicknesses the partial Auger yield in coincidence with $3p$ photoelectrons has been collected both with the sample in its paramagnetic and ferromagnetic states.

This Auger transition extends over 30 eV starting from a kinetic energy of 35 eV. It shows an onset at 63 eV of kinetic energy and a main line centered at 57 eV, which corresponds to the same transition expressed in relation (4.2). AR-APECS spectra, reported in figure 4.16, are given as true coincidence spectra as a function of the kinetic energy: AN geometry is reported as dark green open triangles with error bars while NN geometry as the red open circles with error bars. As a comparison the conventional (single) spectrum, simultaneously acquired with respect to the coincidence one, is shown as the orange dashed line. As summarised in table 4.3, we probed three different systems: a Ni/Cu ferromagnetic film at two different thicknesses, 4 and 6 ML, and a 4 ML paramagnetic film. In this way any asymmetry in AR-APECS spectra can be probed in both the magnetic phases of the film. Spectra collected for the ferromagnetic state have shown a measurable dichroism between the NN and AN geometries. It is possible to recognise two different effects on this dichroism:

1. the different width of the main line in these two geometries;

2. the spectral feature below 50 eV present only in the NN geometry.

The former effect was first observed by Gotter and co-workers for ferromagnetic Co/Cu(001) film [101]. In such a work it has been related to the difference in majority and minority density of states (DOS). To support this idea the authors have modeled coincidence spectra using the self convolutions of spin resolved DOS for singlet and triplet final spin state, appropriate for a two-hole final state of weakly correlated systems. In the same way the dichroism affecting the main line in Ni reflects the valence band splitting

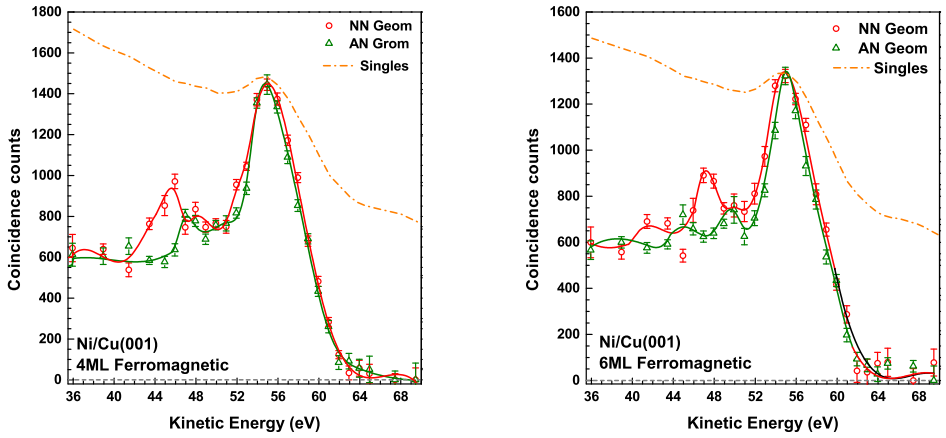

(a)

(b)

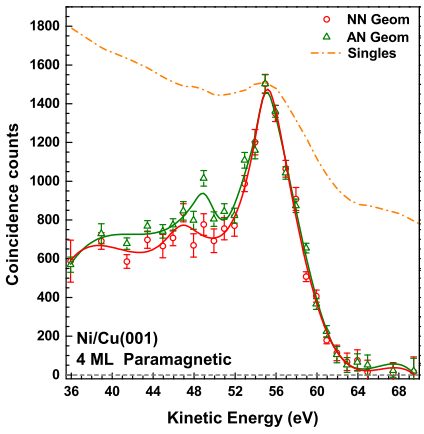

(c)

Figure 4.16: AR-APECS spectra for Ni/Cu(001). True coincidence counts are given as a function of the Auger kinetic energy. NN geometry is reported as red open circles with error bars, while AN geometry as green open triangles with error bars. Conventional (single) Auger spectrum is given as orange dashed line. The solid lines interpolating the experimental data are guides for the eye. Spectra in panel (a) are referred to a 4 ML-thick ferromagnetic film, those in panel (b) to a 6 ML-thick ferromagnetic film, while those in panel (c) are referred to a 4 ML-thick film in its paramagnetic state.

between majority and minority spin populations. To properly interpret the second dichroic effect listed above, i.e. the low kinetic energy feature in the NN geometry, an appropriate theoretical model is required. This because in comparing the AR-APECS spectra of Ni with the ones for Fe (both Fe/Ag right above and Fe/Cu in ref. [104]) the 46 eV feature shown can be associated for analogy to the Cini-Sawatzky resonance of the spin-symmetric ($\uparrow\uparrow$) contribution, but it characterises the NN geometry, which is in principle a singlet-selective geometry. It is also interesting to note that such a feature seems to lie at slightly different energy upon going from a thickness of 4 to 6 ML and it might be interesting to investigate, probing other systems in the ultrathin regime, if such an energy shift is due to a different degree of electron correlation induced by the different thickness or not.

The 4 ML-thick Ni/Cu(001) paramagnetic film has instead shown a reduced dichroism with respect to the others, as clearly shown in figure 4.17 where the DEAR-APECS effect is reported. For this system no dichroism, within the achieved statistics, is visible in the main line, suggesting that, as expected for a magnetic system above the Curie point, the valence band is no more split in two pure majority and minority sub bands. On the low kinetic energy side of the spectrum the dichroism can be considered quite small except for a feature at 48 eV in the AN geometry which results not present in the other kinematic condition. The $M_{23}M_{45}M_{45}$ transition of Ni seems very similar to the $L_{23}M_{45}M_{45}$ one reported by Sawatzky in [137]. Following the interpretation proposed in such a work, the main line is expected to be interpreted as a singlet ^1G followed by a triplet ^3F closer to the Fermi edge, in the high-kinetic energy side. The LMM spectrum reported in [137] is also characterised by a *satellite* structure at low kinetic energy, which has been interpreted as a $3d^7$ final state configuration, and lies at a distance from the main line compatible with the feature in the AR-APECS spectrum we are discussing, so we interpret such a structure as the satellite.

4.3 Insight of a FM/AFM bilayer interface spin multiplet terms via coincidence spectroscopy, the case of Fe/CoO

The atomic level origin of magnetic properties is the key for understanding magnetism. A crucial role for advancing knowledge and for developing new kind of devices is played by the comprehension of physical mechanisms behind interface phenomena, such as the interaction at a Ferromagnetic (FM)/Antiferromagnetic (AFM) interface, leading to the so called exchange-

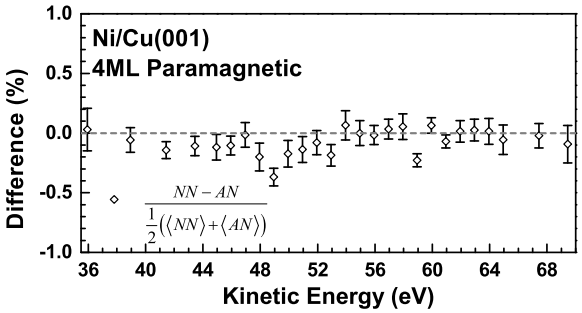

Figure 4.17: DEAR-APECS effect for the 4 ML-thick Ni film above the Curie temperature.

bias effect [138, for a review]. Interface coupling between different magnetic phases governs the behaviour of most of the current magnetic and spintronic devices such as tunnel magnetoresistance read heads, magnetoresistive random access memories (MRAMs) or magnetoresistive sensor recording media [139]. A fundamental issue is therefore understanding and controlling these interface phenomena in order to exploit them as a tool for governing magnetic coupling, thus allowing to optimise the performances and opening new perspectives for future devices. A prototype FM/AFM bilayer uses 3d-metal coupled with their oxides because this has some advantages with respect to other systems, for example it allow to achieve a very good control of the growth properties and consequently of the electronic and magnetic structure. Particularly Fe/TmO bilayers (where Tm stands for Transition metal), have been deeply investigated over the years [140] and recent analysis performed with different techniques like nuclear resonant scattering [141, 142], magneto optical Kerr effect [143, 144, 145] or X-ray absorption [144, 145, 146] have highlighted a complex interfacial scenario whose details might be understood only using element-sensitive experimental techniques that access to local properties.

In this section the acquisition of the $M_{23}M_{45}M_{45}$ Auger spectrum in coincidence with $3p$-core level photoemission for a Fe/CoO bilayer is presented. As for the other experiments described in this chapter, the AR-APECS spectra have been collected upon changing the kinematic condition between the two AN and NN geometries discussed so far. The partial Auger yield for this system, acquired with the Fe layer in a ferromagnetic state and with the CoO substrate antiferromagnetically ordered, can be directly compared to the one of Fe/Ag(001) discussed in the previous section, allowing to determine how the electronic and magnetic structure is influenced upon growing the Fe once on a non magnetic substrate and once on a magnetic one.

4.3.1 Experimental

A Fe/CoO/Ag(100) sample has been grown *in situ* by electron bombardment of high purity rods of the corresponding metals. Cycles of Ar^+ ion sputtering have been used to clean the (001) surface of the Silver single crystal substrate, resulting in x-ray photoemission spectra free of carbon and oxygen. An annealing up to 750 K has been made to get the crystallographic order. The CoO AFM phase has been obtained by depositing Co atoms in an oxygen atmosphere with a partial pressure of $P(O_2) = 1 \cdot 10^{-6}$ hPa and with the Ag(001) substrate kept at a temperature of 470 K, to avoid the formation of clusters with different crystallographic orientation [146], followed by a 30 minutes post-annealing at 750 K in the same oxygen atmosphere. The crystalline structure was monitored using RHEED pattern which has shown the same (001) crystallographic periodicity of the substrate. Photoemission spectra collected after this first step of growth resulted free of carbon and were used to evaluate the thickness resulting in a 25 ML-thick CoO film. According to [146] for thicknesses greater than 10 ML the Néel temperature of the AFM layer is the same of the bulk CoO, $T_N = 298$ K.

An epitaxial 3 ML-thick Fe layer has been grown on top of the CoO. As shown by the RHEED pattern in figure 4.18 the cubic cell is rotated by 45° with respect to the underlying layer, see panel (b) and (c) of the figure. Thickness estimation has been done calibrating the evaporation time using RHEED oscillation for the Fe/Ag(100), see figure 4.12b, and maintaining the same evaporation rate and exposure time. At the end of the sample preparation photoemission spectra were collected to check for absence of contaminants. The L_{23} absorption edge of the iron, in figure 4.19, has been measured after the sample preparation to verify the quality of the Fe film deposited onto the CoO substrate.

4.3.2 AR-APECS spectra

AR-APECS spectra on Fe(3ML)/CoO(25ML)/Ag(001) have been collected at a temperature of $T_{\text{Sample}} = 170$ K lower than both the Néel temperature and Curie point of the CoO and Fe respectively, so probing the metal and the oxide in their respective ordered magnetic phase. Primary photons with an energy of $\hbar\omega = 200$ eV have been used. These measures have been performed in the same geometries (AN and NN) discussed in the previous sections.

Representative AR-APECS spectra from Fe/CoO/Ag(100) are shown in figure 4.20. Spectra are shown as true coincidence counts versus kinetic energy of the Auger electrons and the conventional (singles) Auger spectrum as orange dashed line. Also in this case in referring to the two different geome-

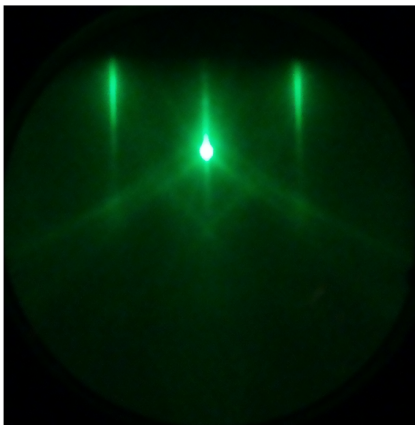

(a) Ag(001) single crystal.

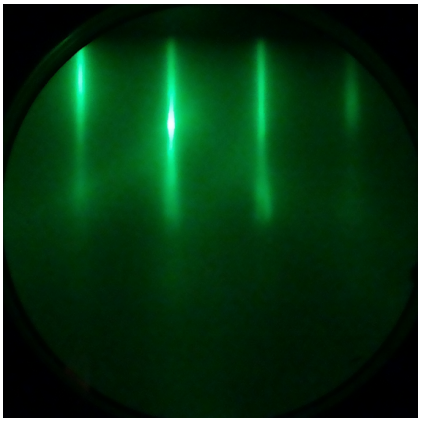

(b) RHEED pattern of CoO/Ag(001) after the CoO deposition. The pattern is due to a (001) symmetry similarly to the substrate.

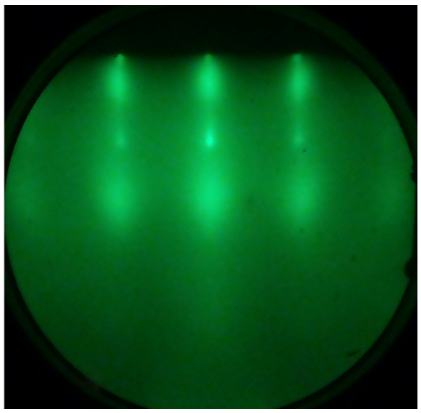

(c) RHEED pattern from the Fe layer grown onto the AFM CoO phase. The cubic surface cell of the Fe layer is rotated by 45° with respect tothe one of CoO.

Figure 4.18: RHEED patterns from Fe(3ML)/CoO(25ML)/Ag(001). The quality of each part of the multilayer (substrate, AFM phase and FM layer) has been verified separately.

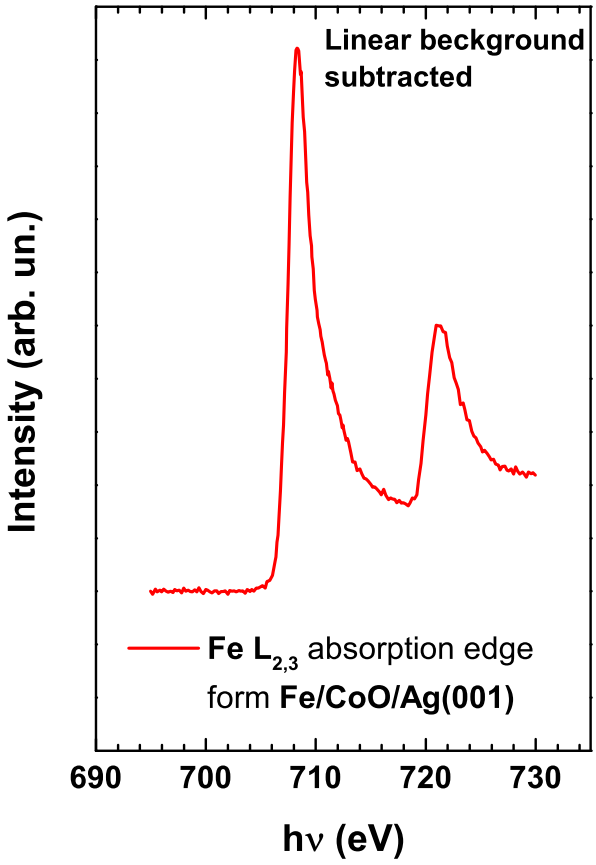

Figure 4.19: L_{23} absorption edge of Fe from Fe(3ML)/CoO(25ML)/Ag(001) at room temperature collected with the partial electron yield method.

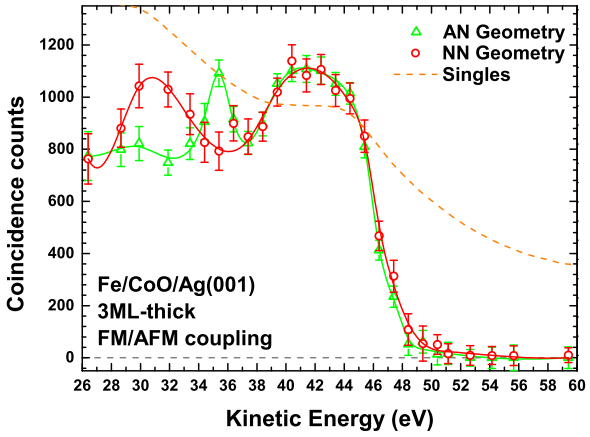

Figure 4.20: $M_{23}M_{45}M_{45}$ AR-APECS spectra in coincidence with $3p$-core level from Fe(3ML)/CoO(25ML)/Ag(001) at low temperature ($T = 170$ K).

tries the AN configuration is reported as green open triangles with error bars and the NN one as red open circles. Spectra from both the kinematics conditions show an onset around 49 eV and a broad main line with a centroid at 43 eV. Again in the low kinetic energy side of the spectrum two main features, one per spectrum, are present, whose nature is expected to be related to the correlation effect as in the case of the Fe/Cu [104]. The idea is to compare the AR-APECS spectra of this FM/AFM interface with respect to the one of Fe/Ag(100), discussed in the previous section, to highlight any change in magnetic structure of the Fe layer due to the magnetic interaction between the two phases. In figure 4.21 spectra collected on the same geometry for both Fe/Ag and Fe/CoO are compared. The different magnetic nature of the substrate shows itself as a broadening on the main line and it seems to affects mainly the "low spin" configuration, shifting towards higher binding energies the satellite features. Also the onset of the spectrum seems to have suffered some changes: as highlighted in panels (c) and (d) of figure 4.21 differences involve mainly the spectral distribution from the onset up to the main line. Such differences in turn are an hint of changes in the electronic structure, hence in magnetic and transport properties, suggesting that the interfacial magnetic interaction plays a role at atomic scale.

Again the support of a dedicated theory is needed to put this interpretation on more quantitative grounds.

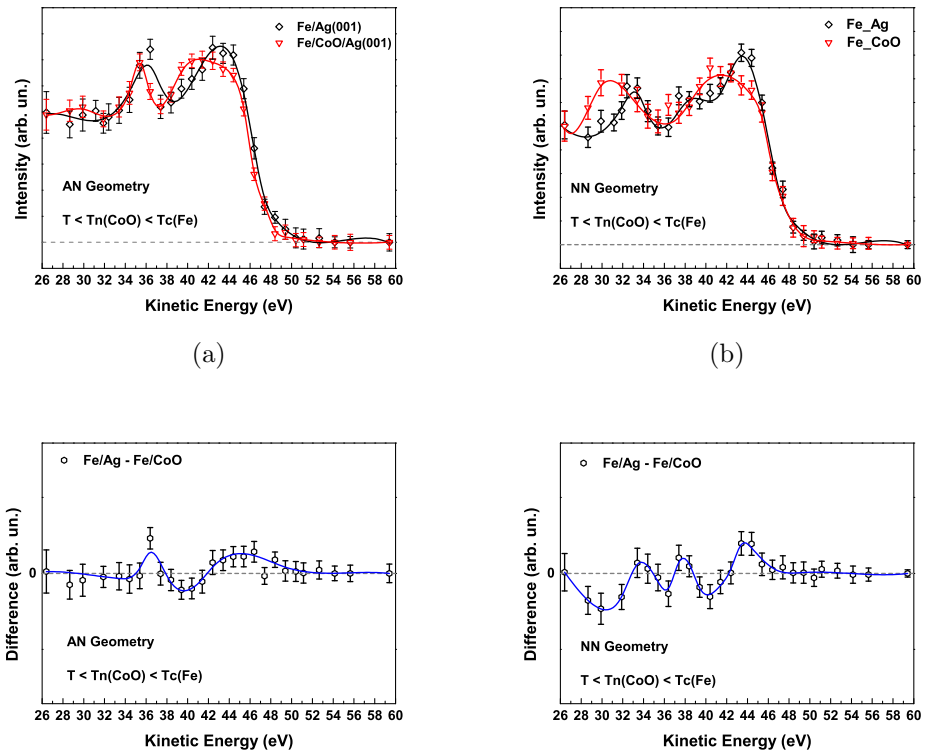

Figure 4.21: Comparison between AR-APECS spectra collected for Fe/Ag and Fe/CoO: panel (a) reports the spectra collected in the AN geometry, while in panel (b) the comparison of the spectra collected in the NN geometry is reported. Panels (c) and (d) show the difference in the spectra of the respective geometries. Solid lines are guide to the eyes.

Conclusions

In this thesis work Auger PhotoElectron Coincidence Spectroscopy (APECS) has been applied to investigate the $M_{23}VV$ Auger transition in magnetic materials.

Motivations to undertake this experimental work must be found in the fact that atomic level origin of magnetic properties in condensed matter is the key for the comprehension of magnetism and up today a microscopic theory is still missing. Nodal points requiring a detailed insight are both the discernment of whether or not the magnetic order is lost even at short-range once the critical point is exceeded and the understanding of interface phenomena between different magnetic phases. These issues have been largely debated in the last decades, but at the state of the art a satisfactory microscopic description has not been achieved yet. Addressing these issues is typically a challenge, because local information on an element selective basis is needed.

APECS spectroscopy, performed in an Angle-Resolved mode (AR-APECS), gives access to the final state multiplet configuration in a spin-selective fashion. It has been shown [37] that AR-APECS is able to unravel or not multiplet contributions respectively below and above the critical temperature of a magnetic system, hence allowing to investigate magnetic phase transitions from a local point of view, contributing to solve the issue about the loss of short-range magnetism.

By using the linearly polarised light of a synchrotron radiation facility and the unique experimental chamber of the ALOISA beamline AR-APECS has been performed both on ferromagnetic (FM) and antiferromagnetic (AFM) systems, particularly probing NiO, Ni and Fe. Also for the first time, AR-APECS has been applied to a FM/AFM interface, namely the Fe/CoO bilayer.

The $M_{23}VV$ Auger transition from NiO/Ag(001) has been measured both below and above the Néel temperature of our film. Combining the dipole and Auger selection rules with the angular distribution of electrons whose partial waves are characterised by different magnetic quantum numbers, AR-APECS

gives the possibility to access the local spin configuration of the Auger final state. Electron-pairs have been collected in two different kinematic conditions in order to achieve the so called high-spin (triplet) versus low-spin (singlet) selectivity. This has been made using two different geometries, the AN in which the photoelectron is collected aligned and the Auger electron not aligned with respect to the light polarisation vector and the NN in which both the electrons are collected in directions not aligned with it. A magnetic dichroism has been measured when the sample was probed at a temperature lower than the Néel value. In particular a redistribution of spectral intensity towards the spin-antisymmetric (singlet) at expenses of the spin-symmetric (triplet) final state has been observed when passing from AN to NN geometry. The large dichroism gave the possibility to unambiguously assign the different multiplet terms. Once the critical temperature is exceeded AR-APECS spectra no longer show any asymmetry between the two geometries.

The $M_{23}VV$ Auger transition has been collected both for Fe/Ag and Ni/Cu, probing the Fe only in its ferromagnetic phase, while for Ni the coincidence spectra have been collected for two different film thicknesses crossing the Curie point. In this case the occurrence of DEAR-APECS collecting electron-pairs emitted in the decay of the M_{23} core-hole in the two AN and NN geometries shows itself as an asymmetry in the main line, but more relevantly, as a feature which could be associated to a high-binding energy resonance.

APECS has been also applied to a FM/AFM magnetic bilayer. Using the same kinematic conditions as in the case of Fe/Ag, the experiment has been carried out probing a Fe/CoO bilayer at a temperature lower than both the Curie and Néel points of the respective magnetic phases. As for the case of Fe and Ni, a large asymmetry in AR-APECS spectra has been observed once probed in its ordered magnetic state.

APECS spectroscopy gave access to a detailed investigation of the $M_{23}VV$ Auger spectrum for both FM and AFM systems showing how such a transition reveals a different behaviour between these two cases. For FM samples this transition results dominated by the main line only followed by an higher binding energy feature which could be associated to a resonance, thus showing both band-like and atomic-like character at the same time. On the contrary, spectra from AFM systems show a series of sharp peaks revealing a strong atomic-like behaviour. This large difference is a proof of the different degree of electron correlation characterising these kind of systems. For an FM like Fe or Ni the open valence shell allows for the delocalisation of electrons in the conduction band, thus leading to a reduced electron-electron interaction, while in AFM systems, like in NiO, even if the Ni is in an open band $3d^8$ configuration, the local electron correlation plays the dominant role and is

responsible for the atomic-like spectrum. Such an observation suggests that while the magnetism of AFMs finds its origin in the local atomic moments, for FMs the itinerant character of electrons plays a crucial role.

Once APECS has unravelled the multiplet structure of the final state holes, comparison with a theoretical model has shown that in order to interpret the Auger final state in AFM metal oxides a cluster calculation results suitable, accounting for the several atomic-like peaks. On the contrary, the spectrum of FM systems requires both the self-convolution of the density of states and the Cini-Sawatzky theory to be fully interpreted. Thus it reveals the nature of both the band-like main line transition and the atomic-like peak which could be associated to a resonance. While the former shows an asymmetry that reflects the majority vs. minority unbalance in the valence band spin population, the latter could arise from the spin coupling of two majority electrons, revealing in the valence band the presence of a localised state which is characterised by a large correlation.

In both kind of investigated systems the collapse of the dichroism once the transition temperature is exceeded has been observed. This behaviour puts in evidence the possibility to discriminate upon the magnetic phase of a system monitoring the phase transition from a localised viewpoint without the necessity to rely on thermodynamics arguments or crystal periodicity. It is well known that the long-range magnetic order is lost when a magnetic system is brought at a temperature larger than its critical point and the magnetisation gets randomised, but this is not enough to justify the complete collapse of the dichroic effect in AR-APECS (DEAR-APECS). The strain affecting our investigated films is such that the magnetisation is preferentially stabilised into the surface plane. In performing the AR-APECS measurements both below and above the transition temperature no structural changes affected our films. Hence, in case, even if randomly oriented, the magnetisation of our thin film still lies in the surface plane, while the two emitted electrons are collected in a plane perpendicular to the sample surface. This implies that the AR-APECS cross-section is not averaged over all the possible angular directions, thus a dichroism is to be expected anyway if the magnetic moment is still present. The presence of magnetic moments affects the AR-APECS spectra via matrix elements; AR-APECS cross-section for spin-polarized atomic target, which up to now is the only available calculation for what concerns the application of APECS to "magnetic systems", contains three relevant kinematic vectors, the momenta of the two emitted electrons and the magnetisation. Changes in one of these vectors can be accounted as responsible for changes in the AR-APECS spectra. In the light of this calculation the collapse of any DEAR-APECS effect when the magnetic transition temperature is crossed must be referred to the loss of one of

these relevant vectors. Of course, because the electrons are collected under the same conditions both below and above the critical point, the collapse of DEAR-APECS is an evidence for the loss of the local magnetisation.

For the first time APECS has been used to reveal the effect of a magnetic substrate coupled with a FM layer. The $M_{23}VV$ Auger transition of Fe once in contact with an AFM phase, like CoO, has shown differences with respect to what observed in the case of a non magnetic substrate. Particularly the presence of magnetic substrate has led to the broadening of the main line and to a shift of the low-kinetic energy feature, but more relevant are differences affecting the onset. This latter part of the spectrum corresponds to Auger decays involving electrons close to the Fermi surface which are the ones responsible for magnetic and conduction properties of the system. Hence what observed is an evidence for important changes in the band structure, which in turn involves changes in magnetic and transport properties.

Supported by a dedicated theory these experiments should be able to unravel the nature of the $M_{23}VV$ Auger transition for both FM and AFM systems, but unfortunately, a unified theory describing AR-APECS in magnetic systems has not been developed yet, but these experimental results are very encouraging to a theoretical challenge.

Appendix A

Data analysis

In the following a description of the data analysis process used to get the AR-APECS spectra presented in this thesis will be described in its principal aspects.

Coincidence spectra have been collected scanning with a multichannel detector (MCP) the energy window correspondent to the MVV Auger transition. In doing so we have set a large pass-energy for the dispersive element to gain in acquisition rate. It is well known that such a choice affects the energy resolution, which remains anyway appropriate to collect the broad spectrum we are interested in. In practice we have scanned an approximately 35 eV wide region collecting around 15 eV at a time (which is the energy window that can be smeared on the MCP's channels at 100 eV pass-energy we used) moving such an energy window in steps of 0.5 eV. We spent 2×120[1] s in the acquisition of coincidence events for each energy position of the MCP before moving to the next one. In order to achieve a reasonable statistics such a scan has been repeated several times. This procedure has to be preferred with respect to the choice of a single energy scan and a long acquisition time for each energy position of the MCP and this because these coincidence measurements are very time consuming (the coincidence rate is usually of the order of 0.01 counts/s): spending a long time in collecting a single energy position leads to acquire events in the first MCP energy position in a sample condition which can be different from the one in which you are acquiring data in the last position expected in the scan because of the sample evolution. Scanning more than once the same energy region spending few seconds for each MCP position prevents the problem because it averages sample evolution on the entire region, affecting the whole spectrum in the

[1] 2×120 means that for every MCP energy position, controlled by its central energy value, a 2 second acquisition is repeated 120 times before moving to the next position.

same manner.

During the period in which this thesis work was carried out, the format for saving coincidence data consisted of four different files per scan identified by different extension and content:

File.cou This file contains axial singles for every energy position of the MCP: a column is reserved for each axial analyser.

File.prx This file contains the snapshot of the MCP, hence the portion of the Auger spectrum inside the energy window collected for a given MCP position. It is made by $2 + 300$ columns as follow

E_k	E_{pass}	Snapshot (300 columns)

Every 2 seconds acquisition produce a row, hence for each central energy value of the MCP 120 rows are created.

File.sum This file contains a number of rows equals to the number of different energy positions of the MCP and is therefore given by $[(E_{\text{First}} - E_{\text{Last}})/step] + 1$. Every row results from the sum over the 120 rows of the *File.prx* corresponding to the same kinetic energy position.

File.cnx This file contains the coincidence events. Every coincidence (true and accidental as well) produces a row. Every row is made by 6 columns reporting all the information necessary to reconstruct the electron-pair characteristics: in the first column is reported the central kinetic energy value of the MCP multiplied by 100; in the second an identification number (unique) is associated to each coincidence event; in the third and fourth columns the arrival $x - y$ coordinates (respectively angular and energy dispersion) of the Auger electron on the MCP are given; the fifth column reports the TDC channel i.e. the position that the electron-pair takes in the histogram of the delay times between the two electrons; the last column lists the number of the analyser which gave the stop signal.

$E_k * 100$	ID code	x pixel	y pixel	TDC channel	Stop

In the following let us focus only on the *File.cnx*.

A.1 Filters

The first step in the data analysis is the selection of real and reliable coincidence events recorded. First of all in order to avoid to put inside the analysis coincidence events for which the Auger electron has impinged on the edge of the MCP, where it results less efficient, some constraints for the energy and angle dispersion, i.e. on the (x, y) coordinates, has been inserted. So once fixed the initial and final energy and angle bins, only events showing the (x, y) pair in the range allowed are taken into account. These events have to follow a filter refinement in order to remove spurious coincidence events produced by the electronics and reflections inside the acquisition chain. Such events are easily identifiable because characterised by the same ID number of the real previous(es) event(s) and by null (x, y) coordinates, i.e. $(0, 0)$ which means that the hypothetical electron has to be detected exactly at the corner of the MCP which is not a very probable condition. Of course if an event shows $(0, 0)$ coordinates, but a different stop analyser with respect to the previous row is accounted as a genuine event. A dedicated filter procedure, which compares the values of the second, third, fourth and last columns of a certain row with both the corresponding of the previous event and the set constraints discern between genuine and fake coincidence events, creating a new file where the latter kind of events is not included. An example of *File.cnx* before and after the filtering is reported in the following tables A.1 and A.2: in the example the allowed range for both energy (y) and angular dispersion (x) has been set to $40 < x < 104$ and $45 < y < 260$; to guide the eye fake events have been marked in bold.

In order to achieve a proper statistics, spectra require several hours of acquisition, i.e. every APECS spectrum presented is the result of the sum of tens of **.cnx* files. Of course the filtering must be performed for each of these files.

A.2 Time spectra construction

Time spectra[2] are built up starting from such a kind of *File.cnx* presented above. Electron-pairs are divided according to their energy: the photoelectron energy is fixed, hence only the Auger kinetic energy is involved in the allocation. The whole Auger energy window acquired is thus divided in several bins and for each of these bins only those Auger electrons for which the kinetic energy (determined by the central energy of the MCP and the y

[2]See section 3.4.1

$E_k * 100$	ID code	x pixel	y pixel	TDC channel	Stop
4500	**1005**	**30**	**142**	**480**	**1**
4500	1016	67	96	1346	3
4500	1705	87	252	1886	4
4500	1867	103	75	4007	5
4500	**1907**	**0**	**0**	**469**	**2**
4600	521	102	174	184	1
4600	**521**	**0**	**0**	**406**	**1**
4600	540	80	184	414	2
4600	1248	70	159	2870	1
...	...	...	...	...	...
...	...	...	...	...	...
...	...	...	...	...	...

Table A.1: Example of a *File.cnx* before the filtering procedure. In this case nine rows associated to coincidence events collected with the MCP central energy both at 45 and 46 eV are reported. First and fifth rows in bold represent two genuine events characterised by (x, y) values out of the allowed range (e.g. $40 < x < 104$; $45 < y < 260$), the seventh row, in bold, is a fake event produced by the electronics.

$E_k * 100$	ID code	x pixel	y pixel	TDC channel	Stop
4500	1016	67	96	1346	3
4500	1705	87	252	1886	4
4500	1867	103	75	4007	5
4600	521	102	174	184	1
4600	540	80	184	414	2
4600	1248	70	159	2870	1
...	...	...	...	...	...
...	...	...	...	...	...
...	...	...	...	...	...

Table A.2: Example of the same *File.cnx* of table A.1 after the filtering procedure. The rows marked in bold associated to undesired or fake events are no longer included.

arrival coordinate of the electron onto the detector) falls inside that range are considered. Once distributed the coincidence events for each bin it is possible to extract the correspondent time spectrum, which represents the time distribution of those electrons whose kinetic energy is in between E_i and $E_{i+1} \equiv E_i + \Delta E$. Thus running on the fifth column of the *File.cnx* an histogram can be built, binning also the time window, but instead of adding a unity in correspondence of a certain bin every time a specific delay, belonging to that bin, is observed, the quantity $1/n$ is added where n is the efficiency of the (x, y) MCP pixel at which the electron has been detected. This is done including in the data analysis an MCP normalisation matrix.

A.3 Peak alignment

APECS spectra presented in this thesis are angular-resolved in two different kinematics as reported in the text of section 3.5 and summarised in table 3.3. Both the so called AN and NN geometries are made up combining electron-pairs collected from more than one axial analyser. Every analyser is associated to an independent acquisition chain as schematically illustrated in figure 3.17 on page 99 and a little difference in the signal transit time inside these five different paths has to be expected. This implies that to put together the coincidence counts coming from different analysers but belonging to the same kinematic condition, as in the case of the NN geometry made by electron-pairs collected using the bimodal analyser and the axial analysers labeled as 1 and 5 in figure 3.19 on page 106, a proper alignment of the coincidence peaks in the time spectra has to be taken into account. This procedure, made by shifting rigidly the whole time spectrum in order to move the coincidence peak to a chosen value, has to be performed for each analyser and prevents from obtaining time spectra affected by multiple peaks. In figure A.1 the time spectrum of the NN geometry for one of the experiments proposed is reported both with and without a proper alignment of the time spectra from axial analysers 1 and 5. The effect of the peak alignment is quite clear.

A.4 Time correction

Delay times shown by different electron-pairs can result affected by differences in time of flight. Let us consider two distinct electron-pairs both made by photo- and Auger electrons "simultaneously" ejected. These two pairs are expected to contribute to the same peak in the time spectrum. However

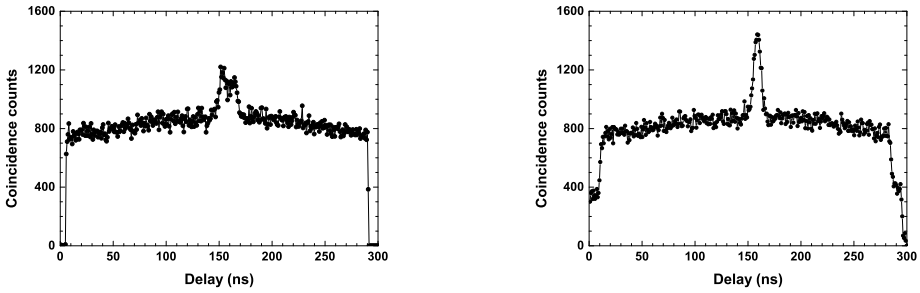

(a) (b)

Figure A.1: In panel (a) the energy integrated (i.e. considering the entire energy window collected) time spectrum for NN geometry made by putting together coincidence events from the bimodal (B) with both the numbers 1 and 5 axial analysers (An1 and An5 respectively) is reported without any time alignment. In panel (b) the same time spectrum is reported after moving the time spectra of B-An1 and B-An5 in order to put the peak centred at the same delay.

Auger electrons produced in the same physical process can have different energies i.e. different velocities and will cover the distance between the sample and the detector in different times. As a consequence these two electron-pairs will result associated to different delays, simply because the "start" signal for the TDC is triggered by the detection of the Auger electron. This effect can be corrected thanks to the fact that the MCP equipping the experimental set-up can discriminate upon different energies by determining the arrival position of electrons. In order to correctly assign the delay time of a coincidence event a linear correction of the form $t' = t + c_y y$ is applied to the time spectrum, where t' and t represent the corrected and uncorrected delay times respectively, y the arrival pixel in the energy dispersive direction and c_y an opportune constant. Such a coefficient is the one which minimises the width of the true coincidence peak. Such a correction is made on the energy integrated time spectrum, that is an high-statistics distribution, and is needed to properly determine the uncorrelated background which is used in the fitting procedure as will be described in the following.

A.5 Building different kinematics

In the data analysis process it is possible to get AR-APECS spectra coming from all the five different couples of analysers. To separate events belonging to such couples is sufficient to run over the last column of the *File.cnx*

and regroup them according to this value. Once the coincidence events are filtered, aligned and properly corrected it is possible to build the different kinematics, according to table 3.3, simply replacing the last column values. Let us consider the case of the NN geometry for which coincidence events coming from B-An1 and B-An5 couples have to be summed: it is possible to put together these coincidence events replacing the last column value from 5 to 1. In this case running over this column all the events collected in the NN kinematic condition are regrouped together.

A.6 From time spectra to APECS spectra

APECS spectra proposed in this thesis report the number of coincidence events as a function of the Auger electrons kinetic energy. The whole Auger energy window is thus divided in several bins and on the abscissa the central value of each bin is reported. For each bin the time distribution of electron-pairs, i.e. the time spectrum, gives the number of coincidence events associated to the correspondent energy.

In the case of continuous sources, like an e^--gun or a common X-ray lamp, the number of coincidence counts can be determined dividing the entire time spectrum into three regions setting two values t_1 and t_2, in the relation $t_1 < t_2$, in such a way that for $t < t_1$ and for $t > t_2$ only accidental counts are present, while in the region $t_1 < t < t_2$ the coincidence peak is included (see figure A.2). Both accidental and true coincidence counts contribute to the area under the peak, A_t, hence it can be expressed as

$$A_t = \sum_{t_i=t_1}^{t_2} c_i$$

where c_i represents the coincidence counts associated to the time delay t_i, assuming an unitary interval Δt_i. The associated uncertainty follows the Poisson's statistics thus

$$\sigma_{A_t} = \sqrt{\sum_{t_i=t_1}^{t_2} c_i}.$$

To get the number of true counts it is necessary to quantify the background contribution to A_t. To do this the number of coincidence events, A_e, contributing to the background at the two sides of the peak must be calculated:

$$A_e = \sum_{t_i<t_1} c_i + \sum_{t_i>t_2} c_i$$

which uncertainty is given by

$$\sigma_{A_e} = \sqrt{\sum_{t_i<t_1} c_i + \sum_{t_i>t_2} c_i}.$$

Now, because the uncorrelated electron-pairs are uniformly distributed in the whole time window allowed, it is possible to determine the accidental coincidence contribution under the peak, A_c, applying a simple proportion: termed Δt the time interval between t_1 and t_2, i.e. the peak region, and ΔT the remainder of the allowed time window, i.e. where only accidental counts are recorded, A_c will read

$$A_e : \Delta T = A_c : \Delta t \quad \Rightarrow \quad A_c = \frac{\Delta t}{\Delta T} A_e \tag{A.1}$$

and its uncertainty is

$$\sigma_c = \frac{\Delta t}{\Delta T} \sigma_e.$$

The true counts, N_t, are now obtainable as a simple difference between A_t and A_c, i.e. the difference between the total area and the background contribution under the peak:

$$N_t = A_t - A_c = \sum_{t_i=t_1}^{t_2} c_i - \frac{\Delta t}{\Delta T} \left(\sum_{t_i<t_1} c_i + \sum_{t_i>t_2} c_i \right)$$

$$\delta N_t = \sqrt{\sum_{t_i=t_1}^{t_2} c_i + \left(\frac{\Delta t}{\Delta T}\right)^2 \left(\sum_{t_i<t_1} c_i + \sum_{t_i>t_2} c_i \right)}$$

This last expression justify the use of such a wide time window: the larger the background region, the lower the uncertainty of the true coincidence counts, because a better determination of the background contributing under the peak is achieved.

Let us now focus on the case of pulsed sources, like in our case where the synchrotron radiation has been used, which are characterised by a non uniform background due to uncorrelated electrons. This because the background reflects the characteristic of the source: in the case of synchrotron light a triangular background comes from the self-convolution of the ring-fill. In this case an approach like the one proposed just above leads to an erroneous determination of true coincidence counts, especially for the side energy values of the spectrum where the difference between the true coincidence peak and the background is not as sharp as in the case of central energies. To get the true counts as the difference of the total area and the

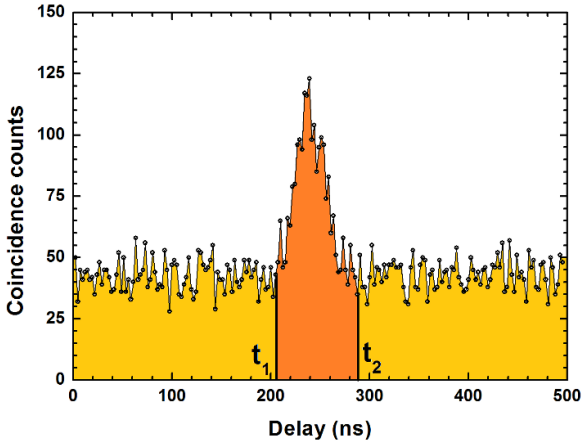

Figure A.2: An example of time spectrum due to an e^--gun is reported. The spectrum is divided into three regions: the two yellow areas, for $t < t_1$ and $t > t_2$, made by accidental counts and the peak region, in orange, for $t_1 < t < t_2$, containing true coincidence events piled-up the accidental background.

accidental counts in the time window under the peak this last contribution must be determined, but applying a proportion as in equation (A.1) an underestimation of the accidental counts, because of the triangular shape of the background, is obtained. In order to overcome this a fitting procedure is used. The fitting function employed is made by a background and two gaussian peaks reproducing the coincidence peak which shows a little asymmetry. The background is determined from the time distribution of all the electron-pairs collected for that specific geometry, i.e. considering the whole energy window as a unique bin. Such a time spectrum corresponds to the overall statistics acquired for that geometry, so it is the best candidate to extract the background's shape: after the subtraction of the peak, reproduced with a gaussian function[3], the background is straightforwardly obtained. This background, scaled by a coefficient lower than 1 which is treated as a fitting parameter, is used in fitting the time spectra for each energy bin. The areas of the gaussian functions are the coincidence counts associated to that energy.

The last step in data analysis is the normalisation of the energy spectrum. The acquisition mode for coincidence spectra foresees to move a 15 eV energy

[3]In fitting the energy integrated time spectrum the gaussian peak is superimposed to a polinomial function.

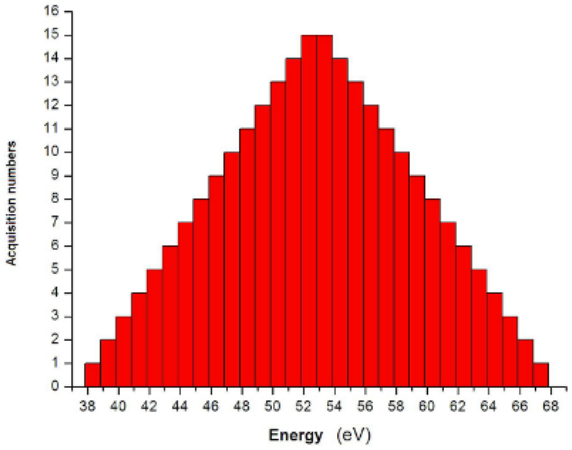

Figure A.3: Normalisation function for APECS spectra: the center of the nearly 15 eV energy window of the MCP has been moved from $E_1 = 45$ eV to $E_2 = 60$ eV with steps of $\Delta E = 1$ eV.

window from a certain first energy position E_1 to a last position E_2 with a certain step, e.g. $\Delta E = 0.5$ eV, covering about 35 eV. This means that the time spent in the acquisition of coincidence events in each energy bin is different from another. In this case a normalisation function built on the basis of the first and last energy positions, on the energy window moved and on the binning performed, like the one in figure A.3, is used.

Ringraziamenti

Portare a termine questo percorso di dottorato é stata una sfida difficile. Pensavo di lasciare giá dopo i primissimi mesi, ma giorno dopo giorno, non senza difficoltá, sono arrivato fin qui. Ora posso dire che questi tre anni sono stati ricchi di esperienza, non solo da un punto di vista formativo e professionale. Rispetto a quando ho cominciato questo ciclo molte cose sono cambiate. Tutto questo ha contribuito a riempire il mio bagaglio, sono entrato in contatto con nuovi strumenti che ho fatto miei e che mi torneranno utili nel proseguio del cammino.

Vorrei allora condividere la gioia per questo nuovo traguardo con chi ha condiviso con me questo percorso. In primo luogo devo ringraziare il Prof. Giovanni Stefani, mio supervisore, per la disponibilitá concessami nel seguirmi durante il mio dottorato e per tutto il supporto offertomi in questo cammino di crescita. Vorrei condividere poi questo traguardo con tutte le altre persone con cui ho collaborato nel laboratorio LASEC partendo dal Prof. Alessandro Ruocco, che ringrazio per la fiducia che ha riposto nelle mie potenzialitá, ringrazio poi Francesco Offi, Stefano Iacobucci ed Adriano Verna per il loro supporto, che nei momenti di necessitá non é mai mancato. Condivido volentieri questo risultato con Giorgia Greco, la donzella del gruppo, che ogni giorno ha trovato modo di intrattenermi a chiacchiere durante i pasti e che non ha smesso di fare il tifo per me, anche quando le giornate sembravano veramente storte. Vorrei ringraziare poi i dottorandi vecchi e nuovi con i quali ho condiviso il laboratorio: partendo dai piú giovani Valerio Serpente e Gian Marco Pierantozzi; ringrazio poi Gianluca Di Filippo con il quale ho condiviso due anni di questa esperienza e che é stato fonte di ispirazione e confronto. Un ringraziamento particolare va a Valerio Lollobrigida, che si é rivelato un amico piú che un collega, lo ringrazio per tutto il supporto e la fiducia offertami, fino all'ultimo, per avermi accolto nella sua famiglia e per essere entrato in contatto con i miei mondi, dai piú sacri ai piú profani (sagre comprese!!!). Ringrazio poi tutte le persone che, pur non facenti parte del mio gruppo, hanno condiviso questi anni di lavoro con me: ringrazio Roberto Gotter, per l'esperienza trasmessami durante i

turni al sincrotrone e non solo, ringrazio Shital R Vaidya, una dottoranda con cui ho condiviso molto di questo percorso e con la quale c'é stato un piacevole scambio culturale; ringrazio poi Francesco Bisio e Riccardo Moroni con i quali ho condiviso le difficoltá sperimentali di questo cammino. Ringrazio tutto lo staff della beamline ALOISA ad Elettra per il supporto fornitomi durante la realizzazione degli esperimenti proposti in questo lavoro ed infine i Proff. Michele Cini e Robert Bartynski che ho avuto modo di incontrare durante questo viaggio.

Come non ringraziare i miei amici di infanzia Lorenzo e Massimo con i quali ho da sempre fatto le peggio stronzate e tuttora non ci smentiamo.

Il posto d'onore peró lo occupa la mia famiglia, un serbatoio infinito di amore che mi spinge ad andare avanti sempre, un sostegno immancabile in qualunque momento della mia vita. Ringrazio mamma Leonarda e papá Franco per come mi hanno insegnato a vivere, trasmettendomi il loro modo di vedere le cose e lasciandomi libero di sviluppare il mio, per come da sempre mi hanno guardato crescere e per come lo fanno ancora. Ringrazio Mario, Tiziana, Sara e Adele, la famiglia della mia compagna, per avermi accolto da oltre dieci anni in casa come un figlio e un fratello. Ringrazio infine la mia nuova famiglia, Silvia la mia compagna, sempre al mio fianco, pronta ad accogliermi ogni volta che faccio ritorno al porto, ed infine la piccolina di casa, la nostra figlia Irene, i cui sorrisi sinceri sono la cura ad ogni male. Vi ho tutti nel cuore.

Marco.

Bibliography

[1] P. Hohenberg and W. Kohn. *Phys. Rev.*, **136**: B864, 1964.

[2] W. Kohn, A. D. Becke, and R. G. Parr. *J. Phys. Chem.*, **100**: 12974, 1996.

[3] G. A. Sawatzky and J. W. Allen. *Phys. Rev. Lett.*, **53**: 2339, (1984).

[4] F. O. Schumann, L. Behnke, C. H. Li, and J. Kirschner. *J. Phys.: Condens. Matter*, **25**: 094002, (2013).

[5] V. I. Anisimov, I. V. Solovyev, M. A. Korotin, M. T. Czyżyk, and G. A. Sawatzky. *Phys. Rev. B*, **48**: 16929, (1993).

[6] H. A. Mook, J. W. Lynn, and R. M. Nicklow. *Phys. Rev. Lett.*, **30**: 556, (1973).

[7] D. E. Eastman, F. J. Himpsel, and J. A. Knapp. *Phys. Rev. Lett.*, **40**: 1514, (1978).

[8] C. J. Maetz, U. Gerhardt, E. Dietz, A. Ziegler, and R. J. Jelitto. *Phys. Rev. Lett.*, **48**: 1686, (1982).

[9] W. Eberhardt, E. W. Plummer, K. Horn, and J. Erskine. *Phys. Rev. Lett.*, **45**: 273, (1980).

[10] H. Hopster, R. Raue, G. Güntherodt, E. Kisker, R. Clauberg, and M. Campagna. *Phys. Rev. Lett.*, **51**: 829, (1983).

[11] H. Ibach. *Physics of Surfaces and Interfaces*, chapter 9.5. Springer, 2006.

[12] J. Kirschner and E. Lagenbach. *Solid State Commun.*, **66**: 761, (1988).

[13] E. Kisker, K. Schröder, M. Campagna, and W. Gudat. *Phys. Rev. Lett.*, **52**: 2285, (1984).

[14] J. Kirschner, M. Glöbl, V. Dose, and H. Scheidt. *Phys. Rev. Lett.*, **53**: 612, (1984).

[15] K.-P. Kämper, W. Schmitt, and G. Güntherodt. *Phys. Rev. B*, **42**: 10696, (1990).

[16] P. Aebi, T. J. Kreutz, J. Osterwalder, R. Fasel, P. Schwaller, and L. Schlapbach. *Phys. Rev. Lett.*, **76**: 1150, (1996).

[17] W. von der Linden, M. Donath, and V. Dose. *Phys. Rev. Lett.*, **71**: 899, (1993).

[18] B. Sinkovic, L. H. Tjeng, N. B. Brookes, J. B. Goedkoop, R. Hesper, E. Pellegrin, F. M. F. de Groot, S. Altieri, S. L. Hulbert, E. Shekel, and G. A. Sawatzky. *Phys. Rev. Lett.*, **79**: 3510, (1997).

[19] M. Pickel and A. B. Schmidt and M. Weinelt and M. Donath. *Phys. Rev. Lett.*, **104**: 237204, (2010).

[20] D. W. Jeong, H. C. Choil, C. H. Kim, S. H. Chang, C. H. Sohn, H. J. Park, T. D. Kang, D. Y. Cho, S. H. Baek, C. B. Eom, J. H. Shim, J. Yu, K. W. Kim, S. J. Moon, and T. W. Noh. *Phys. Rev. Lett.*, **110**: 247202, (2013).

[21] E. P. Wohlfarth. *Rev. Modern Phys.*, **25**: 211, (1953).

[22] J. Hubbard. Proceedings of the Royal Society of London. Series A. *Mathematical and Physical Sciences*, **276**: 238, (1963).

[23] V. I. Anisimov, J. Zaanen, and O. K. Andersen. *Phys. Rev. B*, **44**: 943, (1991).

[24] A. I. Liechtenstein, V. I. Anisimov, and J. Zaanen. *Phys. Rev. B*, **52**: R5467, (1995).

[25] M. Imada, A. Fujimori, and Y. Tokura. *Rev. Mod. Phys.*, **70**: 1039, (1998).

[26] G. Kotliar and D. Vollhardt. *Phys. Today*, **57**(No. 3): 53, (2004).

[27] H. W. Haak, G. A. Sawatzky, and T. D. Thomas. *Phys. Rev. Lett.*, **41**: 1825, (1978).

[28] O. Gunnarsson and K. Schönhammer. *Phys. Rev. Lett.*, **46**: 859, (1981).

[29] R. Gotter, F. Da Pieve, F. Offi, A. Ruocco, A. Verdini, H. Yao, R. Bartynski, and G. Stefani. *Phys. Rev. B*, **79**: 075108, (2009).

[30] E. Jensen, R. A. Bartynski, S. L. Hulbert, E. D. Johnson, and R. Garrett. *Phys. Rev. Lett.*, **62**: 71–73, (1989).

[31] M. Cini. *Solid State Commun.*, **24**: 681, (1977).

[32] G. A. Sawatzky. *Phys. Rev. Lett.*, **39**: 504, (1977).

[33] M. Cini and V. Drchal. *J. Electron Spectrosc. Relat. Phenom.*, **72**: 151, (1995).

[34] P. J. Feibelman, E. J. McGuire, and K. C. Pandey. *Phys. Rev. B*, **15**: 2202, (1977).

[35] G. Stefani, R. Gotter, A. Ruocco, F. Offi, F. Da Pieve, S. Iacobucci, A. Morgante, A. Verdini, A. Liscio, H. Yao, and R.A. Bartynski. *J. Electron Spectrosc. Relat. Phenom.*, **141**: 149, (2004).

[36] R. Gotter, F. Da Pieve, A. Ruocco, F. Offi, G. Stefani, and R. Bartynski. *Phys. Rev. B*, **72**: 235409, (2005).

[37] R. Gotter, F. Offi, A. Ruocco, F. Da Pieve, R.A. Bartynski, M. Cini, and G. Stefani. *Europhys. Lett.*, **94**: 37008, (2011).

[38] B. D. Cullity and C. D. Graham. *Introduction to Magnetic Materials.* IEEE Press - Wiley, 2nd edition, 2009.

[39] P. Langevin. *Ann. Chemie et Physique*, **5**: 70, (1905).

[40] G. Grosso and G. Pastori Parravicini. *Solid State physics.* Academic Press, first edition, 2000.

[41] P. Weiss. *Compt. Rend.*, **143**: 1136, (1906).

[42] S. Mader and A. S. Nowick. *Appl. Phys. Lett.*, **7**: 57, (1965).

[43] H. Lüth. *Solid Surfaces, Interfaces and Thin Films.* Springer, fourth edition, 2001.

[44] J. Stöhr and H. C.Siegmann. *Magnetism From Fundamentals to Nanoscale Dynamics.* Springer, 2006.

[45] L. Néel. *Ann. de Physique*, **18**: 5, (1932).

[46] H. A. Kramers. *Physica*, **1**: 182, (1934).

[47] P. W. Anderson. *Phys. Rev.*, **79**: 350, (1950).

[48] T. Wolfram, R. E. Dewames, W. F. Hall, and P. W. Palmberg. *Surf. Sci.*, **28**: 45, (1971).

[49] E. Kisker, K. Schröder, W. Gudat, and M. Campagna. *Phys. Rev. B*, **31**: 329, (1985).

[50] Y. Li and K. Baberschke. *Phys. Rev. Lett.*, **68**: 1208, (1992).

[51] D. Alders, L. H. Tjeng, F. C. Voogt, T. Hibma, G. A. Sawatzky, C. T. Chen, J. Vogel, M. Sacchi, and S. Iacobucci. *Phys. Rev. B*, **57**: 11623, (1998).

[52] S. Altieri, M. Finazzi, H. H. Hsieh, M. W. Haverkort, H. J. Lin, C. T. Chen, S. Frabboni, G. C. Gazzadi, A. Rota, S. Valeri, and L. H. Tjeng. *Phys. Rev. B*, **79**: 174431, (2009).

[53] N. D. Mermin and H. Wagner. *Phys. Rev. Lett.*, **17**: 1133, (1966).

[54] J. Li, M. Przybylski, F. Yildiz, X. L. Fu, and Y. Z. Wu. *Phys. Rev. B*, **83**: 094436, (2011).

[55] W. H. Meiklejohn and C. P. Bean. *Phys. Rev.*, **102**: 1413, (1956).

[56] Review: J. Nogués and I. K. Schuller. *J. Mag. Mag. Mat.*, **192**: 203, (1999).

[57] Review: J. Nogués, T. J. Moran, D. Lederman, I. K. Schuller, and K. V. Rao. *Phys. Rev. B*, **59**: 6984, (1999).

[58] A. Einstein. *Annalen der Physik*, **17**: 6, (1905).

[59] C.S. Fadley. *Basic concepts of X-ray photoelectron spectroscopy in: Electron spectroscopy: theory, techniques, and applications. Eds. C.R. Brundle and A.D. Baker.* Pergamon Press, 1978.

[60] R.L. Martin and D.A. Shirley. *Many-electron Theory of Photoemission in Electron spectroscopy: theory, techniques and applications.* Academic Press, 1984.

[61] B.H. Bransden and C.J. Joachain. *Physics of atoms and molecules.* Prentice Hall, second edition.

[62] N.W. Ashcroft and N.D. Mermin. *Solid State Physics*. BROOKS/COLE CENGAGE Learning.

[63] S. Hufner. *Photoelectron spectroscopy: principles and applications*. Springer, second edition, 1996.

[64] P. Auger. *J. Phys. Rad.*, **6**: 205, (1925).

[65] G. Wentzel. *Z Phys.*, **43**: 524, (1927).

[66] G. Di Filippo. *Dynamics of two-electron photoemission: a study of electronic correlations in solids*. PhD thesis, Universitá degli Studi Rome Tre, 2014.

[67] J. C. Slater. *Phys. Rev.*, **34**: 1293, (1929).

[68] C. J. Powell. *Phys. Rev. Lett.*, **30**: 1179, (1973).

[69] R. Y. Koyama and N. V. Smith. *Phys. Rev. B*, **2**: 3049, (1970).

[70] S. Hüfner and G. K. Wertheim and N. V. Smith and M. M. Traum. *Solid State Commun.*, **11**: 323, (1972).

[71] J. J. Lander. *Phys. Rev.*, **91**: 1382, (1953).

[72] M. Cini. *Solid State Commun.*, **20**: 605, (1976).

[73] R.A. Bartynski, E. Jensen, S.L. Hulbert, and C.C. Kao. *Progr. Surf. Sci.*, **53**: 155–162, (1996).

[74] O. Gunnarsson and K. Schönhammer. *Phys. Rev. B*, **22**: 3710, (1980).

[75] M. Ohno and G. Wendin. *J. Phys. B: At. Mol. Phys.*, **12**: 1305, (1979).

[76] K. Schönhammer and O. Gunnarsson. *Surf. Sci.*, **89**: 575, (1979).

[77] G. Stefani, R. Gotter, A. Ruocco, F. Offi, F. Da Pieve, A. Verdini, A. Liscio, S. Iacobucci, H. Yao, and R. Bartynski. Relevance of the core hole alignment to auger-photoelectron pair angular distributions in solids. In J. Berakdar and J. Kirschner, editors, *Correlation Spectroscopy of surfaces,Thin Films and Nanostructures*. Wiley, 2004.

[78] U. Fano and G. Racah. *Irreducible Tensorial Sets*. Academic Press - New York, 1959.

[79] N. M. Kabachnik. *J. Phys. B: At. Mol. Opt. Phys.*, **25**: L389, (1992).

[80] V. V. Balashov and A. N. Grum-Grzhimailo and N. M. Kabachnik. *Polarization and Correlation Phenomena in Atomic collisions*. Kluwer Academic/Plenum Press - New York, 2000.

[81] Y. U. Idzerda. *Surf. Rev. Lett.*, **4**: 161, (1997).

[82] F. Da Pieve, D. Sébilleau, S. Di Matteo, R. Gunnella, R. Gotter, A. Ruocco, G. Stefani, and C. R. Natoli. *Phys. Rev. B*, **78**: 035122, (2008).

[83] D. E. Ramaker, H. Yang, and I. U. Idzerda. *J. Elec. Spectr. Rel. Phen.*, **68**: 63, (1994).

[84] E. E. Koch, D. E. Eastman, and Y. Farges. *Handbook of Synchrotron Radiation*, volume 1a. North-Holland Publishing Company, Amsterdam, 1983.

[85] S.Mobilio. Interaction between radiation and matter: an introduction. In S. Mobilio and G. Vlaic, editors, *Synchrotron Radiation: Fundamentals, Methodologies and Applications*, volume 82. Societá Italiana di Fisica, 2001.

[86] D. H. Tomboulian and P. L. Hartman. *Phys. Rev.*, **102**: 1423, (1956).

[87] www.aps.anl.gov.

[88] G. Margaritondo, Y. Hwu, and G. Tromba. Synchrotron light: from basics to coherence and coherence-related applications. In S. Mobilio and G. Vlaic, editors, *Synchrotron Radiation: Fundamentals, Methodologies and Applications*, volume 82. Societá Italiana di Fisica, 2001.

[89] https://www.elettra.trieste.it/lightsources/elettra/odac/elettra-parameters.html?showall=.

[90] https://www.elettra.trieste.it/it/lightsources/elettra/elettra-beamlines/aloisa/aloisa-instrumentation.html.

[91] R. Gotter, A. Ruocco, A. Morgante, D. Cvetko, L. Floreano, F. Tommasini, and G. Stefani. *Nucl. Instr. Meth. A*, **467-468**: 1468, (2001).

[92] G. H. Moore, C. C. Davis, M. A. Coplan, and S. C Greer. *Building Scientific Apparatus*. Cambridge University Press, Fourth edition, 2009.

[93] www.sjuts.com.

[94] J. L. Wiza. *Nucl. Instr. Meth.*, **162**: 587, (1979).

[95] P. Schagen. *Advances in image pick-up and display*, volume 1. Academic Press, New York, 1974.

[96] J. Vallerga and J. McPhate. *Proceedings of SPIE*, **4139**: 34, (2000).

[97] O. Siegmund and J. Vallerga and P. Jelinsky and X. Michalet and S. Weiss. *IEEE Nucl. Sci. Symp. Conf. Rec.*, **N14-55**: 448, (2005).

[98] H.W. Haak. PhD thesis, University of Groningen, 1983.

[99] E. Jensen, R. A. Bartynski, S. L. Hulbert, and E. D. Johnson. *Rev. Sci. Instr.*, **63**: 3013, (1992).

[100] M. Völkel and W. Sandner. *J. Phys. E: Sci. Instrum.*, **16**: 456, (1982).

[101] R. Gotter, F. Offi, F. Da Pieve, A. Ruocco, G. Stefani, S. Ugenti, M.I. Trioni, and R.A. Bartynsky. *J. Elect. Spec. Rel. Phen.*, **161**: 128, (2007).

[102] G. Ghiringhelli, L. H. Tjeng, A. Tanaka, O. Tjernberg, T. Mizokawa, J. L. de Boer, and N. B. Brookes. *Phys. Rev. B*, **66**: 075101, (2002).

[103] I. D. Hughes, M. Däne, A. Ernst, W. Hergert, M. Lüders, J. B. Staunton, Z. Szotek, and W. M. Temmerman. *New J. Phys.*, **10**: 063010, (2008).

[104] R. Gotter, G. Fratesi, R. A. Bartynski, F. Da Pieve, F. Offi, A. Ruocco, S. Ugenti, M. I. Trioni, G. P. Brivio, and G. Stefani. *Phys. Rev. Lett.*, **109**: 126401, (2012).

[105] R. Gotter, M. Sbroscia, M. Caminale, S. R. Vaidya, E. Perfetto, R. Moroni, F. Bisio, S. Iacobucci, G. Di Filippo, F. Offi, A. Ruocco, G. Stefani, L. Mattera, and M. Cini. *Phys. Rev. B*, **88**: 094403, (2013).

[106] W. Neubeck, C. Vettier, V. Fernandez, F. de Bergevin, and C. Giles. *J. Appl. Phys.*, **85**: 4847, (1999).

[107] M. Caffio, B. Cortigiani, G. Rovida, A. Atrei, and C. Giovanardi. *J. Phys. Chem. B*, **108**: 9919, (2004).

[108] M. Caffio, A. Atrei, B. Cortigiani, and G. Rovida. *J. Phys.: Condens. Matter*, **18**: 2379, (2006).

[109] J. Wollschlager, D. Erdos, H. Goldbach, R. Hopken, and K.M. Schroder. *Thin solid films*, **400**: 1–8, (2001).

[110] S. Tanuma, C. J. Powell, and D. R. Penn. *Surf. Interface Anal.*, **21**: 165, (1994).

[111] J. J. Yeh and I. Lindau. *Atom. Data Nucl. Data*, **32**: 1, (1985).

[112] D. Spanke, V. Solinus, D. Knabben, F. U. Hillebrecht, F. Ciccacci, L. Gregoratti, and volume = "**58**" pages = " 5201" year = "(1998)" M. Marsi", journal = "Phys. Rev. B".

[113] S. Altieri, M. Finazzi, H. H. Hsieh, H. J. Lin, C. T. Chen, T. Hibma, S. Valeri, and G. A. Sawatzky. *Phys. Rev. Lett.*, **91**: 137201, (2003).

[114] M. W. Haverkort, S. I.Csiszar, Z. Hu, S. Altieri, A. Tanaka, H. H. Hsieh, H. J. Lin, C. T. Chen, T. Hibma, and L. H. Tjeng. *Phys. Rev. B*, **69**: 020408, (2004).

[115] E. Arenholz, G. van der Laan, R. V. Chopdekar, and Y. Suzuki. *Phys. Rev. Lett.*, **98**: 197201, (2007).

[116] J. S. Kang, S. S. Lee, H. J. Lee, G. Kim, H. K. Song, Y. J. Shin, M. C. Jung, H. J. Shin, J. E. Lee, and B. I. Min. *IEEE T. Magn.*, **45**: 2580, (2009).

[117] G. van der Laan, N. D. Telling, A. Potenza, S. S. Dhesi, and E. Arenholz. *Phys. Rev. B*, **83**: 064409, (2011).

[118] S. R. Krishnakumar, M. Liberati, C. Grazioli, M. Veronese, S. Turchini, P. Luches, S. Valeri, and C. Carbone. *J. Mag. Mag. Mat.*, **310**: 8, (2007).

[119] D. Lederman, J. Nogués, and I. K. Schuller. *Phys. Rev. B*, **56**: 2332, (1997).

[120] M. Cini, E. Perfetto, R. Gotter, F. Offi, A. Ruocco, and G. Stefani. *Phys. Rev. Lett.*, **107**: 217602, (2011).

[121] A. Fujimori and F. Minami. *Phys. Rev. B*, **30**: 957, (1984).

[122] J. Zaanen, G. A. Sawatzky, and J. W. Allen. *Phys. Rev. Lett.*, **55**: 418, (1985).

[123] F. Da Pieve and S. Fritzsche and G. Stefani and N. M. Kabachnik. *J. Phys. B: At. Mol. Opt. Phys.*, **40**: 329, (2007).

[124] L. Braicovich, G. Ghiringhelli, A. Tagliaferri, G. van der Laan, E. Annese, and N. B. Brookes. *Phys. Rev. Lett.*, **95**: 267402, (2005).

[125] J. Shen, J. Giergiel, and J. Kirschner. *Phys. Rev. B*, **52**: 8454, (1995).

[126] W. Platow, U. Bovensiepen, P. Poulopoulos, M. Farle, K. Baberschke, L. Hammer, S. Walter, S. Müller, and K. Heinz. *Phys. Rev. B*, **59**: 12641, (1999).

[127] J. Y. Rhee. *J. Korean Phys. Soc.*, **46**: S30, (2005).

[128] S. H. Kim, K. S. Lee, H. G. Min, J. Seo, S. C. Hong, T. H. Rho, and J.-S. Kim. *Phys. Rev. B*, **55**: 7904, (1997).

[129] T. C. Q. Noakes, P. Bailey, and G. van der Laan. *Phys. Rev. B*, **67**: 153401, (2003).

[130] M. Canepa, S. Terreni, P. Cantini, A. Campora, and L. Mattera. *Phys. Rev. B*, **56**: 4233, (1997).

[131] W. F. Egelhoff Jr. and I. Jacob. *Phys. Rev. Lett.*, **62**: 921, (1989).

[132] F. Huang, M. T. Kief, G. J. Mankey, and R. F. Willis. *Phys. Rev. B*, **49**: 3962, (1994).

[133] B. Schulz and K. Baberschke. *Phys. Rev. B*, **50**: 13467, (1994).

[134] X. Y. Lang, W. T. Zheng, and Q. Jiang. *Phys. Rev. B*, **73**: 224444, (2006).

[135] D. M. Schaller, D. E. Bürgler, C. M. Schmidt, F. Meisinger, and H. J. Güntherodt. *Phys. Rev. B*, **59**: 14516, (1999).

[136] F. Bisio, S. Terreni, M. Canepa, and L. Mattera. *Phys. Rev. B*, **72**: 174413, (2005).

[137] G. A. Sawatzky. Auger Photoelectron Coincidence Spectroscopy. In C. L. Briant and R. P. Messmer, editors, *Auger electron spectroscopy*. Academic Press, Boston, 1988.

[138] Review: J. Nogués and J. Sort and V. Canglais and V. Skumryev and S. Suriñach and J. S. Muñoz and M. D. Baró. *Phys. Rep.*, **422**: 65, (2005).

[139] Information storage insight. *Nat. Mater.*, **6**: 807, (2007).

[140] M. Finazzi, L. Duó, and F. Ciccacci. *Surf. Sci. Reports*, **64**: 139, (2009).

[141] P. Luches, L. Pasquini, S. Benedetti, V. Bellini, S. Valeri, F. Manghi, R. Rüffer, and F. Boscherini. *Phys. Rev. B*, **83**: 094413, (2011).

[142] P. Luches, L. Pasquini, S. Benedetti, S. Valeri, R. Rüffer, and F. Boscherini. *Appl. Phys. Lett.*, **101**: 082412, (2012).

[143] P. Luches, S. Benedetti, A. di Bona, and S. Valeri. *Phys. Rev. B*, **81**: 054431, (2010).

[144] S. Colonna, A. Cricenti, P. Luches, S. Valeri, F. Boscherini, J. Qi, Y. Xu, and N. Tolk. *Superlattice Microst.*, **46**: 107, (2009).

[145] W. Kim, E. Jin, J. Wu, J. Park, E. Arenholz, A. Scholl, C. Hwang, and Z. Q. Qiu. *Phys. Rev. B*, **81**: 174416, (2010).

[146] R. Abrudan, J. Miguel, M. Bernien, C. Tieg, M. Piantek J. Kirschner, and W. Kuch. *Phys. Rev. B*, **77**: 014411, (2008).